Measuring Wave Forces Along Alaska's Coastal Sea Ice

Principal Investigators: Mark A. Johnson[1] and Andrew R. Mahoney[2]

[1]College of Fisheries and Ocean Sciences, University of Alaska Fairbanks
[2]Geophysical Institute, University of Alaska Fairbanks

March 2021
Final Report
OCS Study BOEM 2021-019

BOEM
Bureau of Ocean Energy Management

UAF UNIVERSITY OF ALASKA FAIRBANKS

TABLE OF CONTENTS

List of Tables

List of Figures

ABSTRACT

We designed, built, tested, and deployed portable sensors that measured motion on Chukchi Sea landfast ice and Beaufort Sea drifting sea ice. Our purpose was to acquire information about sea ice motion, forced by winds, waves, or ice-ice interaction, and determine how such motion is related to the formation, decay, and detachment of landfast ice. A key goal is identifying sea ice motion that could be used predictively as part of an early-warning system for landfast ice breakout events, a significant human hazard along the northern coast of Alaska. To meet our objectives, we developed three prototype sensor systems, two using the Vectornav VN-100 Inertial Measurement Unit and one using the Seaview Systems, Inc., SVS-603 wave sensor. Laboratory and field tests led to the production of a sensor (Ice Wave Rider) that acquired more than 9,000 hours of data at 10 Hz, mostly from locations on stable ice in Elson Lagoon, Alaska, from quasi-stationary landfast ice north and west of Utqiaġvik, Alaska, and from drifting ice in the Beaufort Sea accessed through the U.S. Navy ICEX2018 and ICEX2020 campaigns. The acquired data consists of vertical and horizontal acceleration and the attitude heading references yaw, pitch, and roll. The measurements can be characterized broadly as "jolts" where ice-ice collisions produced large, short-lived spikes in horizontal and vertical accelerations, "rumbles" where ice-ice interaction associated with ridge formation or ice-ice grinding lasted for minutes or longer, and wind-forced periodic motion identified as waves in ice. Wave signals in the 2020 Ice Wave Rider data showed frequencies consistent with the dispersion relationship expected for waves under an ice cover treated (mathematically) as an elastic plate. For specific wind speeds and ice thicknesses, resonance conditions may occur where the wave energy cannot propagate away, causing the local wave amplitude to grow. Detecting the conditions that permit resonance may be important to forecasting breakout events, understanding the evolving shape of the ice edge, and predicting the timing of seasonal ice breakup.

Relevance and Utility

The results of this project improve our understanding of the seasonal cycle of sea ice in the nearshore region of northern Alaska and support analysis and investigation of breakout events in which shorefast ice detaches and drifts away from the coast. This project is relevant to maritime safety impacted by detached and drifting ice and to breakout events that can pose significant risks to personnel and assets on the ice. The project also provided insights into convergence events where drifting ice impacts the shorefast ice. Such movements can cause the ice to deform and pile-up, creating hazards both on the ice and near the shoreline. This work helps the subsistence community, who rely on the landfast ice for transport and hunting, and improves the potential for determining the navigational window, particularly during the shoulder seasons of freeze-up and breakup.

This project contributes to developing the methodology for predicting the stability and safety of coastal shorefast ice in three specific ways. First, we have demonstrated our ability to design, build, and deploy rugged, highly portable sensors that incorporate MEMS (micro-electro-mechanical systems) technology and can be powered for at least two months in the extreme regions of northern Alaska. These sensors telemeter limited amounts of data at a nominal cost. Our laboratory tests showed that we could increase data transfer at a relatively low cost by building a telemetry system using commercially-available, low-energy XBee radios to relay large amounts of data from the offshore limits of the landfast ice to shore stations and into the internet. Second, this project measured, simultaneously by separated instruments, harmonic signals consistent with wave propagation under an ice cover. The measured signals obey the dispersion relationship for wave propagation in ice. The measurements show that the conditions

encountered along the coast of Alaska can create resonance conditions where the local wave amplitude grows, a potential mechanism to initiate breakout. Third, this project supported the development of sensors and analysis tools that helped lay the foundation for new work funded through the U.S. Army and the Cold Regions Research and Engineering Laboratory. That work continues the development of the sensors described in this report, continues their deployment at multiple locations along coastal Alaska, and permits the ongoing evolution of our analysis techniques. The project, "ISOPS - Integrated System for Operations in Polar Seas," formally began in February 2021. The work accomplished here is one of multiple steps needed for developing a sea ice forecast system for coastal Alaska relevant to an ice-ocean system responding to climate change.

INTRODUCTION

The potential for offshore exploration and development of hydrocarbon resources in Alaska's Chukchi and Beaufort Seas opens opportunities for considerable marine activity, mainly during the open water season. In a December 16, 2011 lease approval letter to Shell, BOEM imposed certain restrictions on marine operations on the Alaska OCS due to concerns associated with possible oil spills "in consideration of the distance to limited support infrastructure on the Chukchi coast" and because of the "Secretary of Interior's desire to proceed cautiously with oil and gas development in the Chukchi Sea."

The duration of open water operations may increase due to the lengthening melt season inferred from satellite-derived surface ice temperature trends (Comiso, 2002), declining ice extent (Bjørgo *et al.*, 1997; Parkinson *et al.*, 1999), and thinning ice (Rothrock *et al.*, 1999; Wadhams and Davis, 2000). These trends suggest that increased exposure of the Arctic Ocean to surface winds and increased fetch will provide more area for wind-generated waves to propagate into slush and brash ice, create floes of different sizes and strengths, and affect the landfast ice at the Arctic periphery.

Our primary motivation was to provide information relevant to human safety as our stakeholders include indigenous users and marine operators. An overarching goal was developing and deploying a sensor platform to provide early warning about breakouts and other important ice events by flagging critical data in real-time and then alerting forecasters and ice users about specific conditions measured on the ice. To that end, a prototype sensor was designed, built, and cold-tested initially in Fairbanks. The first field deployments were on stable ice in Elson Lagoon near Point Barrow, Alaska. After initial tests proved successful, additional sensors were built for deployment on the Chukchi Sea landfast ice near Utqiaġvik, Alaska. As the sensor design was improved by making it smaller, less cumbersome, and more powerful, we added additional telemetry to acquire on-ice data in real-time. Real- or near-real-time data acquisition is necessary to establish a functional early warning system for ice users and other stakeholders, including the oil and gas industry. The successful design and deployment of the sensors developed here improves our understanding of how ice responds to stresses from wind waves, coastal waves, storm surges, and possibly ship wakes. This work is a step toward providing a predictive capability for the stresses that drive landfast ice breakout events.

Some of the more extreme risks along the Chukchi Sea coast occur where landfast ice detaches from the coast or adjacent immobile ice partway through the landfast ice season. Such mid-season events are called breakouts, in contrast with the final detachment at the end of the season, referred to as breakup. Breakout events represent a significant hazard for anyone occupying landfast ice at the time and are considered by indigenous hunters as one of the primary ice-associated risks. Indigenous Elders and hunters report that mid-season breakouts have become more common and more difficult to predict in recent decades (Gearheard *et al.*, 2006; Jones *et al.*, 2016) and are now a serious safety concern that impacts the success of spring bowhead whaling (Norton and Gaylord, 2004; Druckenmiller *et al.*, 2012). The rarity of mid-winter breakout events before the 1990s (Jones *et al.*, 2012) suggests that the landfast ice is responding to ongoing climate change and the reductions in sea ice evident throughout the Arctic.

During the spring bowhead whale hunt, 200 or more people may use trails built on the landfast ice near Utqiaġvik, Alaska (Druckenmiller *et al.*, 2009). Multiple whaling teams in the communities of Wales, Point Hope, Point Lay, and Wainwright also use landfast ice at this time, while seal hunters are likely out in other coastal communities. Breakouts put lives at risk and can require substantial resources to mitigate.

1

For example, helicopters were needed to rescue more than 50 whalers after a breakout occurred during the 2002 hunting season (George *et al*., 2004b), and a breakout event in 2014 required boats to rescue two whaling crews when winds were too strong for a helicopter (Mahoney *et al*., 2017).

There appears to be no "simple set of indicators" (George *et al*., 2004a) to evaluate breakout risk, but most breakout events involve some combination of destabilization followed by an offshore component of forcing from winds or currents (Mahoney *et al*., 2007; Jones *et al*., 2016). Changes in sea level and influxes of warm water likely weaken the anchoring strength of grounded ridges that hold the landfast ice in place (George et al., 2004b; Mahoney et al., 2007; Jones et al., 2016). Rapid, small fluctuations in seafloor pressure and "flickering" in time-lapse coastal radar imagery indicate that waves may also play a role (Bates and Shapiro, 1980; Shapiro and Metzner, 1987; Mahoney *et al*., 2007). Mahoney *et al*. (2007) showed that fluctuations in radar backscatter from apparently stationary targets might be used to develop an early warning system from radar installations on shore. A reasonable expectation is that wave propagation destabilizes the landfast ice either by fracturing the ice cover or reducing the shear strength of grounded ridge keels, allowing any subsequent offshore winds to displace the ice from the coast.

Identifying potential precursors to landfast ice breakout is motivated by Shapiro (1987), who first observed the "flickering" in sequences of radar imagery several hours before observing measurable ice motion associated with a number of breakout events between 1974 and 1977. Speculation that the radar flickering could have indicated wave propagation into the ice was supported by tide gauge data showing "vertical waves" of several centimeters amplitude under landfast ice prior to a large (10 meter) ice-push event (Bates and Shapiro, 1980). The observed period of these waves was around 600 seconds, much longer than those typically associated with wind waves and swell. Bates and Shapiro argued that, as pressure ridges form, impulses from ice motion transfer stored elastic energy into the ocean, exciting the longer period gravity waves. Marchenko *et al*. (2002) showed such waves could propagate to the coast and transfer energy to edge waves that then propagate along the coast. Their analytical model showed wavelengths between 11 and 16 kilometers. Although the ice's resulting curvature would not be sufficient to crack the ice (Squire *et al*., 1995), we speculate that repeated cyclic loading could destabilize landfast ice by weakening it at critical attachment points or causing rearrangement of blocks in grounded ice keels.

Local traditional knowledge describes breakouts arising due to pack ice abrasion, ice deterioration from offshore directed under-ice currents, rapid changes to sea level, and chiseling of mobile ice against landfast ice (Druckenmiller *et al.*, 2009). Two breakout events at Utqiaġvik in 2007 (Druckenmiller *et al*., 2009) were associated with currents advecting pack ice along the landfast ice edge and driving ice-ice collisions that destabilized the landfast ice seaward of a line of grounded ridges. Local winds drove onshore Ekman transport that raised the sea level along the Chukchi coast, possibly preconditioning the ice by destabilizing attached ice keels. When the winds veered to the southeast, the ice was driven offshore. In a 1997 event described in George *et al*. (2004b), a "jolt" was felt in the landfast ice before breakout. Recent changes affecting the landfast ice, such as later freeze-up and earlier breakup (Johnson and Eicken, 2016), can conflict with the traditional/indigenous understanding of sea ice patterns built from an oral history extending back more than a thousand years (Gearheard *et al*., 2006).

Because landfast ice is often heavily ridged, detached ice may become a hazard to navigation. Wave propagation into ice can lead to floe fragmentation and destabilization and is thus important to the strength of the ice and the evolution/shape of the ice edge. Accurately locating the ice-edge boundary and

understanding how it may change under different wave regimes are critical shortcomings in many forecast models.

The National Weather Service (NWS) is the forecasting agency for weather-scale (10 – 12 day) events for the coastal Chukchi and Beaufort Seas. The NWS's "tactical scale" forecasts are necessary to schedule safe marine operations, including shipping to remote coastal communities. The current generation of ice-ocean models does not reliably provide navigators and ice-users with details of ice-formation, nor does it provide estimates of the decay of sizable ice. Reliable forecasts require better knowledge of the ocean's heat content, stratification, and air-sea heat fluxes and require better knowledge of the processes that affect the mechanical erosion of ice from storm-induced waves.

Surface wave heights in the Arctic are increasing (Francis and Vavrus, 2012), and bigger waves may lead to more ice break, more open water, and even bigger waves via a positive feedback loop. In September 2012, when the Beaufort Sea was largely free of ice, the significant open water allowed wind waves to evolve into sea swell, with the long waves propagating away from the generating winds. Waves of 5 m were forced by winds up to 18 m s^{-1} (Thomson and Rogers, 2014). With reduced Arctic ice cover and larger waves, swells may become more common. Swells carry more energy and have longer attenuation scales (Squire *et al*., 1995; Squire, 2007) and can further increase ice break and enhance ice retreat (Thomson and Rogers, 2014), potentially becoming another driver towards reduced or ice-free Arctic summers.

In the open ocean, a typical wave spectrum has an amplitude peak in the period range of 2 to 30 seconds, the range for wind-driven waves and sea swell propagating as gravity waves (Hunkins, 1962). Large-scale atmospheric storms can excite waves exceeding 25 seconds, generally outside of wave periods under a sea-ice cover (Hanafin *et al*., 2012; Ardhuin *et al*., 2016). The WAVEWATCH II model, for example, includes wave frequencies from 0.0338 to 0.7 Hz or periods from 1.4 to 29.6 seconds (Ardhuin et al., 2016). Infragravity waves can range to tens of seconds (e.g., 30–50 second range as found by Mahoney *et al*., 2016).

When surface waves reach the sea-ice boundary, their energy is attenuated due to scattering and dissipation (Ardhuin *et al*., 2016). Scattering and dissipation have different effects on wave energy, so analysis of swell directional spreading and arrival times can help determine the relative importance of scattering versus dissipation. Measurements in pack ice show scattering has a negligible role in attenuating long swells but reduces the passage of shorter waves.

Robin (1963) conducted one of the first systematic comparisons of wave amplitude and wave period in the Weddell Sea and found ocean swells with periods between 4 and 24 seconds. Longer swells, from 11 to 23 seconds, propagate through large floes by bending them. Ice flex can generate turbulence, weaken ice, and cause ice fracture. Smaller floes, those less than ~40 meters in diameter and 1.5 meters thick, respond as rigid bodies. The ice acts as a low-pass filter by removing shorter periods and attenuating longer swells less. When the floe length is less than 1/6 the wave wavelength, most of the wave energy passes through. Ice floes block wave penetration when they are larger than half the wave wavelength. The most intense energy near the ice edge flexes the ice and breaks it into fragments resulting in a floe size distribution where the smallest pieces are nearest to open water. Wave energy decreases in intensity and the peak period increases as waves encounter and propagate into the marginal ice zone. For continuous

sea-ice, waves and swell can cause cracks that may open into leads when winds or currents diverge the ice (Langhorne et al., 2001).

Measuring waves in sea ice was an important part of scientific experiments in the 1970s and 1980s when camps were set up on drifting sea ice and wire strainmeters were the commonly used tools (Squire, 1978; Squire and Allan, 1980; unpublished data cited in Doble *et al*., 2006). Tilt meters were a reasonable alternative when deployed in direct contact with ice, although leveling the instrument was sometimes problematic. (See projects such as Arctic Internal Waves Experiment, AIWEX, and the Coordinated Eastern Arctic Experiment, CEAREX, for details.) A pilot experiment north of Svalbard from Alfred Wegener Institute's research vessel *Polarstern* demonstrated that tilt meters could be used successfully instead of wire strainmeters. Doble (2004) described a tilt meter (from Applied Geomechanics, Inc.) with a customized self-leveling mechanism controlled by microprocessors and stepping motors. As the technology developed, high-sensitivity accelerometers were used, overcoming past fragility, maintenance costs, and transport challenges.

Kohout *et al*. (2015) used ship- and helicopter-deployed accelerometers to measure storm-generated wave signals propagating into the ice hundreds of kilometers from the Antarctic ice edge. They found decay was near linear for waves larger than three meters, which conflicts with the assumption of exponential energy decay (Dumont *et al*., 2011) and suggests the need for additional direct measurements. Kohout *et al.*'s Antarctic results strengthen expectations that similar processes occur in Arctic ice. For example, remotely forced shelf waves, such as those documented by Danielson *et al*. (2014) in the Chukchi Sea, can modulate sea-surface height (up to 10 centimeters modeled heights) along the coast and impose stress on ice anchored to the bottom. According to Danielson *et al*., the wave period depends on whether wave generation is remote or local. Regardless of the forcing, shorter wavelengths are preferentially filtered out by the sea ice, indicating that the wavelength and ice floe-size distribution are related (Williams *et al*., 2013). This relationship is important for defining ice rheology.

Considerable work has been done to define a boundary between fragmented sea ice and the central ice pack (see Dumont *et al.,* 2011). Williams *et al*. (2013) set a theoretical foundation for wave-ice interaction that addresses wave attenuation and breaking of floes in the marginal ice zone, defining key parameters based on ice damping of wave energy and the wave-induced breakup of ice. Their model accounts well for the loss of wave energy into the ice away from the ice edge. However, our focus is on landfast ice, often with an abrupt boundary exposed to open water at the lead edge.

Greenhill (1886) first developed an elastic plate model where sea ice behaves as a thin, unbroken ice sheet. That model did not predict attenuation and was modified to model energy loss (Wadhams, 1973; Squire and Allan, 1980; Liu and Mollo-Christensen, 1988; Squire and Fox, 1992; Balmforth and Craster, 1999). Wang and Shen (2010) treated the ice as a homogeneous incompressible viscoelastic fluid and applied a finite thickness viscoelastic model by assuming floes are small compared to the wave wavelength. The resulting dispersion relation becomes an approach for approximating ice thickness. Wadhams and Doble (2009) used their thin elastic plate model to track mean Arctic sea ice thickness using the dispersion relation for infragravity waves. A thin elastic plate model developed for a continuous ice sheet may be the most applicable for landfast ice, depending on the ice rigidity and viscosity.

When ice is compacted due to on-ice winds or compacted near the coast by onshore winds, ice floes converge and may act collectively as a single unit. Under compaction, the floes cannot surge, and wave

attenuation may be due primarily to viscous losses from the under-ice boundary layer (Squire *et al.*, 1995). For very thick floes, some of the wave energy may be lost as reflections at the ice edge and at pressure ridges further into the ice (Squire *et al.*, 1995). If the wave energy that propagates into the ice results in ice stresses larger than the ice strength, fracturing occurs, allowing ice to be removed by winds or currents as suggested for the Chukchi Sea breakouts. Squire *et al.* (1995) noted that the ice breakdown process is a common occurrence, particularly at the ice edge where the steepest waves are found. This is important around the Arctic periphery, and Utqiaġvik in particular, where extensive regions of landfast ice have seaward edges exposed to waves that cause the ice to flex, stress, and break apart.

Different ice regimes require specific models to derive information about the local ice properties. A single, comprehensive model describing wave propagation into all ice types does not yet exist (Wang and Shen, 2010). There are two broad model classes that can account for the length and height changes of waves propagating into sea-ice (Squire, 2007), and they range from continuous ice to ice treated as individual floes.

For ocean waves, frequency and wave number are related by a dispersion relationship. The dispersion relationship without an ice cover is $\omega = \sqrt{gk \tanh(kH)}$, where g is gravity, H is water depth, and the wavenumber k is $2\pi/\lambda$ for wavelength λ. A simplified "deep-water" or "short-wave" approximation using $\omega = \sqrt{gk}$ can be used when $kH > \sim3$ because the *tanh* function asymptotes to 1. For example, in the deep water of the Arctic Ocean where H=1000 meters or more, wavelengths up to ~1700 meters and periods up to ~33 seconds can be approximated by the deep-water dispersion relation. These waves appear as long swell gravity waves.

For the comparatively shallow water off Utqiaġvik, where some of our sensors were deployed, the depth is 55 meters. Here, the deep-water approximation holds reasonably well for wavelengths less than ~172 meters and periods up to ~10 seconds. These are still "short waves" compared to the depth. For the discussions here, we will use the full dispersion relation, or the deep-water approximation if valid, for an ocean without ice cover.

When the ice cover is treated as a thin elastic plate, the dispersion relation for waves in sea ice is (Liu and Mollo-Christensen, 1988; Squire et al., 1995; Sutherland and Rabault, 2016):

$$\omega^2 = \frac{gk + Dk^5 - Qk^3}{\coth(kH + kM)} \qquad \text{(Equation 1)}$$

where ω is the wave frequency $\frac{2\pi}{T}$ for period T, k is the wavenumber $\frac{2\pi}{\lambda}$ for wavelength λ, g is gravity, H is water depth, D is the bending modulus, Q arises from compression forces, and M represents the added mass from the ice plate. D depends on the ice thickness and its rheological properties such that

$D = \frac{Eh^3}{\rho_w 12(1-\nu^2)}$, where E is Young's modulus, h is ice thickness, ρ_w is water density, and ν is the Poisson ratio.

In general, the ice compression term $Q = {Ph}/{\rho_i}$ (where ρ_i = ice density) and the mass loading term $M = h{\rho_i}/{\rho_w}$ are much smaller than the gravity and bending terms and are neglected. Here, the following values are adopted (see Squire et al., 1995; Sutherland and Rabault, 2016): $E = 3 \times 10^9$ N m^{-2}, P=0, $\rho_w = 1025$ kg m^{-3}, $\rho_i = 922.5$ kg m^{-3}, and $\nu = 0.3$

Figure 1 compares the frequency and phase speeds from the dispersion relationships for cases with and without ice. It shows that the group velocity, the velocity at which the wave energy propagates, increases due to a 1-meter ice cover for frequencies greater than ~0.06 Hz, and the phase velocity increases for frequencies greater than ~0.075 Hz. When the frequency is greater than 0.145 Hz, the group velocity, C_g, becomes greater than the minimum in the phase velocity, C_p. As the water shallows, this transition point, where the group velocity exceeds the phase velocity, $C_g > C_p$, shifts to lower frequencies.
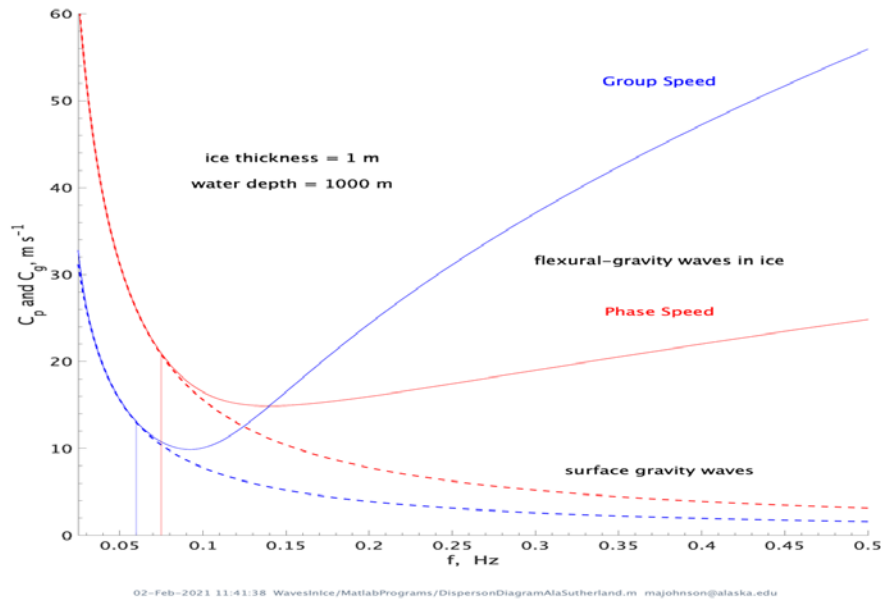
Figure 1. Phase (red) and group (blue) velocities for gravity waves (lower lines) and flexural-gravity waves (upper lines) for 1-meter thick ice cover. The group velocities diverge above frequencies of ~0.06 s^{-1}, and the phase velocities diverge above frequencies of ~0.075 s^{-1}.

Based on equation (1), an ice cover increases the wavelength and reduces the wavenumber for frequencies greater than $\sim 2\pi/15$ seconds for deep water (H=1000 m) and 1-meter thick ice (Figure 2). For example, for a frequency of $2\pi/5$ seconds, the wavenumber is 0.161 m^{-1} without an ice cover and reduces to k=0.079 m^{-1} with ice. The presence of ice has almost doubled the wavelength from ~40 m to ~80 m.
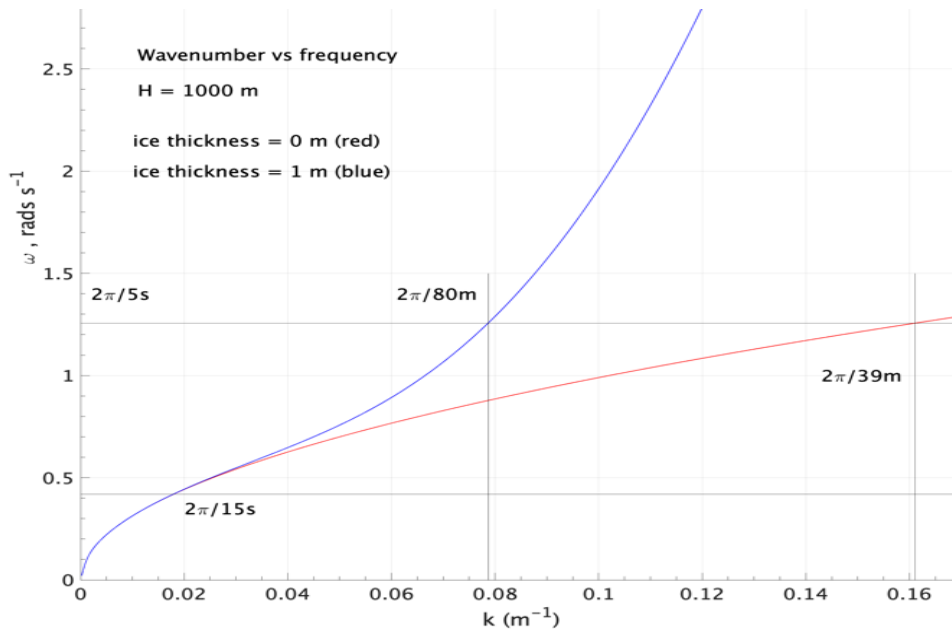
Figure 2. Wavenumber, k, versus frequency, ω, for 1-meter thick ice cover (blue line) and without ice (red line). For frequencies greater than $2\pi/\sim15$ seconds, the ice cover reduces the wavenumber, lengthening the wave.

What kind of forcing is required to excite waves in ice? The velocity of an atmospheric pressure field moving over the ice or of the winds from a moving storm are important factors to consider. A pressure field or winds traveling at some velocity will excite waves at that phase velocity. If the pressure field or wind velocity is less than the minimum wave phase velocity, no waves are forced. For the 1000-meter depth and 1-meter ice cover shown in Figure 1, this minimum speed is ~16 m s^{-1}.

Sea ice strongly affects the dispersion relation because of the k^5 dependence in the bending modulus term, allowing nonlinearities to arise (Sutherland and Rabault, 2016). This can occur even when the wave steepness, ak, where a is wave amplitude, is too small to drive nonlinearities in open water (Liu and Mollo-Christensen, 1988; Sutherland and Rabault, 2016).

The wavenumber is also influenced by the water depth (Figure 3). For a frequency of $2\pi/15$ seconds and a depth of 55 meters, the wavenumber is $k=0.0213$ m^{-1}, and the wavelength is 295 meters, shorter than the 354-meter wavelength for 1000-meter water depth. The wavenumber and wavelength are unchanged for frequencies greater than $\sim2\pi/5$ seconds.
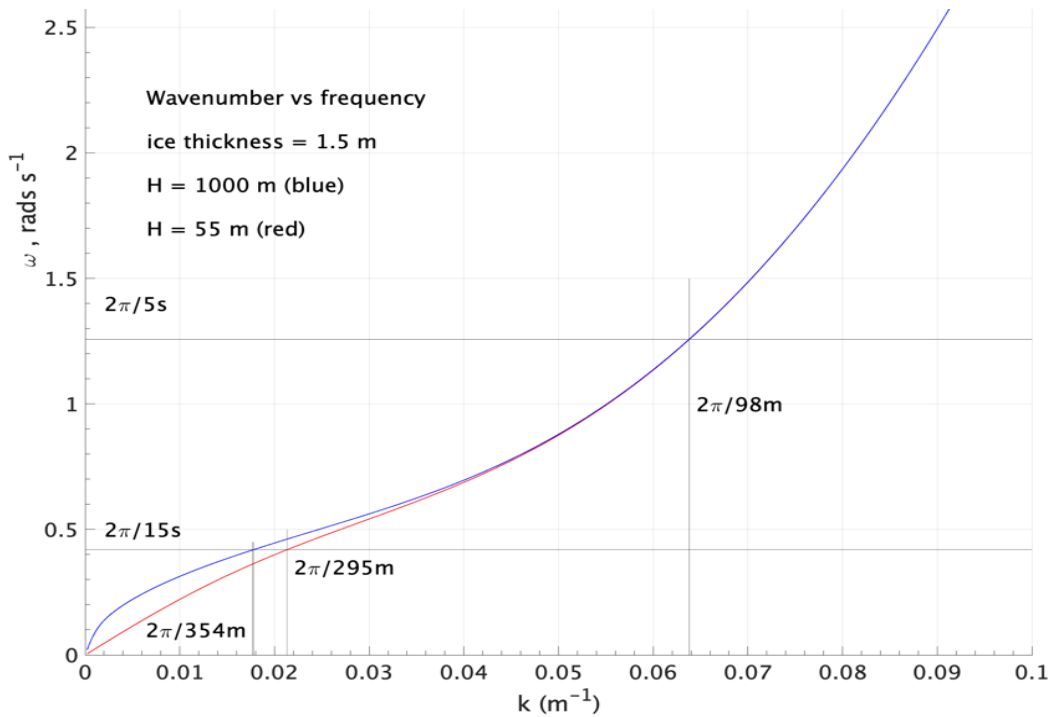
Figure 3. Wavenumber, k, versus frequency, ω, phase diagram for waves with 1.5 m of ice for water depths of 55 m (red) and 1000 m (blue). The water depth has an influence on wave numbers less than ~0.04 m^{-1}.

If the wind speed is greater than the phase velocity minimum and less than the long wave velocity, i.e., $\sqrt{gH}$, then two waves are excited, both with phase speeds equal to the moving pressure field or wind speed, but with slightly different wavelengths. Because the group velocity of the k^- wave is smaller than the k^+ wave (see Figure 1), energy is transferred away from the atmospheric pressure field at two different group velocities. If the pressure velocity is greater than $\sqrt{gH}$, there is only one wave transferring energy away.

In a special case called resonance, energy cannot be transferred away from the pressure field. Resonance occurs when the wave group velocity, the wave phase velocity, and the velocity of the pressure field or wind speed are equal. In this case, equal phase and group speeds cannot propagate energy away, and the local wave amplitude grows. In shallow depths of 55 meters at Utqiaġvik, resonance can occur in 1-meter thick ice when winds at 15 m s^{-1} force a wavenumber of 0.0575 m^{-1}, or a wavelength of 110 m (Figure 4). For thicker ice, the storms must move faster in order to have resonance. Resonant conditions allow wave energy to accumulate and the wave amplitude to grow.
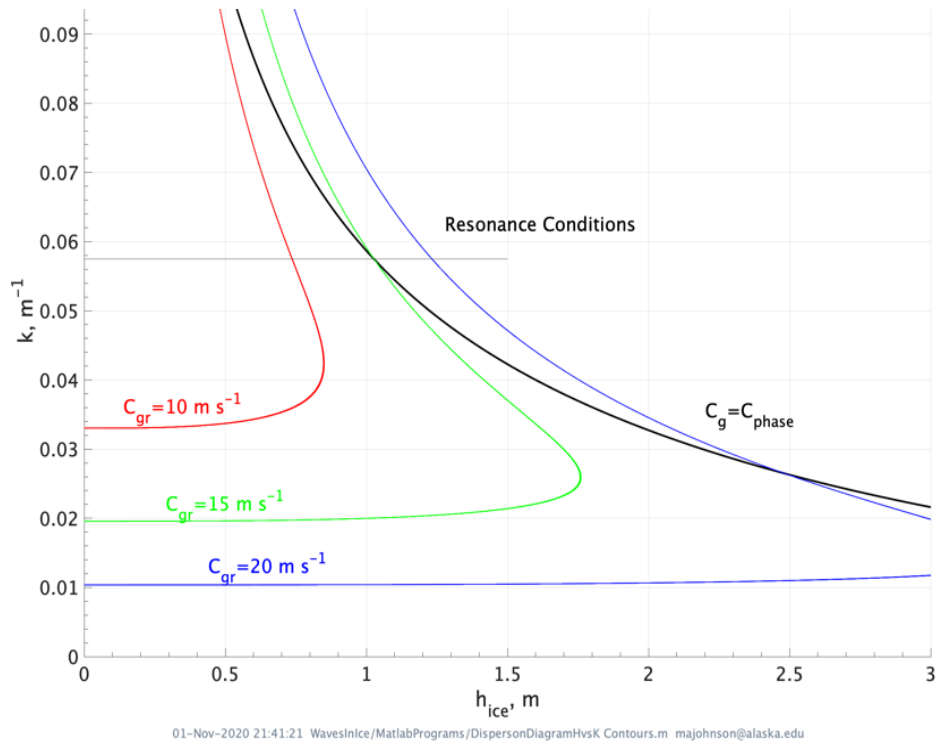
Figure 4. Ice thickness, H_{ice}, versus wavenumber, k, for resonance condition where the wave C_{phase} and $C_{group,}$ velocities, and the velocity of the atmospheric pressure field are equal. For ocean depths of 55 m and 1-meter ice thickness, the growing wavenumber, k, is ~0.0575 m^{-1}.

METHODS

The work described in this report builds from the knowledge and experience gained in 2015 fieldwork conducted with colleagues investigating wave-induced ice motion in a fjord near Longyearbyen, Svalbard. Dr. Graigory Sutherland led that effort for the laboratory of Dr. Atle Jensen, University of Oslo. The team, now including Dr. Jean Rabault, continues to develop a wave-ice sensor that uses the Vectornav VN-100 inertial measurement unit. This work is complementary to ongoing University of Oslo investigations, which generally focus on measurements on un-deformed, relatively thin ice. The work described here is focused on measurements from the thicker and often significantly deformed and ridged landfast ice of the Chukchi and Beaufort Seas.

Two approaches to sensor build-up were used during this project. One approach was to work with a known commercial vendor and have them build-out our sensor design. We chose Pacific Gyre, Inc. because of our prior experience using their dependable, rugged products. The second approach was to pursue in-house technical support led by Jeffrey Simonson, UAF/CFOS IT Administrator.

Multiple design criteria drove the development of the sensors. We needed to directly measure ice motion associated with ocean waves, ice ridging, and ice-ice collisions with instruments operating in the ice environment of the Chukchi and Beaufort Seas. The sensors needed to function unattended for at least several weeks in temperatures reaching -40°C and reliably record data at rates of 10 Hz, and perhaps up to 40 Hz, or more. The sensor hardware needed to collect and store significant amounts of raw data because high sample rates create massive data sets that are cost-prohibitive to telemeter using conventional approaches. We opted to recover data from the sensors and analyze it after recovery. One goal was to identify critical data that might be telemetered in the future as part of an "early warning system" operating in real-time.

Ice Wave Rider Sensor Development

Sensor design specifications were established by the science and technical team at the University of Alaska and the team at Pacific Gyre, Inc.:

- Use a proven, commercially available Inertial Motion Unit (IMU),
- Record high-resolution data for at least 30 days, unattended,
- Be easy to transport, deploy, and service, with on-site battery replacement,
- Provide sufficient computing power to analyze collected data to support real-time detection of breakout events.

The resulting commercial sensor product, dubbed "Ice Wave Rider" (IWR), included the following features:

Vectornav VN-100 IMU (Figure 5): The Vectornav VN100 IMU was selected after observing its successful deployment in 2015 Svalbard field experiments that measured wave-induced ice motion (see Sutherland and Rabault, 2016 for a field project description and Rabault *et al*., 2020 for sensor information). The VN-100 includes a three-axis accelerometer, a three-axis gyroscope, a three-axis magnetometer, a temperature sensor, and an air pressure sensor. The VN-100 communicates using a transistor-transistor logic (TTL) serial interface, and when connected through the installed single-board computer, stores that data onto non-volatile memory. The data is recorded at 10Hz, and we have

successfully recorded at 40 Hz in laboratory testing. The VN-100 sensor can be controlled with any serial terminal application to avoid using the Vectornav Explorer software, which has operating system limitations. It is possible to send commands to control the sensor performance and connect to the serial port to read the VN-100 output using a terminal emulator. When the VN-100 is in the factory reset configuration, it streams several values asynchronously to the output.

BeagleBone Computer (Figure 5): The Linux-compatible BeagleBone open-source single-board computer provides a powerful, low-cost, and relatively low-power platform to integrate the various components of the sensor. The IMU, satellite transceiver, and GNSS receiver (see below) are connected through TTL serial ports. The non-volatile storage communicates through a standard USB connector. The system is capable of analyzing and storing the IMU data at 10 Hz or more, and various alert algorithms can be easily installed and tested. A large developer community allows users such as Pacific Gyre to leverage software development time with proven existing software solutions. The BeagleBone, the interface between the IMU, the Iridium modem, and the USB stick are temperature-rated down to -40℃.
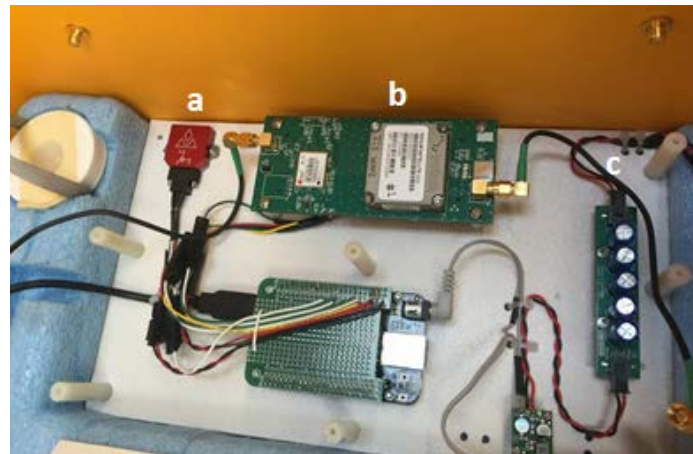
Figure 5. Ice Wave Rider interior with VN-100 accelerometer (a, red unit), BeagleBone single-board computer (b), and supercapacitors (c). The brass connectors at the top allow for external antenna attachment.

Pelican Case Enclosure (Figure 6): The Pelican Storm case is used as a rugged system enclosure. It is relatively light and can be pulled on even ground using its integrated wheels and telescoping handle. The most recent version uses a smaller case that can be transported as carry-on luggage in most commercial airlines. The case can be opened, even in the field, to power-up the electronics, swap batteries, or recover and replace the USB flash drive, which holds the non-volatile collected data.

Alkaline Battery Power Supply with Supercapacitors (Figure 6): The installed alkaline batteries supply ample energy to run the platform for over 30 days, with cold-weather field tests lasting up to 45 days. Alkaline batteries were chosen because they do not include hazardous materials and are easier to transport than lithium batteries. Primary non-rechargeable batteries are used to increase lifespans and eliminate the need for solar recharging, which can be a problem during Arctic winters. A single battery pack powers the entire system. Supercapacitors are installed in parallel to the main battery to lower the output impedance and supply sufficient power in the potentially extreme cold of the Arctic.

Figure 6. Three battery packs next to the control switch in an Ice Wave Rider unit. The USB flash drive is at the back of the case, easily accessible for field swap-out.

Iridium SBD Telemetry (Figure 7): The eventual goal of deploying the sensors is to warn of breakout events by flagging important data events and alerting forecasters. Because deployments are in remote areas, possibly far from installed terrestrial cellular networks, it is necessary to use a satellite telemetry system. Iridium, a low-earth and polar-orbiting system, provides excellent low-power coverage in the Arctic. The lowest-power, lower-cost Iridium SBD channel is sufficient to transmit the flagged data as alerts. Two cables exit the IWR (Figure 7), one connecting to the Iridium and the other to the GPS external dome antenna. The antenna requires a 3/4" NPT threaded pipe to keep it upright and out of the snow.

Figure 7. White PVC caps protect the antenna connectors that pass through the Pelican case to the external antenna.

GNSS Positioning: The sensors are generally deployed at a fixed location on landfast ice. Exceptions include our two Beaufort Sea deployments on the drifting U.S. Navy ICEX2018 and ICEX2020 ice camps. An installed global navigation satellite system (GNSS) receiver can calculate the platform position using the GPS/QZSS, GLONASS, BeiDou, or Galileo system. The installed receiver can also augment those positions with SBAS corrections when available. The calculated sensor position is transmitted along with battery voltage as status information in the real-time Iridium SBD data stream.

Generic Non-Volatile USB Flash Data Storage: Data collected from the IMU are stored on a USB Flash drive in real-time. The drive is easily unplugged from the sensor hardware to archive large data sets for post-processing. When the IMU is sampling and logging 10 Hz data, 1 hour of data requires 10 kilobytes of storage, which means that a 3 GB USB stick can hold more data than the battery capacity, so there is no issue of filling up the memory stick. The USB Flash drive can be swapped out in the field. Upon recovery, the raw binary data from the IMU is converted to csv and/or Matlab formats via the BinaryConfigTool executable supplied by Vectornav.

Initial Ice Wave Rider Deployments and Testing

The first prototype IWR, completed in Fall 2016, used three internal battery packs that provided 150 Amp-hours of capacity, with the system drawing 250 milliamps. The batteries were wired for 12V DC, and a step-down transformer inside the IWR converted to 5V DC. The Vectornav requires a minimum of 3.2V DC with an absolute max of 5.5V DC.

The IWR was programmed to log GPS position at 10-minute intervals to confirm proper operation of the unit immediately after deployment. Generally, once the updates looked normal online, the interval was changed to 4 hours. At the start of this project, only date, time, GPS position, and battery voltage were sent through the iridium link.

The first unit meeting the design features was shipped to Fairbanks for outdoor, cold-weather testing in early December 2016. The unit was deployed on stable sea ice in Elson Lagoon, Alaska, from December 21, 2016, through January 5, 2017 (Figure 8). The IWR successfully measured accelerations at 10Hz, storing all data on a 64GB USB flash drive. It ran successfully for nearly 1200 hours (~50 days) when air temperatures averaged around -13°C. This field test demonstrated the sensor design would work in cold conditions.

Figure 8. First IWR deployment on Elson Lagoon (December 2016) with an external antenna and ratchet straps to secure to the ice.

Following the success of the first Elson Lagoon deployment, a second IWR was built and delivered to the University of Alaska Fairbanks (UAF) in February 2017. Both IWR were shipped to Utqiaġvik and deployed on Elson Lagoon ice on March 24, 2017, where they successfully collected data (510 and 620

hours). As collected data were downloaded and processed, we developed a software library capable of visualizing the results and identifying wave signals, if present. Software library development continued as instruments acquired new measurements from real-world conditions.

To establish the background levels for acceleration and other measured parameters when the sensor is subject to little or no motion, we placed two IWRs on snow-covered ground and inside the seismic vault at the University of Alaska Fairbanks Alaska Earthquake Center (AEC) from 11 December 2017 through 29 January 2018 (Figure 9). We hoped to compare the measurements from the IWRs with any data from earthquake activity that might occur at the time of our deployments. The AEC instruments, calibrated to measure seismic activity, measured ground motion during our deployments but the ground motion was not strong enough to be recorded by our instruments. The measurement background levels are discussed in detail in "RESULTS." We placed an IWR inside on a concrete ground floor at UAF for three-days to further establish background measurement levels. These deployments established the "background noise" for the IWRs and showed they could collect and telemeter data continuously for ~50 days in cold, winter temperatures.

Figure 9. IWRs undergoing testing outside (left) and inside (right) at the University of Alaska Fairbanks Alaska Earthquake Center.

We initially anticipated placing the external antenna atop a nearby ice ridge to get clear GPS and Iridium signals for deployments on ridged or deformed landfast ice, so the IWR was designed with ~20 Feet of coaxial cabling between the sensor and antennas; however, mounting the antenna on a ridge proved unnecessary. We then mounted the external Iridium/GPS directly to the Pelican case with an external mount (Figure 10). This design, used in 2017 and 2018, proved cumbersome during deployments and unnecessary under the field conditions we encountered. In December 2018, we tested an internal antenna design that eliminated the external cabling. It proved far easier to transport and deploy. Beginning in January 2019, all IWR deployments used this upgraded design.

Figure 10. External antennas with yellow mounts to attach directly to the IWR Pelican case.

Deployments through 2019 established that the IWRs can record accelerations that are visibly larger than background levels. We speculate that the large accelerations are caused by ice-ice collisions. Based on data acquired to date, we chose a vertical acceleration threshold value of ±1.0 m s^{-2} as an indicator that the ice conditions were "dynamic." The IWR's BeagleBone computer was programmed to sum, over a user-selected interval, the number of vertical acceleration values that exceeded this threshold, and then telemeter that total, as "z-counts," with the other data. The result is a near-real-time monitor of "extreme" or "dynamic" ice activity.

While the IWRs show success in measuring comparatively large ice-ice collision events, likely from winds or currents driving drifting ice against the landfast ice, signals clearly due to waves were not measured before 2020. Was there an issue with the sensors? Were there no waves where the sensors were deployed? Was the ice too thick in the Chukchi Sea region to allow for wave propagation? Johnson discussed these and other questions with Drs. Atle Jensen and Jean Rabault in August and September 2019. After measurements over several field seasons in Svalbard and Norway, Rabault and Jensen found the sensor's signal-to-noise ratio could be improved by changing the VN-100's filtering protocol. The default filter setting essentially block-averages the data before storing it. The VN-100 operates internally at a factory-set rate of 800 Hz, and in our case, saves data at 10 Hz. At 10 Hz, the IWR effectively subsampled the Vectornav internal 800 Hz data stream, storing every 80th value. We reprogrammed the VN-100 filter settings for it to _average_ sequences of 80 values, which were then saved at 10 Hz. The result was significantly reduced noise and improved signal. This filtering was imposed on the existing IWR sensors and incorporated into new sensor purchases.

Six new IWRs were constructed with the revised filter setting and telemetry of "z-counts," as described above. The newer units were also smaller, lighter, and easier to deploy than previous prototypes and had the power to last several weeks. The new sensors telemetered time, location, and battery life, plus the real-time count of accelerations that exceed the ±1.0 m s^{-2} threshold. This is another step toward a real-time sensor for alerting users of ice conditions, and this approach was adopted for our 2020 field season with deployments on landfast ice near Utqiaġvik and opportunistically on drifting ice in the Beaufort Sea with the U.S. Navy's ICEX2020 ice camp.

The IWRs measure vertical acceleration, but what is the actual displacement of the ice associated with the measured accelerations? While accelerations can be easily calculated from displacements by differentiating twice, the inverse operation (i.e., double integration) can lead to spurious displacement values when applied to noisy, real-world acceleration data.

To overcome this problem, we apply the approach of Kohout *et al*. (2015) to find the displacements. The double integration is performed in the frequency domain using Fourier analysis and then transformed back into the time domain. To prevent abrupt frequency cut-offs, which can add noise (amplitude) to the displacement, frequency response weights, *H(f)*, are applied for the 2 to 20-second wave band. This frequency-dependent cut off is applied as follows using a half-cosine taper, *H(f)*:

$$H(f) = \begin{cases} 0, & 0 < f < f_1 \\ \frac{1}{2}\left[1 - cos\left(\pi \frac{f-f_1}{f_2-f_1}\right)\left(\frac{-1}{2\pi f^2}\right)\right], & f_1 \leq f \leq f_2 \\ \frac{-1}{2\pi f^2}, & f_2 \leq f \leq f_c \end{cases} \qquad \text{(Equation 2)}$$

where f_1=0.02 Hz and f_2=0.03 Hz, suitable for waves with periods between 2 and 20 seconds. Data and analysis from the field deployment are presented in "RESULTS."

In-House Approaches

Two designs were pursued at UAF. The first uses the SVS-603 wave sensor manufactured by SeaView Systems, Inc., a sensor often used in traditional ocean wave buoys. The SVS-603 requires a power supply between 5V and 30V DC. Its power consumption varies depending on the power supply, consuming between 136 mW at 5V and 150 mW at 12V. The SVS-603 draws 11 mA. When powered by a 12V UB12350 gel battery (similar to a traditional car battery but sealed) rated at 35 AH, the system is expected to last 132 days at 25°C. This unit was field-tested at the AEC, where it ran for ~50 days in temperatures around -10°C.

The SVS-603 accelerometer is embedded in a fully developed circuit board (Figure 11) that allows for on-board data processing, including calculating and outputting Fast Fourier transform (FFT) coefficients (i.e., "spectral analysis" data), significant wave height (SWH), and other user-selected parameters.

Figure 11. SVS-603 circuit board from SeaView Systems, Inc.; micro-USB connector at the top, micro-SD card at lower center, and watch battery at lower right to preserve clock and sampling settings. The green connector at the lower left is for data and external power supply.

The SVS-603 stores the raw accelerations and summary data to an internal micro-SD card. The unit connects via a micro-USB directly to a computer cable for data download and programming parameters, including user-defined values for sampling rate, raw data output, averaging interval, magnetic declination, and frequency cutoff for spectral calculations. The sensor requires a terminal emulator to communicate using a PC's com3 port. We mounted the sensor in a non-metallic, high-impact, flat top, molded NEMA 4X junction box (part PN-1331-C, available through Bud Industries for $11.50 each).

The SVS-603 is a significantly more expensive accelerometer package (~$6300) than the VN-100 IMU (~$1300). Seeing potential use in a multi-sensor "early warning network," SeaView Systems, Inc. discounted the purchase of two sensors (~$1,500 each) and loaned a third unit for testing and evaluation. The three SVS-603 sensors were received in Fall 2016 and mounted in NEMA polycarbonate junction boxes.

During laboratory tests of the SVS-603, after data collection was paused to calculate FFT and SWH, the units resumed raw data collection with a small data drift in the record. This problem was reported to SeaView Systems Inc., and they revised their User Manual regarding parameter settings that control the sampling rate. To avoid the sensor reloading its calibration (i.e., maintain our initial setup), we were advised to use the following settings: INTERVAL of 10,000, AVR of 10, RECAL to 0, RESETCOUNT to 0 (Tim Crandle, personal communication).

 We found that the SVS-603 was highly sensitive to the thickness of the micro-SD card used to store output data. After some experimentation, we settled on SanDisk brand SD cards (Figure 12). Other testing examined the SVS-603 data output after attaching it to pendulums of different lengths and mounting it to a rotating turntable spinning at different rates. To do this, a 9V battery was wired inside the SVS-603's NEMA housing box, so the unit was fully self-contained, avoiding the need for wiring to an external power supply. For a swinging pendulum of length L, the period is $T = 2\pi\sqrt{L/g}$ Where g is gravity. No problems were found with the spectral results from the SVS-603, and these tests helped us understand the unit's performance, including how to program it and download and interpret data. The results from these preliminary tests are not discussed further in this report.
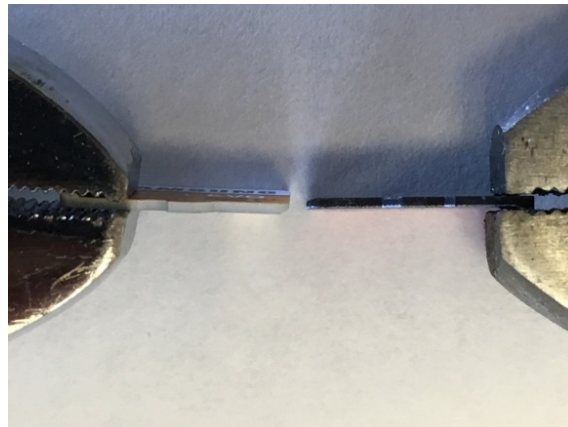
Figure 12. Micro-SD card comparison. The thicker SanDisk card was most reliable.

After laboratory testing of the SVS-603, two prototypes, "Able" and "Baker," were constructed, powered by a sealed gel UB12350 battery (Figure 13). Able and Baker were then deployed at AEC to determine the sensitivity of the SVS-603 sensors (Figure 9). The units were put on level ground and recorded data for ~44 days from 12 December 2017 through 25 January 2018.

Figure 13. Sensor Able in Pelican case with 12V battery (at right), charger (upper left), and SVS-603 sensor (lower left). This unit can log data for more than 30 days at -20℃.

The field data, discussed in detail in "RESULTS," indicates this sensor may be best for measuring in locations where large accelerations are expected from ridging or ice-ice collisions. However, the SVS-603 records accelerations only to a resolution of 1×10^{-2} m s^{-2}, so it does not have sufficient sensitivity for measuring wave signals in ice. Because of its lower measurement resolution and the lack of straightforward methodology to add telemetry, we ceased further development with the SVS-603 in 2019 and initiated a second "in-house" approach to sensor development.

For consistency, we wanted the second "in-house" approach to use the same IMU, the VN-100, as the IWRs. Using the VN-100 sensor, we could use Vectornav's C++ libraries and generate binary, asynchronous streaming up to 80 Hz with quick and easy parsing from binary to text data. We also wanted to create as small and compact a sensor as possible. Further, we designed a system around the LINUX open-source computer system using Arduino and the Raspberry Pi Zero hardware. Arduino and Raspberry Pi are commercially available microcontroller boards with considerable open-source software available to a large user community. Any system built using LINUX, Arduino, and Raspberry Pi components could be quickly cloned to achieve rapid scale-up to multiple systems.

We wanted this new system to send and receive data wirelessly and share data over the internet where it could be easily monitored, controlled, and packaged for stakeholders. Transmitting data from remote, on-ice sensors to shore can be done using one of several types of radio transmission, such as cellular, satellite, Wi-Fi, Bluetooth, XBee (Figure 14), or some other custom transceiver. XBee is a commercially produced product by Digi International that acts as both a transceiver and receiver for radio communication. XBee supports wireless peer-to-peer and point-to-multi-point network communications at 250 kbits s^{-1}.

Data can be sent and received via a system of XBee radios deployed in the field with at least one radio transmitting to a shore-based Arduino Ethernet Base Station connected to the Internet. XBee radio offers

a low-cost, low-power system with a range of up to 28 miles. Data can be streamed from the XBee on the remote sensor to a base station on the shore, then sent out over the Internet. XBee has the capability for a mesh network where the most remote sensors, out of range of the base station, can relay their data along a trail of other XBee radios, thus providing an unlimited range. The base station can aggregate data from all sensors and present them to interested users anywhere on the Internet.

Figure 14. XBee radio module wired into the VN-100 sensor system.

The data aggregator may be a simple set of flat files, or a system better designed to collect sensor data and present it in more useful ways. Zabbix is one such system designed specifically to monitor changing information like that generated from the sensors used here. Zabbix is open-source, enterprise-class monitoring software providing monitoring metrics, network utilization, and other relevant data streams. Zabbix provides different data handling methods, a graphical representation of incoming data in real-time (Figure 15), and the ability to use monitoring triggers to act on specific conditions in the real-time data. For example, Zabbix includes a notification mechanism that can be configured to send email alerts for any user-flagged event, ideal for an event-triggered "early warning system." This design could form the foundation for an early-warning system outside of cellular reception.
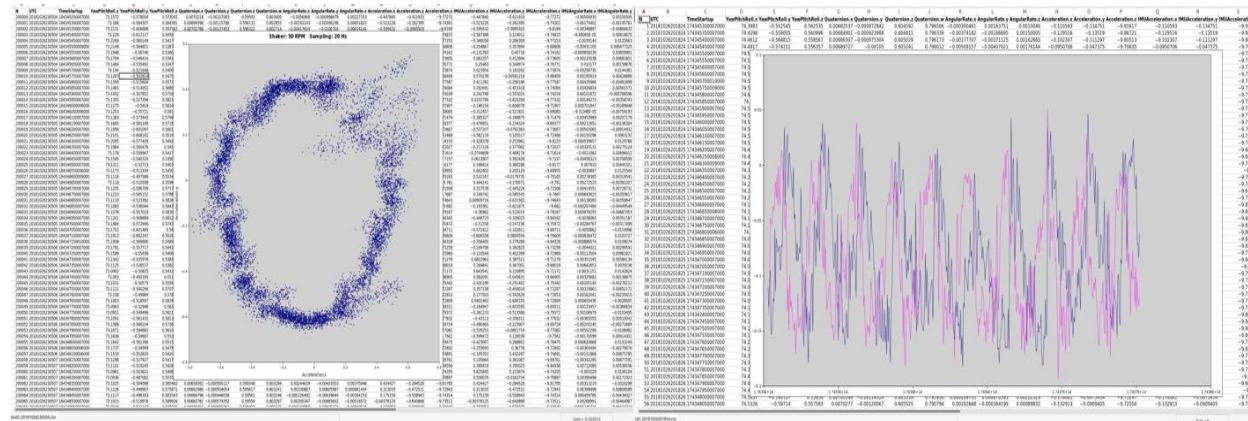
Figure 15. Screen snapshots of Zabbix display showing numerical and plotted data from the VN-100 real-time transmission over an XBee radio. X versus Y accelerations (left) and X and Y acceleration timeseries (right) while the sensor was on the rotating turntable shown in Figure 16.

A prototype sensor, dubbed "Metis," was designed and built around the VN-100 and a small LINUX computer system to control data sampling and storage. This unit was tested using the XBee radio system (Figure 16) and programmed to record at a sampling rate of 40 Hz. Laboratory experiments indicate that this prototype could acquire data at 40 Hz, transmit multiple data channels via XBee to an internet base station, and display the results via Zabbix servers on a laptop (Figure 15). To work in the field, a series of XBee radios would need to be deployed across landfast ice to relay data in real-time. A five-day test on landfast ice (without XBee) in Utqiaġvik acquired data at 40 Hz from the field. Data from that test are in "RESULTS."
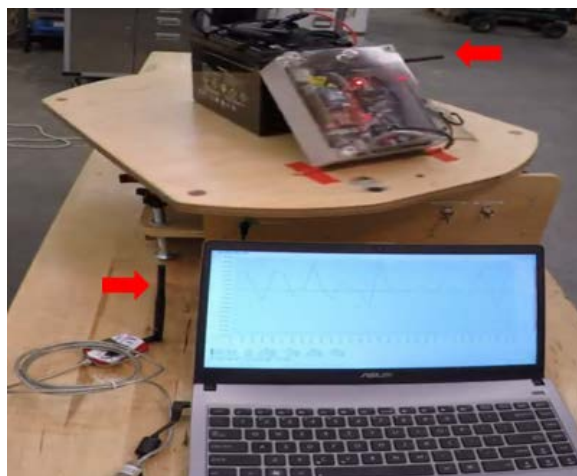
Figure 16. VN-100 sensor Metis on a rotating turntable transmitting via XBee radio to laptop with real-time data display. Note XBee antennas on sensor box and near laptop (red arrows).

Deployment Strategies

Personnel from UIC Corporation, Utqiaġvik, Alaska, assisted in many of the deployments described here (Figure 17). Sensors were shipped via Alaska Airlines to Utqiaġvik and picked up by UIC. Deployment instructions included with each sensor requested photographs facing N, S, W, and E with the sensor in view and, additionally, GPS location for Able, Baker, and Metis deployments. However, we did not get pictures and/or GPS locations for some deployments. Future sensor designs must include telemetry of the location to make for easier deployments.

Figure 17. UIC personnel arming Able before deployment (left), IWRs loaded on sled for transport (center), and IWR deployed on Chukchi Sea landfast ice (right).

RESULTS

Appendices I and II show complete timeseries of all relevant sensor data as raw data except for converting the sensor's internal data counter to Coordinated Universal Time (UTC) and eliminating any start and end records acquired during sensor transit. The "Data" section below presents select measurements, acquired during laboratory testing and field deployments, that are relevant to understanding sensor performance. The following sections present results from the different sensors used in this study. Data are from Able and Baker using the SVS-603 and Metis and the IWRs using the VN-100. The SVS-603 data are accelerations in coordinate directions North-East-Up. The VN-100 data are in North-East-Down, plus the heading attitude references yaw, pitch, and roll (Figure 18).

The section "Breakout Event" presents IWR measurements acquired adjacent to a Chukchi Sea landfast breakout event. The section "Waves in Ice" presents computed wave displacements and results of their spectral analyses and examines the wave dispersion relationship in light of our measurements of wave propagation in ice.
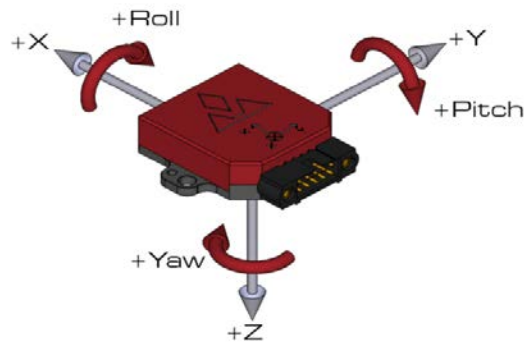
Figure 18. XYZ sensor coordinates are converted to North-East-Down based on the local, sensor-measured magnetic field. The heading attitudes, yaw, pitch, and roll, are shown (from the Vectornav User's Manual.)

Data

The figures included with the text below provide detail not found in the Appendix figures. The field measurements are generally dominated by long periods of relative quiet, punctuated by shorter periods when the measured motion is well above the background levels. For example, there are short-lived "spikes" in acceleration and abrupt changes in the heading attitudes (yaw, pitch, and roll) that visibly stand out in the data timeseries.

For this Report, we adopt the term "jolt" to mean an abrupt change in the measured signal that persists for a few seconds. We use this terminology following George *et al*. (2004b), who noted on-ice users felt a "jolt" in the landfast ice just before a 1997 breakout event. Here, "jolt" is used without implying ice breakout or detachment. In addition to jolts in the timeseries data, another common characteristic is acceleration and/or attitude varying above background levels for minutes or longer. When measured values of acceleration or attitude persist above background levels for many seconds or minutes, one can imagine that the ice-ice interactions might cause the ice to "shake" or "rumble" as felt by the sensors or people on the ice. We adopt the term "rumble" to mean a signal that is persisting for minutes or more and is visibly above background values.

SVS-603

Acceleration data collected by units Able and Baker are shown in Appendix II. All data are in the North-East-Up (NEU) coordinate system, a conversion from XYZ coordinates registered on-board by the SVS-603 based on real-time measurements of the local magnetic field. Able and Baker were deployed at the UAF AEC seismic facility from 11 December 2017 to 30 January 2018. Table 1 lists the deployment details for sensors tested on land at the AEC and on a concrete slab at UAF.

Table 1. Test deployments on land.

Sensor	Location	Latitude	Longitude	Start	End	Duration (hours)
IWR1	AEC	64.873	-147.8615	11 Dec 2017	29 Jan 2018	1174
IWR2	AEC	64.873	-147.8615	11 Dec 2017	30 Jan 2018	1196
Able	AEC	64.873	-147.8615	11 Dec 2017	30 Jan 2018	1172
Baker	AEC	64.873	-147.8615	11 Dec 2017	30 Jan 2018	1184
IWR1	Slab	UAF	UAF	22 Nov 2018	25 Nov 2018	81
IWR2	Slab	UAF	UAF	22 Nov 2018	25 Nov 2018	81

Appendix II, Figure AII.1, shows abrupt shifts in the Up acceleration recorded by Able. Variability in both horizontal accelerations (N and E) become visibly larger just before 31 December, about the same time that the Up acceleration shows a shift to larger values. This signal contrasts that of Baker (Figure AII.2), deployed nearby, which shows large variations in the horizontal accelerations after 31 December. After the data were reviewed, the measured levels of "background" were deemed excessive and likely to mask any signals from waves in ice. The variability in NEU for both Able and Baker is larger than that of the IWRs deployed at the same time and an order of magnitude greater than the IWRs with the revised on-board filtering (discussed below).

Figure AII.3 shows a 32-hour deployment of Baker on landfast ice north of Prudhoe Bay, Alaska, opportunistically carried out by Dr. Steve Okkonen (UAF). There are visible data "shifts" in the NEU accelerations. Due to the obvious shifts in the raw data, no discernable signal has been clearly identified or associated with on-ice phenomenon.

Able was deployed for ~4-days on drifting sea ice as part of ICEX2018. The data were unrecoverable from the micro-SD card (see discussion in "METHODS"). The unit was tested before it left Fairbanks, but the micro-SD became corrupted sometime during the deployment or transit to Fairbanks.

Figure AII.4 and AII.5 show data from Able and Baker deployed in May 2018 on Chukchi Sea landfast ice near Utqiaġvik north of IWR1 and IWR2 and in proximity to IWR3 and IWR4. Able shows a diurnal signal in NE acceleration and large variations in Up. Baker shows several large jolts in NEU accelerations, with values as large as 7 m s^{-2}. Jolts at 19:22 UTC 12 May and 19:04 UTC 13 May, align with jolts in accelerations measured by IWR4 deployed nearby (see Figure AI.21). These large acceleration jolts are the first such recorded measurements of simultaneous signals.

Figures AII.6 and AII.7 show data from Able and Baker, deployed in early May of 2019 for ~17 days on Chukchi Sea landfast ice using Frederick Brower's trail. There are several large accelerations on 14 and 15 May, but no other identifiable signals in either deployment.

Based on too much "noise" present in Able and Baker data, the higher cost of the SVS-603 sensor, the failure of the micro-SD card under field conditions, and lower measurement resolution, we halted further development with this sensor after the 2019 field season. Though SVS-603 sensor deployments were discontinued, the data collected indicate the sensor can measure ice-ice collisions (jolts) with acceleration values above ~0.4 m s^{-2} and might be useful in an early warning system designed for alerting users of significant ice motion. However, the SVS-603 lacks a temporally stable signal and is insufficiently sensitive to measure signals produced by waves propagating in ice for the conditions encountered during this study.

Metis

Metis was deployed from 29 April – 3 May 2019 on Chukchi Sea landfast ice. The VN-100 data were recorded at 40 Hz and did not show any significant motion. A 5000-second (~1.4 hours) snapshot is shown in Figure 19 for the attitude headings, yaw, pitch, and roll, and the XYZ acceleration. The values are relatively steady. This deployment was before the upgrade of the filter setting for the VN-100.

One problem encountered with the deployment of Metis, Able, and Baker is uncertainty in the exact deployment location (latitude, longitude), which had to be acquired by the deployment team. This demonstrates the critical need to incorporate GPS data into the telemetry data stream to ensure that the sensor location is known, as is done for the IWRs discussed next.
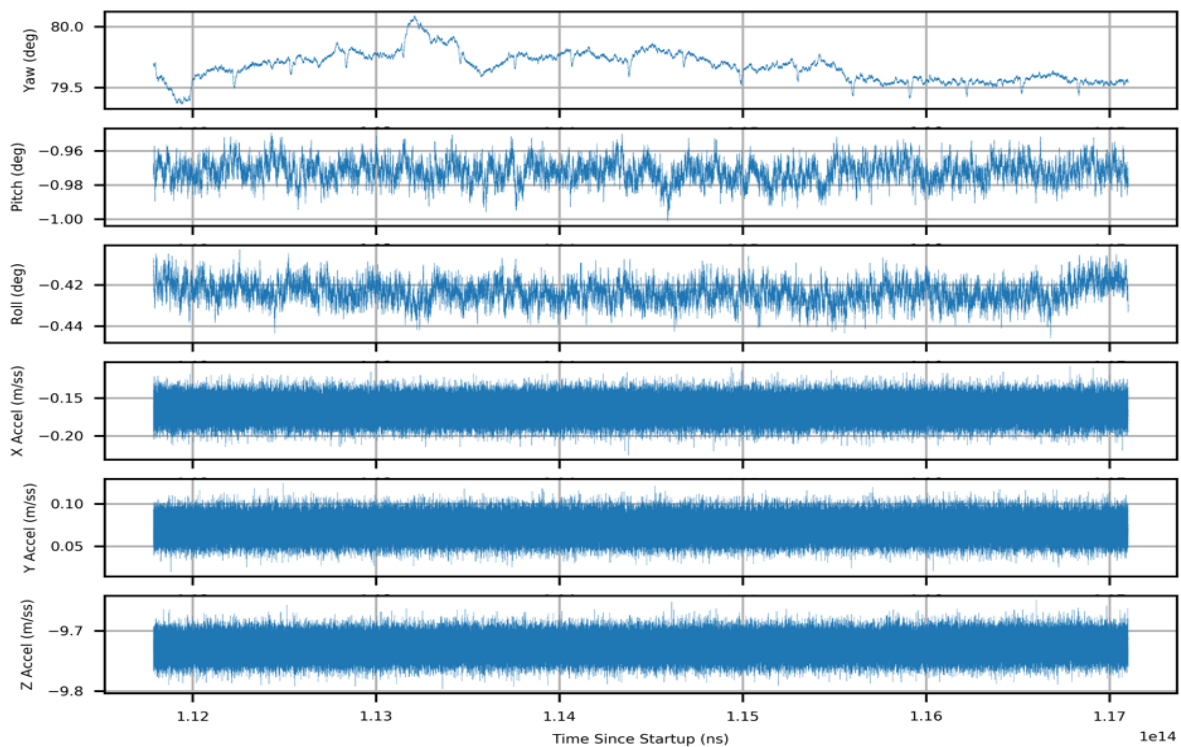
Figure 19. Metis Chukchi Sea landfast ice timeseries of yaw, pitch, roll (top three panels), and XYZ accelerations (bottom three panels) for a 5000-second snapshot at 40 Hz.

Ice Wave Riders

Ice Wave Rider sensors (IWR) collected and stored (on a USB drive) attitude headings (yaw, pitch, roll), Quaternions (a single vector value of attitude that does not have numerical instability at 0°, 90°, 180°, and 270° headings), angular rates, accelerations in the XYZ sensor frame, and accelerations in the North-East-Down (NED) coordinate system derived from the sensor's 3-axis magnetometers and 3-axis gyroscopes. For deployments prior to spring 2020, atmospheric temperature and barometric pressure were also measured by the VN-100 and stored on the USB drives. For this Report, we focus on the NED acceleration data and the sensor attitude heading data (yaw, pitch, and roll) collected at 10 Hz.

Data from all IWR deployments are plotted and shown in Appendix I. Figures AI.1 and AI.2 show data from a ~44-day test when the IWRs were outside at the AEC seismic facility. The variability in the NED accelerations is generally less than 0.1 m s^{-2} in N and E, with some drift in D over the record length. Pitch and roll vary within 0.5 degrees with some drift in yaw. These instruments were on level ground undergoing freezing which may account for some of the temporal drift. Figures AI.3 and AI.4, from a 3.3-day test with the IWRs placed on an indoor concrete slab, show NED varying less than 0.1 m s^{-2}, with pitch and roll varying less than 0.1 degrees. There was no drift in NED, yaw drifted less than 0.5 degrees, and pitch and roll drifted less than 0.05 degrees. In spring 2020, we applied the revised filtering configuration to the IWRs deployed on Elson Lagoon. Those NED accelerations vary less than 0.02 m s^{-2}, a 5-fold reduction in the noise.

Elson Lagoon

The first on-ice measurements were conducted on the relatively flat and stable ice of Elson Lagoon northeast of Utqiaġvik in December 2016 and repeated in early 2017, 2019, and 2020 (Figure 20). IWR1 2016, IWR1 2017, and IWR2 2020 were deployed at the same location. Figure 21 shows Elson Lagoon deployment conditions. Table 2 lists details of the Elson Lagoon IWR deployments.
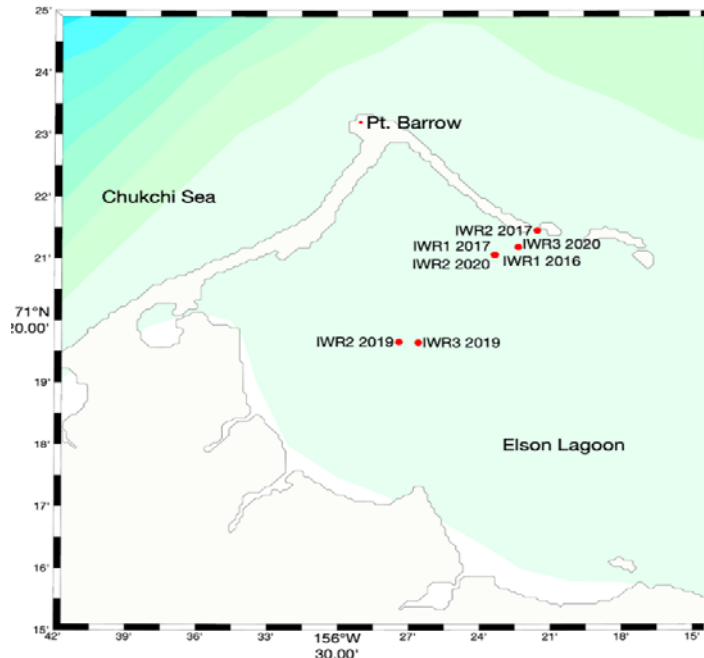
Figure 20. IWR Elson Lagoon deployment locations for 2016, 2017, 2019, and 2020.

Figure 21. IWR Elson Lagoon deployments 2017 (left), 2018 (middle), and 2019 (right).

Table 2. Elson Lagoon deployments on stable ice.

Sensor	Location	Latitude	Longitude	Start	End	Duration (hours)
IWR1	Elson Lagoon	71.3509	-156.3889	22 Dec 2016	4 Jan 2017	332
IWR1	Elson Lagoon	71.3509	-156.3880	24 Mar 2017	15 Apr 2017	513
IWR2	Elson Lagoon	71.3575	-156.3582	24 Mar 2017	19 Apr 2017	623
IWR2	Elson Lagoon	71.3276	-156.4565	19 Mar 2019	9 May 2019	1234
IWR3	Elson Lagoon	71.3276	-156.4428	19 Mar 2019	8 May 2019	1207
IWR2	Elson Lagoon	71.3509	-156,3884	4 Apr 2020	28 May 2020	1326
IWR3	Elson Lagoon	71.3518	-156.3719	3 Apr 2020	2 June 2020	1446

The 2016 and 2017 deployments have NED accelerations that vary around a background of ± 0.1 m s^{-2} (Figures A1.5 through A1.11), similar in variations to the AEC tests. None of the Elson Lagoon deployments showed evidence of waves in ice. In many cases, the air temperature varies similarly to the Down acceleration. At this time, we are uncertain whether this is a direct effect of the temperature on the sensor or temperature-induced ice motion, and further analysis is required. In the analysis of waves, all linear trends are removed before computing displacements and spectra.

ICEX2018 and ICEX2020 Drifting Ice

Five sensors were deployed on drifting ice in the Beaufort Sea as part of the U.S. Navy ICEX campaigns: Able and two IWRs in 2018 and two IWRs in 2020. Deployment details are listed in Table 3.

Table 3. ICEX2018 deployments on drifting sea ice in the Beaufort Sea.

Sensor	Location	Latitude	Longitude	Start	End	Duration (hours)
IWR1	ICEX	72.337	-148.1561	17 Mar 2018	21 Mar 2018	90
IWR2	ICEX	72.309	-148.7886	17 Mar 2018	21 Mar 2018	89
Able	ICEX	72.337	-148.1561	17 Mar 2018	21 Mar 2018	90
IWR5	ICEX	71.158++	-152.4++	7 Mar 2020	18 Mar 2020	264
IWR6	ICEX	71.158++	-152.4++	7 Mar 2020	15 Mar 2020	197

The ICEX2018 data from sensor IWR1, placed within 100 meters of the camp's airstrip (Figure 22), had multiple "spikes" in the accelerations that are visibly above background levels (Figure 23).

Figure 22. IWR1 and Able south of the ICEX2018 airstrip at deployment (left) and seven days later (right, note plane in background).
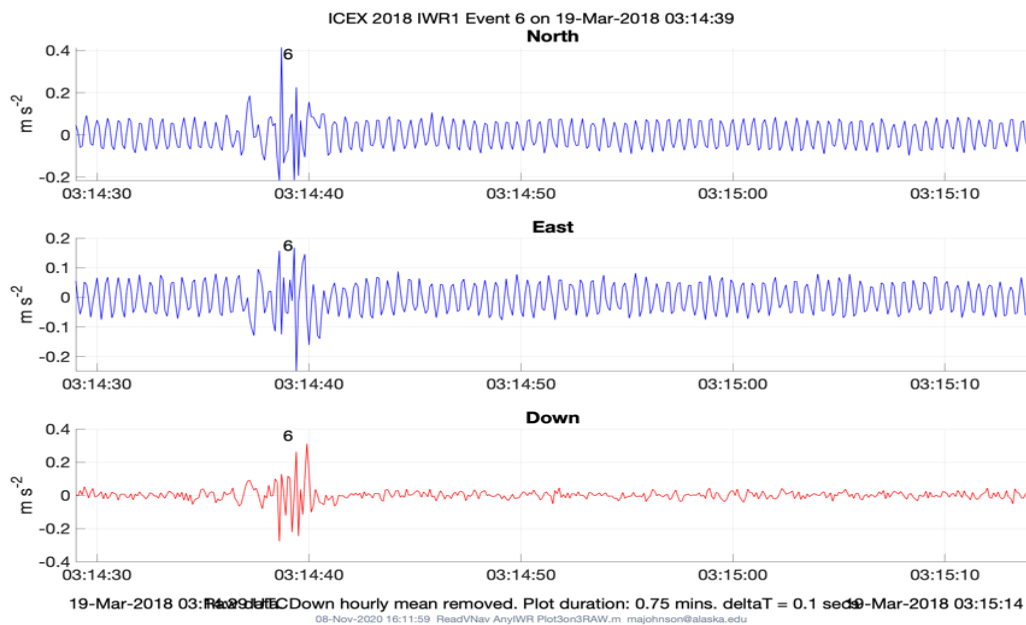
Figure 23. IWR1 ICEX2018 NED accelerations from Event 6 acquired near the airstrip. The vertical and horizontal accelerations due to planes landing on the ice are well above background values.

The timing of spikes generally matches the logged times of plane landings and take-offs that serviced the camp. As an aircraft travels along an ice runway, the moving load creates an ice-wave that propagates away, much like the wake behind a boat moving through water. In this case, the "wake" was recorded by the nearby IWR. Copies of these data are with Dr. Henrik Kalisch, University of Bergen, Norway, who is comparing them with theory. Any future measurements of moving loads should be acquired at higher rates of at least 40 Hz as these data appear aliased by the 10 Hz sampling rate. These data are not discussed further.

In 2020, IWR5 and IWR6 were deployed at the U.S. Navy ICEX Camp Seadragon drifting in the Beaufort Sea. IWR5 was deployed on multi-year ice ~300 meters north of the runway (Figure 24), and IWR6 was deployed on first-year ice ~60 meters south of the runway. Both IWRs were recovered with data about 11 days later. Raw data plots are shown in Figures AI.12 through AI.15. These IWRs were configured with the revised filtering parameters and programmed to telemeter counts of "extreme" events where the IWR's on-board BeagleBone computer monitored the 10 Hz data stream in real-time to count the vertical accelerations exceeding ± 1 m s^{-2}. Total counts were telemetered at the programmed reporting interval, generally one hour. This test confirmed the ability of the IWRs to monitor "extreme" events in real-time.

Figure 24. IWR5 ICEX2020 location looking toward Camp Seadragon.

Based on the two ICEX2020 sensors' hourly GPS positions, the camp drift changed from northward to southeastward around noon on 13 March 2020 and shifted from eastward to southeastward at 2100 on 14 March 2020. Both changes occurred when very strong winds were measured at the camp, and timing aligns with IWR data showing signals consistent with wave propagation. The discussion of waves in ice from ICEX and Chukchi Sea landfast ice are combined and presented in the "Waves in Ice" section.

Chukchi Sea Landfast Ice

In 2018, 2019, and 2020, IWR deployments were made on Chukchi Sea landfast ice to the west and north of Utqiaġvik. The deployment locations are shown in Figure 25, and deployment details are shown in Table 4. The full timeseries of attitude heading and NED accelerations are shown in Appendix I, Figures AI.18 through A1.33.
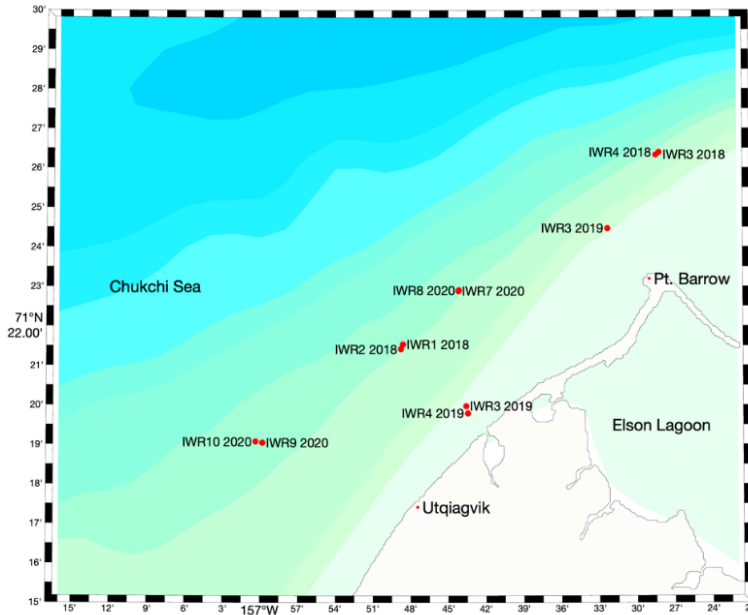
Figure 25. Chukchi Sea IWR landfast ice deployment locations for 2018, 2019, and 2020. Bathymetry increases by 10-meter contours from the shore.

Table 4. Chukchi Sea landfast ice deployments.

Sensor	Location	Latitude	Longitude	Start	End	Duration (hours)
IWR1	Utqiaġvik	71.359	-156.8102	1 May 2018	24 May 2018	575
IWR2	Utqiaġvik	71.357	-156.8130	1 May 2018	24 May 2018	574
Able	Utqiaġvik	~71.359	~-156.8102	1 May 2018	24 May 2018	575
IWR3	Utqiaġvik	71.439	-156.4742	11 May 2018	22 May 2018	263
IWR4	Utqiaġvik	71.440	-156.4701	11 May 2018	24 May 2018	312
Baker	Utqiaġvik	~71.440	~-156.4701	11 May 2018	24 May 2018	312
IWR3v1	Nageak Trail	71.333	-156.7265	20 Mar 2019	20 Mar 2019	21
IWR3v2	Nageak Trail	71.333	-156.7265	20 Mar 2019	28 Mar 2019	173
IWR4	Nageak Trail	71.333	-156.7243	20 Mar 2019	20 Mar 2019	20
IWR4	Nageak Trail	71.333	-156.7243	20 Mar 2019	26 Apr 2019	894
IWR3	Brower Trail	71.408	-156.5387	20 Apr 2019	12 May 2019	525
Able	Brower Trail	~71.408	~-156.5387	30 Apr 2019	16 May 2019	411
Baker	Brower Trail	~71.408	~-156.5387	30 Apr 2019	16 May 2019	409
IWR7	Utqiaġvik	71.3816	-156.7367	1 May 2020	29 May 2020	694
IWR8	Utqiaġvik	71.3819	-156.7362	1 May 2020	29 May 2020	695
IWR9	Utqiaġvik	71.3175	-156.9965	19 May 2020	28 May 2020	214
IWR10	Utqiaġvik	71.3180	-157.0059	19 May 2020	28 May 2020	214

IWR1 and IWR2 were deployed from 1 – 21 May 2018 on landfast ice near a ridge and close to open water west of Utqiaġvik (Figure 26). At ~11:00 on 5 May, IWR1 measured NED accelerations that began to "spike" above the background levels, and yaw began to vary by $\pm 1°$ for the next 24 hours (Figure 27). On May 17, both sensors recorded yaw oscillations lasting for about 12 hours (Figure A1.18). These data suggest that a series of small, measurable jolts may be able to weaken the ice and free it to yaw or rotate about the vertical.

Figure 26. IWR2 and Able on Chukchi Sea landfast ice with open water visible in the background.
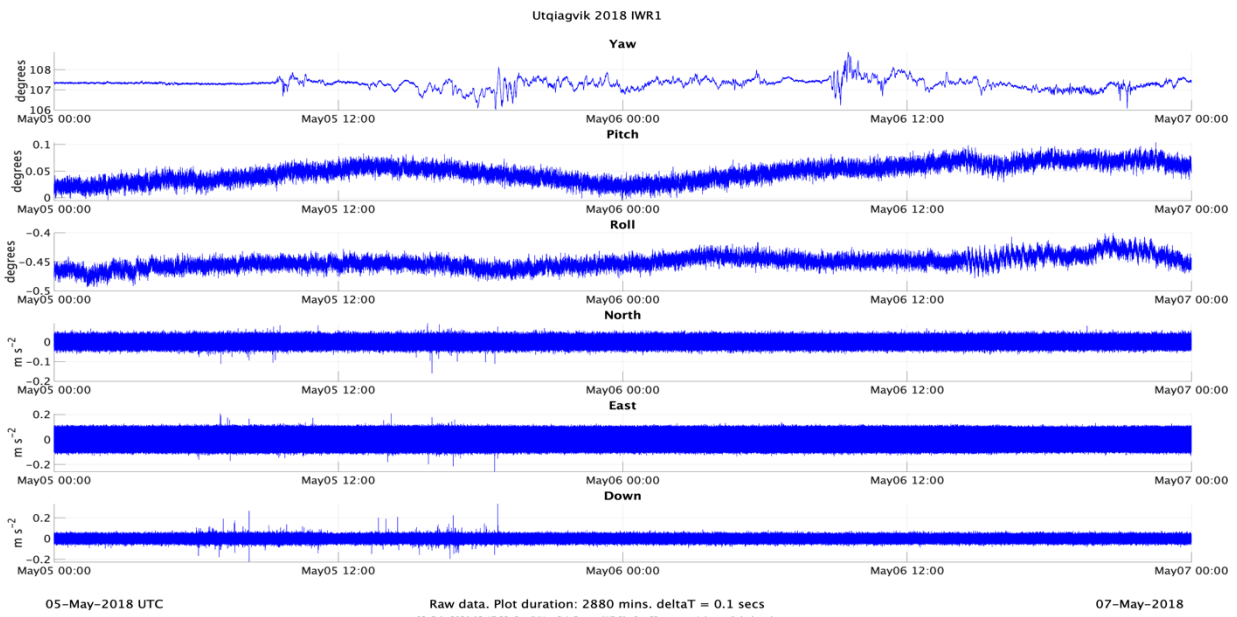
Figure 27. IWR1 Utqiaġvik 2018 record with steady yaw until May 5 that begins to vary $\pm 1°$ as the D and E accelerations reach values of ± 0.2 m s^{-2}.

Sensors IWR3, IWR4, and Baker were deployed north of Point Barrow from 11 – 22 May 2018 (Figure 28). IWR4 and Baker showed jolts in NED at the same time, recorded as abrupt changes in yaw, pitch, or roll (Figure 29). On 12 May, the jolt in Down acceleration was almost 20 m s^{-2} at the same time as yaw changed up to 12° and roll to 6°.

Figure 28. IWR4 and Baker at Point Barrow on landfast ice near open water.
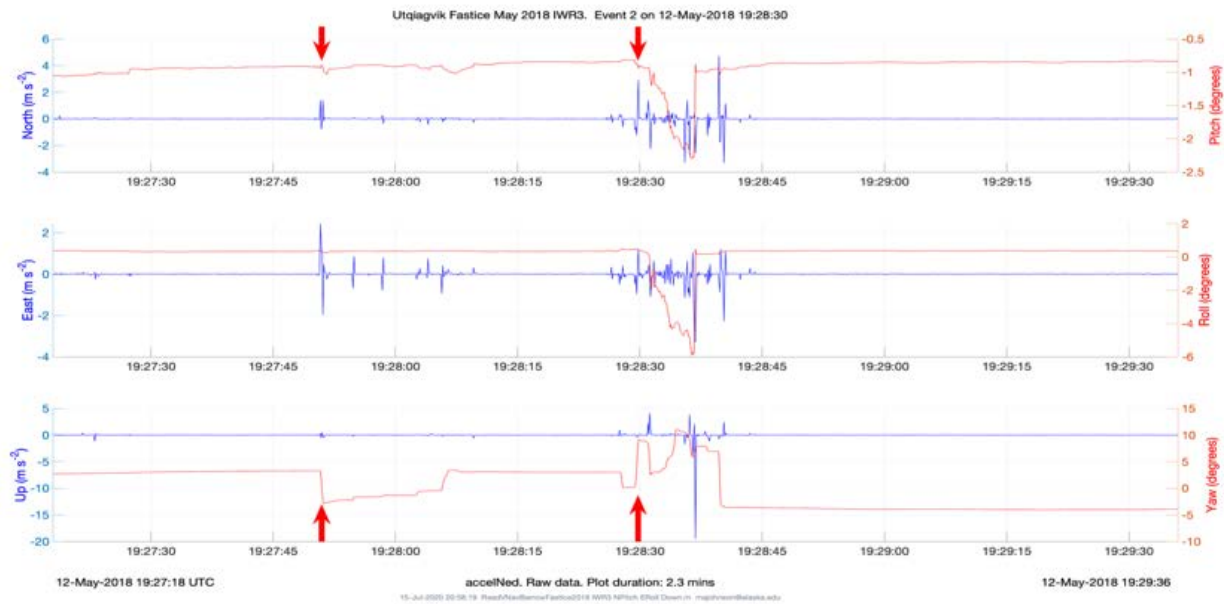
Figure 29. IWR3 Point Barrow NED accelerations (left axes) and yaw, pitch, and roll (right axes). N and E are up to 4 m s^{-2}, lasting for ~45 seconds, and the jolt in D acceleration is ~20 m s^{-2}. The jolt occurs at 19:27:50 UTC (left red arrow) as yaw changes by 8°. A series of jolts at 19:28:30 (right red arrow) occurred with a 2° pitch and 15° yaw.

In May 2020, IWRs 7, 8, 9, and 10, each with the updated filtering protocol and telemetry of Down accelerations $> \pm 1$ m s^{-2}, were deployed on Chukchi Sea landfast ice. IWR7 and IWR8 were placed west of Point Barrow (Figure 25). They show accelerations above 1 m s^{-2} beginning around 16 May. Early on 22 May, IWR8 yaw abruptly changed by ~10 degrees and began to roll and pitch by 4 degrees (Figure 30). About this time, the landfast ice was becoming unstable (Michael Thomas, UIC, personal communication). IWR7 and IWR8 were recovered from the ice on 30 May.
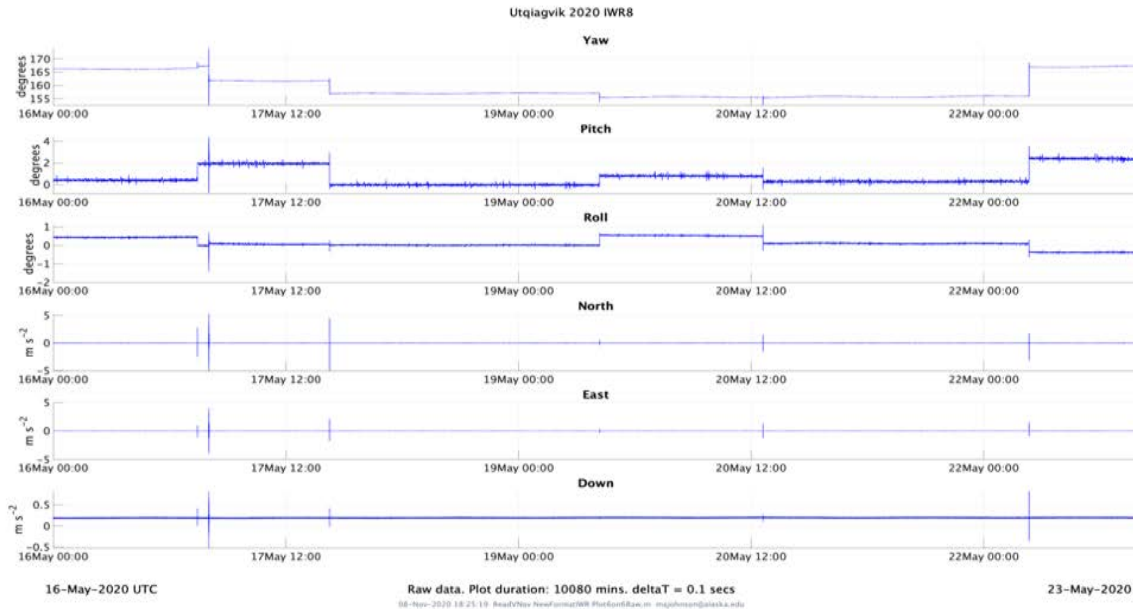
Figure 30. IWR8 Utqiaġvik 2020 jolts in NED accelerations and step changes in yaw, pitch, and roll when the ice was becoming unstable.

IWRs 9 and 10 were deployed on Chukchi Sea landfast ice west of Utqiaġvik from 20 – 29 May 2020 (Figure 31). On May 27, a 5 m s^{-2} jolt in Down acceleration in IWR9 occurred at the same time that the ice rotated (yaw) by 20° degrees and began a 2° roll (Figure 32). Deteriorating conditions prompted the recovery of IWR9 and IWR10 on 28 May.

Figure 31. IWR9 on landfast ice west of Utqiaġvik near open water of the Chukchi Sea.
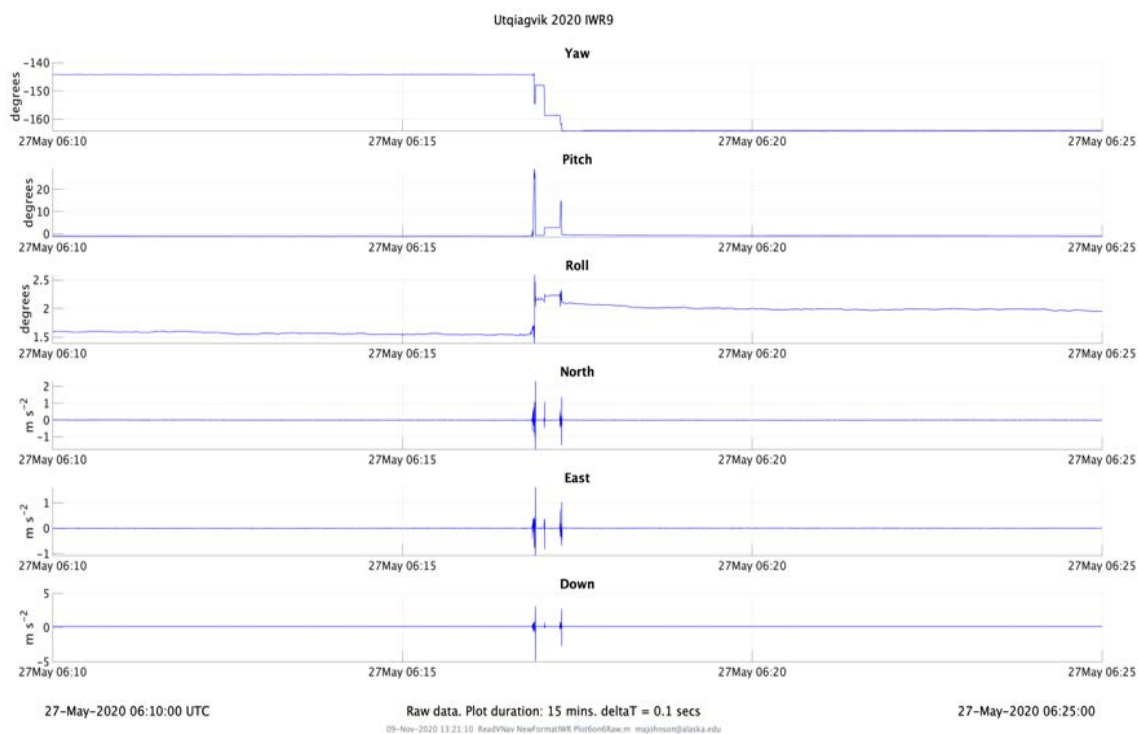
Figure 32. IWR9 Utqiaġvik 2020 with D accelerations up to 5 m s^{-2}, N and E accelerations to 2 m s^{-2} and changes of ~15° yaw of and ~30° pitch.

Breakout Event

In March 2019, Johnson and Mahoney deployed sensors IWR3 and IWR4 west of Utqiaġvik on Chukchi Sea landfast ice using the whaling trail of Kooneak Nageak. The IWRs were to be deployed 30 meters apart at the lead edge near open water; however, the lead closed the day before the planned deployment, so the sensors were placed on relatively un-deformed ice within 5 meters of the former lead edge (Figure 33). The next day we returned to the site, recovered data from both sensors, and redeployed them. On March 27, the landfast ice detached and began drifting off Point Barrow with sensor IWR4 (Figure 34). For almost 30 days, IWR4 telemetered time, position, and battery voltage until transmission ceased when the power supply fell below the 5V minimum needed to power the sensor.

Sensor IWR3 was recording data nearby when the ice with IWR4 detached. Recovered a day later, IWR3 measured extreme values of NED accelerations and abrupt changes to yaw, pitch, and roll during the "breakout" of IWR4. NED accelerations reached $\pm$10 m s^{-2}, roll reached 60°, and yaw changed by ~12° (Figure 35). With IWR4 lost, UIC re-deployed IWR3 in late April 2019 on Chukchi Sea landfast ice using the whaling trail of Frederick Brower. Figure AI.33, Appendix I, shows data from the 21-day deployment with oscillations in the N acceleration on 23 April and several jolts in NED, particularly around 30 April and 9 May. Yaw shows oscillations of 1° lasting for 6 – 12 hours at regular intervals throughout the record.

Figure 33. IWR3 (left) and IWR4 (right) deployed on Chukchi Sea landfast ice in March 2019. The ice supporting IWR4 detached on 27 March 2019 and drifted off Point Barrow for the next 30 days.
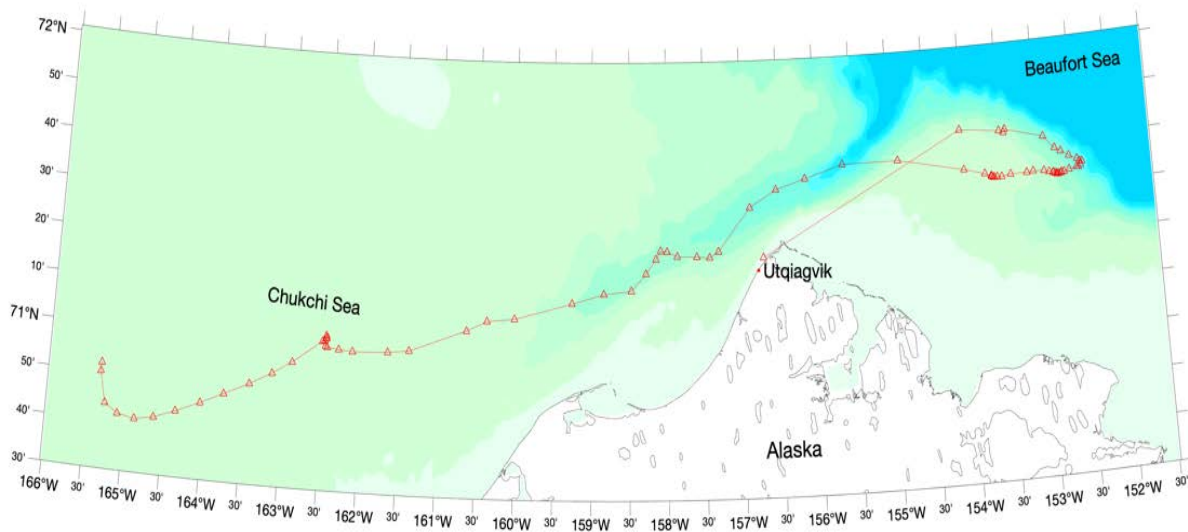
Figure 34. Drift track of IWR4 sensor following detachment on 27 March 2019. The sensor telemetered time, position, and battery voltage until 26 April, when the power fell below the minimum threshold.
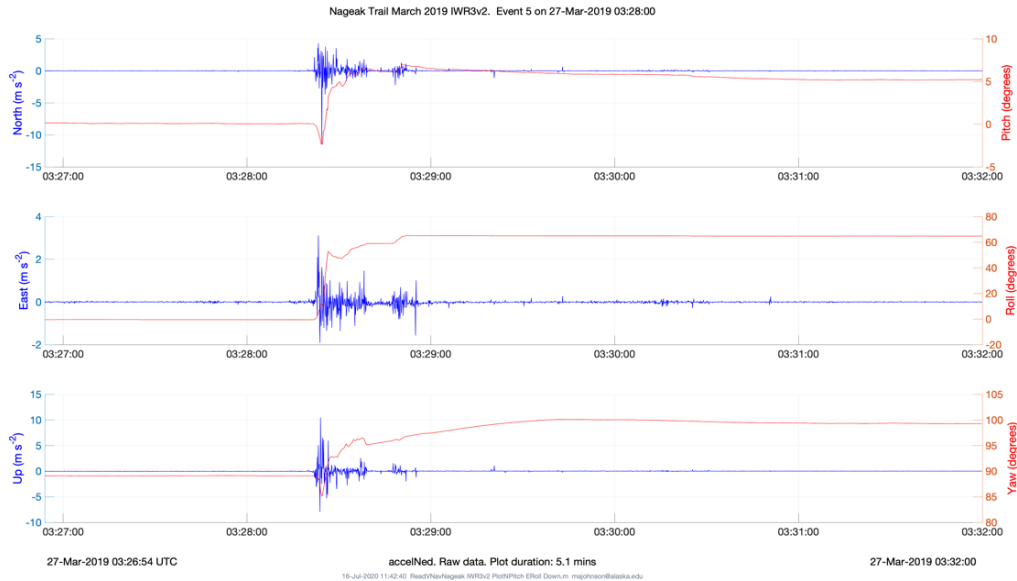
Figure 35. IWR3 Nageak Trail NED accelerations (left axes) and YPR (right axes) just prior to the breakout event. N and D accelerations exceed ± 10 m s^{-2} as roll reaches 60° and yaw changes by 12°.

Waves in Ice

The deployments in 2020 were the first to show signals associated with waves in ice. Based on our signal processing as developed so far, previous deployments showed no clear evidence of waves propagating in ice. However, it is possible that sensors deployed before 2020 missed registering wave propagation because the default VN-100 filter settings were inadequate to capture any signal. As noted in "METHODS," a 5-fold reduction in noise arises from setting the VN-100 filtering parameters to output the data at 10 Hz as a running average of the sensor's internal 800 Hz data stream. In early 2020 we dismantled IWR2 and IWR3 to reprogram the VN-100 with the new filter settings. After testing the IWRs for data consistency, we purchased six new IWRs (#5#10) with the revised filter settings and telemetry of the "z-counts." Two pairs of new sensors deployed in 2020 have processed data consistent with waves in ice: IWR5 and IWR6 deployed on drifting ice in the Beaufort Sea as part of ICEX2020, and IWR7 and IWR8 deployed on Chukchi Sea landfast ice near open water (Figure 36).

Figure 36. IWR7 (left) and IWR8 (right) on landfast ice near open water of the Chukchi Sea and north of whaling camp.

To identify wave signals, we processed the IWR data using the approach detailed in "METHODS" after Kohout et al. (2015) and described further in Rabault et al. (2016, 2020). Essentially, the vertical acceleration is double-integrated to produce timeseries of displacement, the vertical motion of the ice. Mathematically, the calculated vertical displacement is the motion required to produce the measured accelerations. For this study, we set the period parameters used to calculate displacements to between 2 and 20 seconds, a typical band for waves in ice (Kohout et al., 2015). The resulting displacement timeseries is partitioned into 30-minute lengths, with each new segment overlapping the previous one by 50%. This is commonly referred to as the Welch method (Welch, 1967) with 50% overlap. The 50% overlap acts to slightly smooth the spectra. A Fourier analysis is applied to each 30-minute timeseries, with the resulting spectral amplitudes, stacked in time over the deployment period, termed the Welch periodogram.

The processed ICEX2020 data from IWR5 and IWR6 are shown as full-record timeseries of vertical displacements in Appendix I (Figures AI.14 and AI.15) and Welch periodograms (Figures AI.16 and AI.17). Both sensors have similar responses. During wave activity (Figure 37), the displacement amplitudes are almost 2 cm, and the dominant periods are centered on ~3 – 4 seconds and ~10 – 18 seconds. There is little or no signal between these two bands, at ~5 – 8 seconds. The first wave signals persist for ~16 hours, and the second persists for ~10 hours. The higher frequency response (3 – 4 seconds) appears slightly later than the lower frequency response (10 – 18 s).
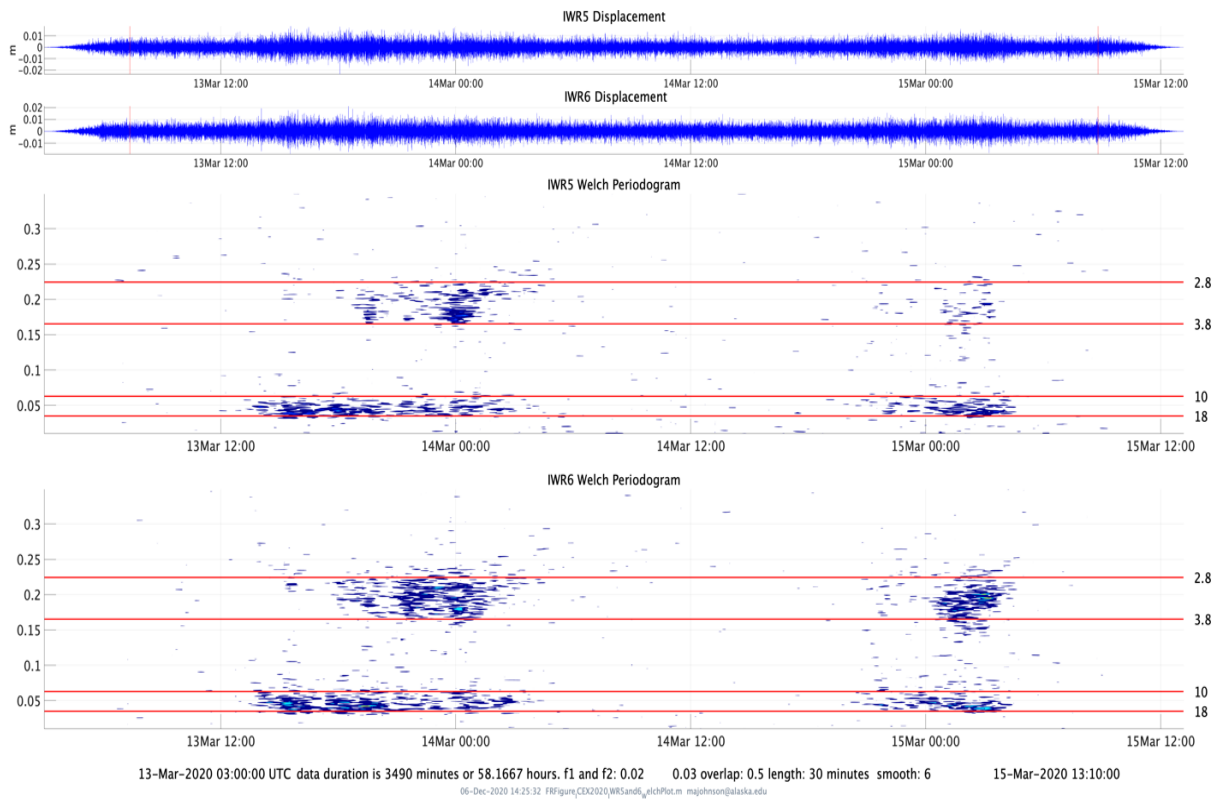
Figure 37. ICEX2020 IWR5 and IWR6 displacements (top two frames) and Welch periodograms (bottom two frames). The two sensors simultaneously measured signals with spectral peaks in the ~3 – 4 second and 10 – 18 second wave bands (period in seconds marked by red lines) lasting for ~16 hours on 13 March and for ~10 hours on 14 – 15 March.

Surface gravity waves and flexural-gravity waves in ice are forced by moving pressure fields or winds, as discussed in the "INTRODUCTION." The wind speed during the ICEX2020 campaign, recorded by meteorological sensors at the camp, is plotted from 9 to 17 March 2020 in Figure 38. On 12 May, the wind speed increased, exceeding ~22 m s^{-1} by midday on the 13th and lasting for ~16 hours. After a lull to ~10 m s^{-1}, winds again exceeded ~22 m s^{-1} late on 14 March, lasting through midday 15 March. The ice thickness at ICEX2020 ranged from ~1.2 m thick first-year ice near the runway and IWR6 to ~2.5 m thick on multiyear ice around the camp and IWR5. The thickness survey line, camp location, and runway location are shown in Figure 39.
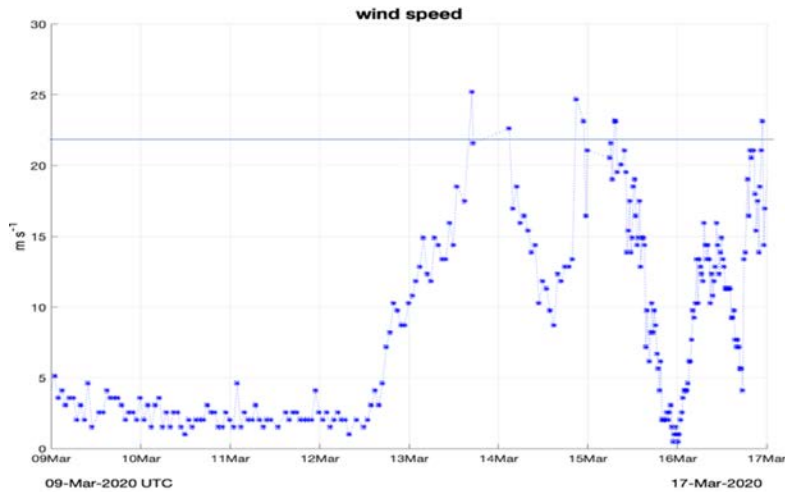
Figure 38. ICEX2020 wind speed in meters per second from 9 – 17 March. The winds reach 22 m s^{-1} near midday on 13 March.
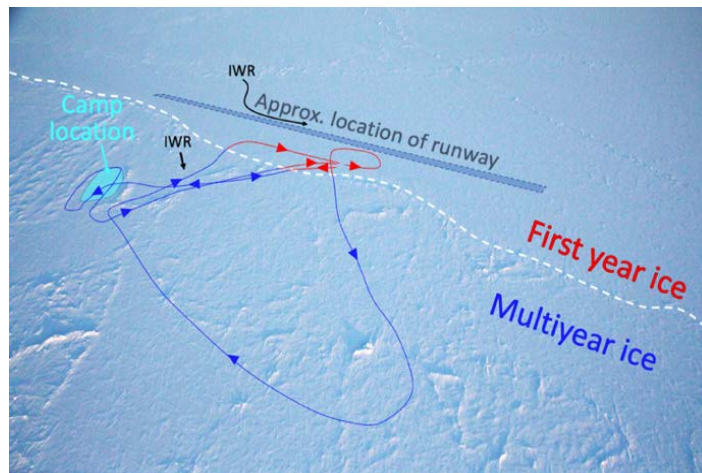
Figure 39. ICEX2020 with IWR5 on multiyear ice and IWR6 near runway on first-year ice. Ice thickness survey lines are marked in red and blue. (Figure from Chris Polashanski.)

The wind speed, ice thickness, and the dispersion relationship for flexural-gravity waves (see Equation 1) can be used to infer the response of the ice-ocean system. Figure 40 relates frequency to the phase and group velocities for 1000-meter water depth and 1.2-meter ice thickness. For wind speeds of ~22 m s^{-1}, the excited waves are expected to have frequencies between $2\pi/3$ seconds and $2\pi/14$ seconds. The group and phase speeds cross, where energy is trapped, at a period of 7.7 seconds (Figure 40). This is

generally consistent with the frequency response bands measured by the IWRs with wave energy in the bands from 2.8 – 3.8 and 10 – 18 seconds. The ICEX2020 waves were forced in a range of ice thickness by extremely strong winds over deep water. While the agreement with theory is reasonable, future work might examine the width of the resonance band. In our case, it spans from 4 to 9 seconds, wider than theory suggests.
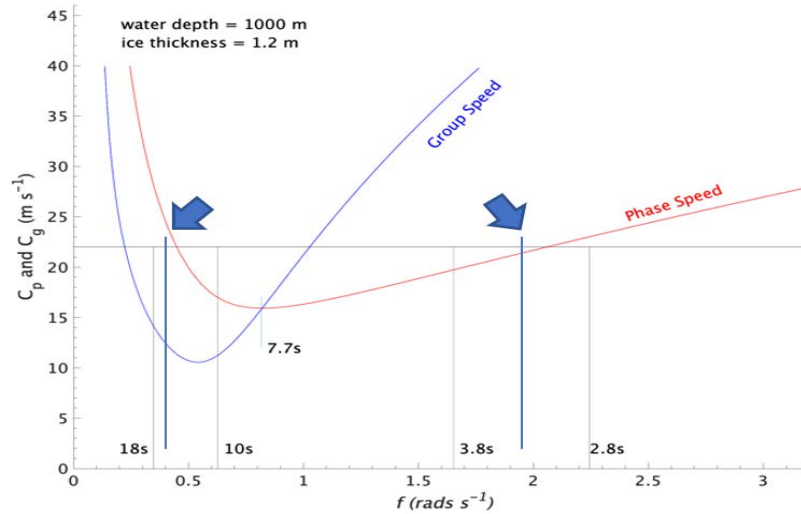
Figure 40. Frequency (Hz) versus phase and group speeds (m s^{-1}) for ice 1.2-meter thick and 1000-meter water depth. For winds of 22 m s^{-1}, the excited waves periods are between ~3 and ~14 seconds (blue arrows and lines) with a gap at 7.7 seconds where the phase equals the group speed.

The results from landfast ice near Utqiaġvik are different from ICEX2020. In May 2020, IWR7 and IWR8 were deployed about 0.44 kilometers west of Point Barrow, Alaska (Figure 25) on landfast ice where the water depth is ~55 meters. The IWRs were placed ~15 meters from the lead edge using Michael Donovan's whaling trail and collected data at 10 Hz from 1 – 30 May (Appendix I, Figures AI.22 and AI.23). MODIS imagery shows a small lead west of Utqiaġvik on 1 May when winds were blowing toward the coast. On 4 May, the winds turned offshore, opening the lead, and continued offshore from 7 – 16 May, maintaining the open lead (Figure 41). The wind speed (Barrow airport) was less than 4 m s^{-1} through May 10th and then increased to 15 m s^{-1} with gusts to almost 20 m s^{-1} on 12 – 13 May (Figure 42).
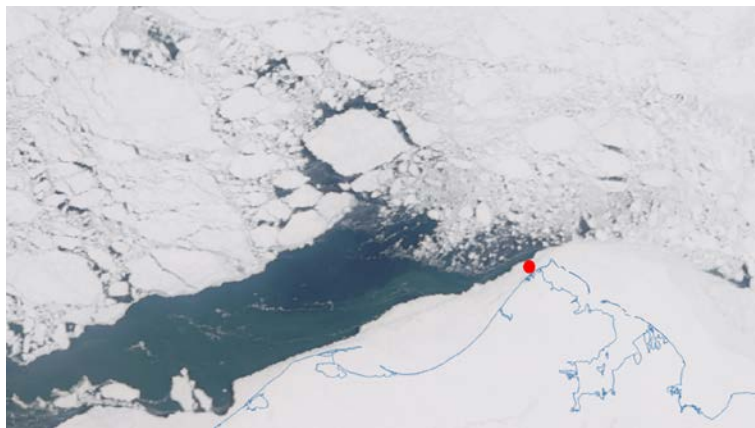
Figure 41. MODIS image on 13 May 2020 (16:37 UTC) showing open lead west of Utqiaġvik and IWR location (red dot). Figure courtesy of Lew Shapiro.
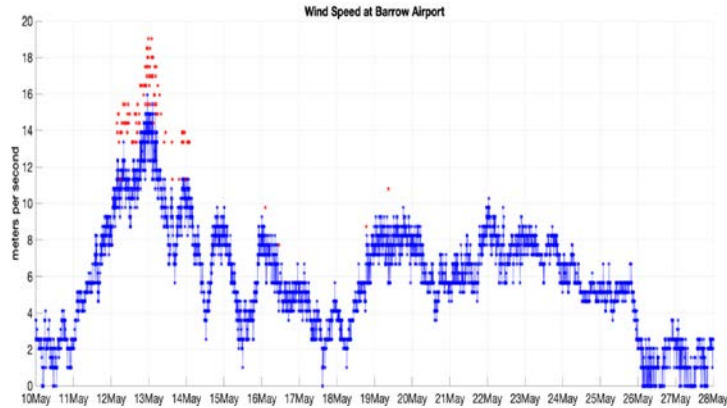
Figure 42. Wind speed (blue) and wind gusts (red) in m s^{-1} at Barrow Airport for 10 – 28 May. Speeds reach ~15 m s^{-1} on 12 May and reach a peak of 19 m s^{-1} early on 13 May 2020.

IWR7 and IWR8 Welch periodograms reveal three separate events with spectral peaks having periods in the wave band beginning early on 12 May 2020. Spectral amplitudes for periods between 3 and 7 seconds are evident from 12 May – 13 May 2020, persisting for ~36 hours. A second, weaker event at the ~3 second period lasts for several hours on 24 May. A third event from 27 – 28 May lasts about 24 hours in the 5 – 7 second band. As in the ICEX data, the higher frequencies tend to appear slightly later in the record.

The vertical displacements (Figure 43), calculated after Kohout et al. (2015) and Rabault et al. (2016; 2020), have amplitudes to ~1.5 cm. The spectral responses (Figure 43) are a single band from ~3 – 7 seconds without any gap between high and low frequencies. This contrasts the response ICEX2020, where the spectral response is bi-modal, appearing as two separate bands.

For the 55-meter depths at Utqiaġvik, Figure 44 shows the expected frequency response for 0.5 and 1-meter ice thickness for the observed wind speed of 15 m s^{-1}. If the ice was 1-meter thick, a 15 m s^{-1} wind is too slow to excite waves. However, our instruments detected waves between 2.7 and 6.7 seconds. If the ice was thinner under the IWRs, the responses measured by IWR7 and IWR8 fit wave theory. In 2020, Matt Druckenmiller (UAF) and team mapped the ice thickness along the Utqiaġvik whaling trail we used to deploy IWR7 and IWR8. The thickness was ~0.61 – 1.22 meters near the lead edge, thinner than many other locations. It is also possible that winds were stronger over the landfast ice than at the Barrow airport.
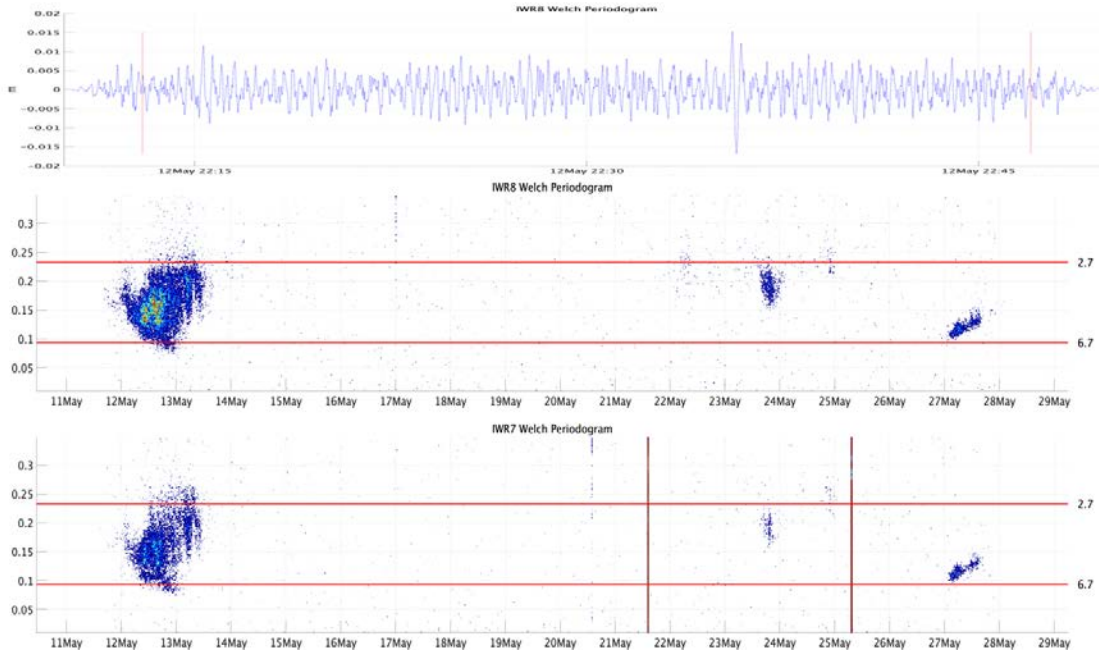
Figure 43. Utqiaġvik 2020 IWR8 displacements to ~1.5 cm (40-minute span, top), and IWR7 and IWR8 Welch Periodogram from 11 – 29 May (bottom two frames). Both sensors began measuring wave signals in the ~3 – 7 second band (period in seconds marked by red lines) on 12 May. Weaker events occur on 23 and 27 May, lasting ~8 hours and ~18 hours, respectively. The vertical lines in the IWR7 periodogram are likely due to ice-ice jolts that produce a broad spectral response.
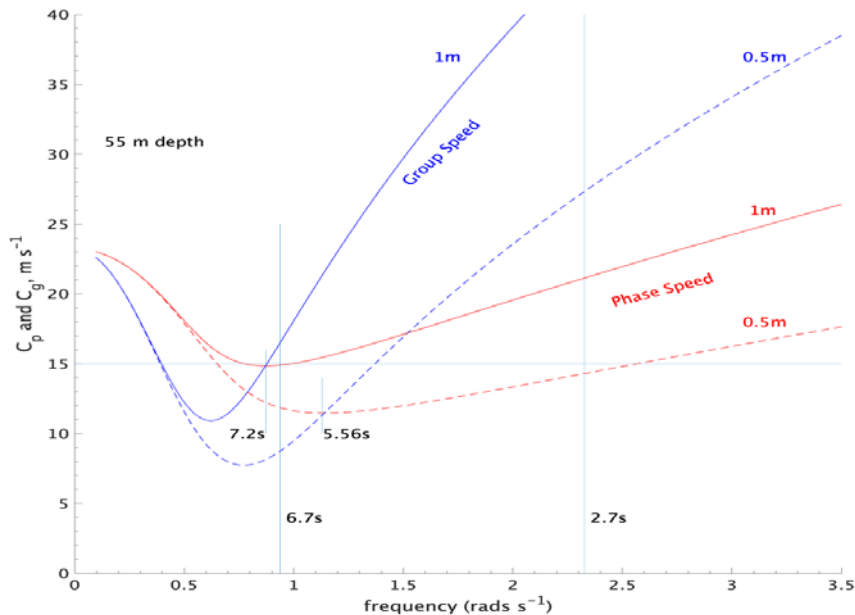
Figure 44. Wave frequency versus phase (red) and group (blue) speeds for ice thickness of 1- (solid) and 0.5- (dashed) meters. Wind speeds of 15 m s^{-1} excite waves ~7.2 seconds. For ice 0.5-meters thick, the response is a range from ~7 – 2.5 seconds. The measured range was 2.7 – 6.7 seconds.

DISCUSSION

To the best of our knowledge, the measurements described here are the first such data acquired from Chukchi Sea landfast ice using state-of-the-art accelerometers deployed in stand-alone packages. We also acquired data from drifting ice in the Beaufort Sea from the U.S. Navy's ICEX2020 Camp Seadragon. We have identified specific time spans from both regions where the theory for wave propagation in ice is consistent with the measurements.

Measurements from landfast ice west of Utqiaġvik, Alaska, and drifting ice in the Beaufort Sea reflect significantly different ice and ocean conditions. The ICEX data, from drifting ice in a nearly continuous ice cover, contrasts the quasi-stationary landfast ice west of Utqiaġvik. The ocean depth was ~1000 meters at ICEX2020 and only ~55 meters off Utqiaġvik. For both areas, the ice thickness ranged from ~0.5 meters to more than 2 meters. Given the range of conditions, our measurements are in reasonable agreement with theory. While the dispersion model is "tunable" based on input parameters, we chose reasonable values from the literature. For example, we used 3 N m^{-2} for Young's Modulus in the bending term in Equation 1; however, it has a large possible range, from $1 - 10$ N m^{-2} (personal communications, C. Polashenski, A. Marchenko) and the value will modify the dispersion curve results.

We discovered there is potential for resonance conditions to arise on landfast ice near Utqiaġvik, where wave energy can build and affect the ice stability. Resonance occurs when the wave phase and group velocities are equal to the wind speed. In this case, wave energy is unable to propagate away, and the wave amplitude grows locally. Based on the dispersion relation, we can compute the intersection where the wind, phase, and group speeds are the same. At Utqiaġvik and a water depth of 55 meters, resonance can occur when winds are ~15 m s^{-1} and ice is ~1-meter thick (Figure 45), quite similar to the conditions near the IWRs. Resonance conditions may help to weaken the ice. However, under these wind speeds, ice users would likely have left for safety ashore.

Resonance may occur at lesser wind speeds where the ice is thinner. We can generalize this relationship for wind speed and ice thickness (Figure 46). For conditions shown by the red line, the wave amplitude may grow as energy cannot propagate away. This may be a mechanism to weaken or destabilize the ice as a pre-condition for breakout events. In this case, wind speeds at 10 m s^{-1} are enough to generate resonance when the ice is 0.5 meters thick.
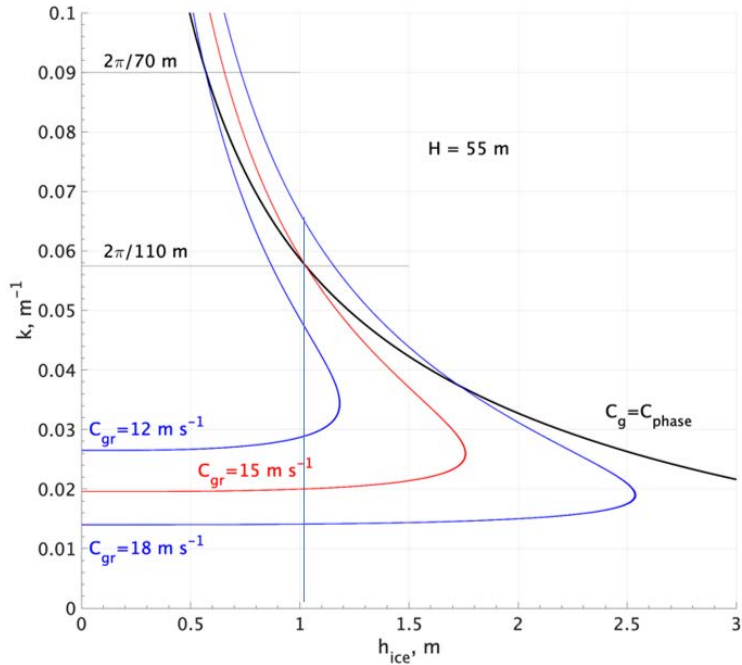
Figure 45. Ice thickness versus wavenumber for resonance conditions; black line marks equal group and phase speeds, blue and red lines mark wind speeds. Resonance occurs where the lines overlap. Here the wave energy grows because the wave energy is trapped and cannot propagate away.
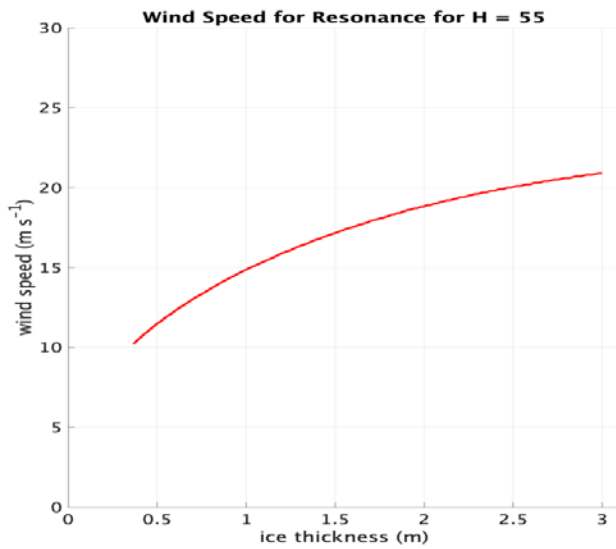
Figure 46. Ice thickness versus wind speed for resonance. Wave amplitude can grow for conditions marked by the red line.

CONCLUSIONS

Motion sensors were designed, constructed, and deployed on stable ice in Elson Lagoon, Alaska, on landfast ice of the Chukchi Sea near Utqiaġvik, Alaska, and on drifting ice in the Beaufort Sea as part of the U.S. Navy ICEX2018 and ICEX2020 ice campaigns. Deployments from 2016 through 2020 successfully measured ice motion at 10 Hz. More than 9000 hours of data were acquired during the project. The data consist of timeseries of accelerations in the North-East-Down coordinate system and the attitude headings of yaw, pitch, and roll.

Our primary sensor, the IWR, is portable, easy to carry and deploy, telemeters real-time data on ice conditions, and has the power to operate unattended for more than six weeks. Battery and data storage swap-out can be done in the field. The IWR design improved after each field season to make it smaller, lighter, and easier to deploy. The present design can telemeter from the field real-time data of measured ice motion and operate unattended under extreme conditions. A unit design using the Seaview Systems, Inc. SVS-603 sensor was deemed to have insufficient measurement sensitivity and field-reliability based on deployments on Chukchi Sea landfast ice and on the ice near Prudhoe Bay, Alaska. We discontinued the development of SVS-603 based sensors after the 2019 field season.

The data show the ice to be relatively motionless, occasionally punctuated by short bursts of large accelerations (jolts), possibly due to ice-ice collisions, and longer-lasting signals (rumbles), possibly from ice grinding or ridge formation. Convergence events due to winds or currents produced rumbles with accelerations of the order of 1 m s^{-2}. A value of 1 m s^{-2} was selected as a threshold measure of ice activity to monitor and telemeter via Iridium. Other values may be appropriate, depending on the type of ice motion to be monitored.

Jolts up to 20 m s^{-2} and rolls to 60° were measured. A jolt of 10 m s^{-2} was measured prior to a nearby detachment and breakout of ice that then drifted into the Beaufort Sea. During the observed breakout, a sensor was lost along with the data stored on-board, which presumably measured the precise accelerations and attitude headings causing the breakout. Based on our data so far, there is no definitive threshold for accelerations that lead to a breakout event.

The risk of loss or damage imposes a financial constraint on sensor production costs and underscores the importance of data telemetry. The cost of data telemetry is proportional to the quantity of data transmitted through the Iridium network. One of our sensor designs demonstrated wireless data transfer using the XBee radio system, which, after scale-up, could be used in remote locations to transmit large data sets to a base station and the internet for stakeholder access. It was tested at sampling rates up to 40 Hz. Using XBee to transmit data to a base station could reduce Iridium telemetry costs and be particularly important for large deployments. In laboratory exercises, we demonstrated how such a system might work and feed the internet for real-time data display and event triggering. A scaled-up XBee network has the potential to be able to transmit large data sets from the field for real-time monitoring and event-triggering.

Mobile ice chiseling into landfast ice causing it to weaken or detach, winds or edge waves driving sea level changes that destabilize ice grounding points, and waves weakening ice through repeated flexing or resonance, all appear to be possible precursors to breakout events along the Chukchi Sea coast. Evaluating their role in creating breakout conditions requires measurements from locations where the ice is or may become unstable. Our present inability to predict when and where the ice may become unstable poses a direct challenge to developing a simple and safe strategy for deploying sensors for on-ice

measurements. Nevertheless, we met a key goal of this research by acquiring measurements of ice motion that identified the types of signals that could be used to alert stakeholders about unsafe ice.

By the 2020 field season, the IWRs had improved the VN-100 on-board data filtering and were consistently being deployed close to open water of the Chukchi Sea. We were able to measure waves in ice based on the agreement between the measurements and the wave dispersion relationship for flexural-gravity waves. Flexural-gravity waves are waves propagating under an ice cover and having periods and wavelengths described by the dispersion relationship in Equation (1) in the "INTRODUCTION." This dispersion relationship arises by treating the ice cover as a thin elastic plate. It applies to IWR measurements of waves in ice acquired during ICEX2020 at U.S. Navy's Camp Seadragon on drifting ice and measurements acquired on landfast ice at Utqiaġvik. We were able to acquire measurements consistent with waves in ice from two separate deployments, with each deployment using a pair of sensors. The measured waves have periods ranging from ~2 to ~18 seconds, typical periods for waves in ice.

The ICEX2020 and Chukchi Sea landfast ice data are highly complementary, allowing us to look at the wave response for water depths of 55 and 1000 meters, ice thickness from 0.5 – 2.5 meters thick, and for a range of wind speeds up to 22 m s^{-1}. An emerging hypothesis from this work suggests there is potential for resonance conditions to arise that trap wave energy in the region, allowing the wave amplitude to grow. Rapidly growing wave amplitudes may play a role in weakening or destabilizing the ice, adding to the list of potential mechanisms that drive ice breakout.

Future work may be motivated by the following questions: Was the VN-100 sensor measuring ice motion responding to the diurnal cycle of temperature, or are certain measurements an artifact related to the sensor's ambient temperature? For Chukchi Sea landfast ice, weaker signals in the wave band exist when the winds (measured at the Barrow Airport) appear too weak to be a forcing mechanism. Are those measured waves the result of a distant storm? Can we identify the location of such storms from those data? Further work is needed to address the differences in propagation and attenuation of ocean waves into and across the sharp boundary of landfast ice edge. Finally, although these measurements provide some insight into the magnitude of accelerations resulting from ice-ice collisions, there is still no clear threshold value associated with creating a breakout event. Further work is needed in this dynamic environment.

STUDY PRODUCTS

Publications

Johnson, M., A. Mahoney, A. Sybrandy, and G. Montgomery (2020) Measuring acceleration and short-lived motion in landfast sea-ice. Journal of Ocean Technology, 15(3):113–131. https://www.thejot.net/article-preview/?show_article_preview=1190

Johnson, M., A. Marchenko, O. Dammann, and A. Mahoney. Flexural-gravity waves under a drifting ice cover in the Beaufort Sea during ICEX2020. Journal of Marine Science and Engineering, Special Issue, in preparation.

Presentations

"Measuring ice motion along Alaska's coast," Dr. Mark Johnson; hosted by Dr. Atle Jensen University of Oslo, Mathematics and Engineering Department, Seminar, 6 September 2019.

"Measuring ice motion along Alaska's coast," Dr. Mark Johnson; hosted by Dr. Henrik Kalisch, University of Bergen, Department of Mathematics, Seminar, 12 September 2019.

"Recent data from landfast ice off Northern Alaska," Dr. Mark Johnson; hosted by Dr. Aleksey Marchenko, University Centre at Svalbard (UNIS) and presented at the international meeting "Safety of Industrial Development and Transportation Routes in the Arctic," Memorial University of Newfoundland, Seminar, 9 October 2019.

"Forces of landfast ice breakout along Alaska's coast," Dr. Mark Johnson, Alaska Marine Science Symposium, Anchorage, Alaska. Poster presentation, January 2020.

"Forces of landfast ice breakout along Alaska's coast," Dr. Mark Johnson, Alaska Marine Science Symposium, Anchorage, Alaska. Poster presentation, January 2019.

"Measuring wave forces along Alaska's coast," Dr. Mark Johnson, CMI Annual Research Review. Zoom Conference, Oral presentation, January 2021.

"Measuring wave forces along Alaska's coast," Dr. Mark Johnson, CMI Annual Research Review, Anchorage, Alaska. Oral presentations, January 2020, 2019, 2018, 2017.

REFERENCES

Ardhuin, F., P. Sutherland, M. Doble, and P. Wadhams (2016) Ocean waves across the Arctic: Attenuation due to dissipation dominates over scattering for periods longer than 19 s. Geophys. Res. Lett., 43:5775–5783. doi:10.1002/2016GL068204

Balmforth, N. J., and R. V. Craster (1999) Ocean waves and ice sheets. J. Fluid Mech., 395:89–124. doi:10.1017/S0022112099005145

Bates, H. F., and L. Shapiro (1989) Long-Period Gravity Waves in Ice-Covered Seas. J. Geophys. Res., 85:1095–1100.

Bjørgo, E., O. M. Johannessen, and M. W. Miles (1997) Analysis of merged SMMR-SSMI time series of Arctic and Antarctic sea ice parameters 1978-1995. Geophys. Res. Lett., 24(4):413–416.

Comiso, J. (2002) A rapidly declining perennial sea ice cover in the Arctic. Geophys. Res. Lett., 29(20):17-1–17-4. doi:10.1029/2002GL015650

Danielson, S., T. Weingartner, K. Hedstrom, K. Aagaard, R. Woodgate, E. Curchitser, and P. Stabino (2014) Coupled wind-forced controls of the Bering-Chukchi shelf circulation and the Bering Strait throughflow: Ekman transport, continental shelf waves, and variations of the Pacific-Arctic sea surface height gradient. Prog. Oceanogr., 125:40–61. doi.org/10.1016/j.pocean.2014.04.006

Doble, M (2004) Sea ice physics: ice thickness determination using flexural gravity waves. Ber. Polar Meeresforsch./Rep. Pol. Mar. Res., 481:43–46.

Doble, M. J., D. J. L. Mercer, D. T. Meldrum, and O. C. Peppe (2006) Wave measurements on sea ice: developments in instrumentation. Ann. Glaciol., 44:108–112.

Druckenmiller, M. L., H. Eicken, J. C. George, and L. Brower (2012) Trails to the whale: reflections of change and choice on an Iñupiat icescape at Barrow, Alaska. Polar Geogr., 36(1–2):5–29. doi:10.1080/1088937X.2012.724459

Druckenmiller, M. L., H. Eicken, M. A. Johnson, D. J. Pringle, and C. C. Williams (2009) Towards an integrated coastal sea-ice observatory: System components and a case study at Barrow, Alaska. Cold Reg. Sci. Technol., 56:61–72.

Dumont, D., A. Kohout, and L. Bertino (2011) A wave-based model for the marginal ice zone including a floe breaking parameterization. J. Geophys. Res., 116:C04001. doi:10.1029/2010JC006682

Francis, J. A., and S. J. Vavrus (2012) Evidence linking Arctic amplification to extreme weather in mid-latitudes. Geophys. Res. Lett., 39:L06801. doi:10.1029/2012GL051000

Gearheard, S., W. Matumeak, I. Angutikjuaq, J. Maslanik, H. P. Huntington, J. Leavitt, D. Matumeak Kagak, G. Tigullaraq, and R. G. Barry (2006) 'It's not that simple': a collaborative comparison of sea ice environments, their uses, observed changes, and adaptations in Barrow, Alaska, USA, and Clyde River, Nunavut, Canada. Ambio, 35:203–211.

George, J. C., J. Zeh, R. Suydam, and C. Clark (2004a) Abundance and population trend [1978-2001] of western Arctic bowhead whales surveyed near Barrow, Alaska. Mar. Mamm. Sci., 20:755–757.

George J. C., H. P. Huntington, K. Brewster, H. Eicken, D. W. Norton, and R. Glenn (2004b) Observations onshore fast ice failures in Arctic Alaska and the responses of the Inupiat hunting community. Arctic 57(4):363–374.

Greenhill, A. G. (1886) Wave motion in hydrodynamics. Am. J. Math., 9(1):62–96. https://doi.org/10.2307/2369499

Hanafin, J., Y. Quilfen, F. Ardhuin, J. Sienkiewicz, P. Queffeulou, M. Obrebski, Bertrand Chapron, N. Reul, F. Collard, D. Corman, E. B. de Azevedo, D. Vandemark, and E. Stutzmann (2012) Phenomenal sea states and swell from a North Atlantic Storm in February 2011: A comprehensive analysis. Bull. Am. Meterol. Soc., 93(12):1825–1832.

Hunkins, K. (1962) Waves on the Arctic Ocean. J. Geophys. Res., 67(6):2477–2489.

Johnson, M., and H. Eicken (2016) Estimating Arctic sea-ice freeze-up and break-up from the satellite record: A comparison of different approaches in the Chukchi and Beaufort Seas. Elem: Sci. Anthrop. 4:000124. doi:10.12952/journal.elementa.000124

Jones, J., H. Eicken, A. Mahoney, M. V. Rohith, C. Kambhamettu, Y. Fukamachi, K. Ohshima, and J. C. George (2016) Landfast sea ice breakouts: Stabilizing ice features, oceanic and atmospheric forcing at Barrow, Alaska. Cont. Shelf. Res., 126:50–63.

Kohout, A., B. Penrose, S. Penrose, and M. Williams (2015) A device for measuring wave-induce motion of ice floes in the Antarctic marginal ice zone. Ann. Glaciol., doi:10.3189/2015AoG69A600

Langhorne, P., V. Squire, C. Fox, and G. Haskell (2001) Lifetime estimation for land-fast ice sheet subjected to ocean swell. Ann. Glaciol., 33:333–338.

Liu, A. K., and E. Mollo-Christensen (1988) Wave propagation in a solid ice pack. J. Phys. Oceanogr., 18:1702–1712. doi:10.1175/1520–0485

Mahoney, A., H. Eicken, A. G. Gaylord and L. Shapiro (2007) Alaska landfast sea ice: Links with bathymetry and atmospheric circulation. J. Geophys. Res., 112:C02001.

Mahoney, A. R., D. O. Dammann, F. J. Meyer, H. Eicken, J. Jones, and M. A. Johnson (2017) Monitoring small-scale sea ice motion with land-based and space-based radar. Proceedings of the 32nd International Symposium on Okhotsk Sea & Polar Oceans, V32:149-152. Mombetsu, Japan.

Mahoney, A. R., D. O. Dammann, M. A. Johnson, H. Eicken, and F. J. Meyer (2016) Measurement and imaging of infragravity waves in sea ice using InSAR. Geophys. Res. Lett., 43:6383–6392.

Mahoney, A., Eicken, H., and L. Shapiro (2007) How fast is landfast sea ice? A study of the attachment and detachment of nearshore ice at Barrow, Alaska. Cold Reg. Sci. Technol., 47:233–255. doi:10.1016/J.Coldregions.2006.09.005

Marchenko, A., A. Makshtas, and L. Shapiro (2002) On the excitation of shelf-edge waves due to self-induced oscillations of ice floes; *in* Ice in the Environment: Proceedings of the 16th IAHR International Symposium on Ice; 2–6 December 2002, Dunedin, New Zealand. International Association of Hydraulic Engineering and Research V2:301–309.

Norton, D. W., and A. Graves Gaylord (2004) Drift velocities of ice floes in Alaska's northern Chukchi Sea flaw zone: Determinants of success by spring subsistence whalers in 2000 and 2001. Arctic, 57(4):347–362.

Parkinson, C., D. Cavalieri, P. Gloersen, H. Zwally, and J. Comiso (1999) Arctic sea ice extensors, areas, and trends, 1978–1996. J. Geophys. Res., 104(C9):20,837–20,856.

Rabault, J, G. Sutherland, O. Gundersen, A. Jensen, A. Marchenko, and Ø. Breivik (2020) An open-source, versatile, affordable waves in ice instrument for scientific measurements in the Polar Regions. Cold Reg. Sci.Technol., 170:102955. doi.org/10.1016/j.coldregions.2019.102955

Rabault, J., G. Sutherland, B. Ward, K. Christensen, T. Halsne, and A. Jensen (2016) Measurements of waves in landfast ice using inertial motion units. IEEE Trans. Geosci. Remote Sens., 54(11):1–10.

Robin, G. (1963) Wave propagation through fields of pack ice. Phil. Trans. Royal Soc. A, 255(1057). doi.org/10.1098/rsta.1963.0006

Rothrock D, Y. Yu, and G. Maykut (1999) Thinning of the Arctic sea-ice cover. Geophys. Res. Lett., 26: 3469–3472. doi:10.1029/1999GL010863

Shapiro, L. H. 1987. Mechanical properties of sea ice and sea ice deformation in the nearshore zone. Minerals Management Service OCS Study MMS 90-0096, OCSEAP Final Report 72:357–584.

Shapiro, L., and R. Metzner (1987) Coefficients of friction of sea ice on beach gravel; pp. 520–527 *in* L Shapiro, L., Barnes, P., Hanson, A., Hoskins, E., Johnson, J., and Metzner, R. (Eds.), Mechanical Properties of Sea Ice Deformation in the Near Shore Zone; OCSEAP Final Report, Research Unit 265, Minerals Management Service, Alaska.

Squire, V. A. (1978) An investigation into the use of strain rosettes for the measurement of propagating cyclic strains. J. Glaciol., 20(83):425–431.

Squire, V. A. (2007) Of ocean waves and sea ice revisited. 2007. Cold Reg. Sci. Technol., 49:110–133.

Squire, V. A., and A. J. Allan (1980) Propagation of flexural gravity waves in sea ice; pp. 327–338 *in* Pritchard, R. S. (Ed.), Sea Ice Processes and Models, Proceedings of the Arctic Ice Dynamics Joint Experiment; Unversity of Washington Press, Seattle, WA.

Squire, V. A., and C. Fox (1992) On ice-coupled waves: A comparison of data and theory; pp. 269–280 *in* T. K. S. Murthy, W. M. Sackinger, W. M., and Wadhams, P. (Eds.), Advances in Ice Technology, Proceedings 3rd International Conference on Ice Technology, 11–13 August 1992, Cambridge, MA.

Squire, V. A., J. P. Dugan, P. Wadhams, P. J. Rottier, and A. K. Liu (1995) Of ocean waves and sea-ice. Ann. Rev. Fluid Mech., 27:115–168.

Sutherland, G., and J. Rabault (2016) Observations of wave dispersion and attenuation in landfast ice. J. Geophys. Res.: Oceans, 121(3):1984–1997. doi:10.1002/ 2015JC011446

Thomson, J., and W. E. Rogers (2014) Swell and sea in the emerging Arctic Ocean. Geophys. Res. Lett., 41:3136–3140. doi:10.1002/2014GL059983

Wadhams, P. (1973) Attenuation of swell by sea ice, J. Geophys. Res., 78(18):3552–3563. doi:10.1029/JC078i018p03552

Wadhams, P., and N. R. Davis (2000) Further evidence of ice thinning in the Arctic Ocean. Geophys. Res. Lett., 27(24):3973–3975. doi:10.1029/ 2000GL011802

Wadhams, P., and M. J. Doble (2009) Sea ice thickness measurement using episodic infragravity waves from distant storms. Cold Reg. Sci.Technol., 56(2–3):98–101. doi:10.1016/j.coldregions.2008.12.002

Wang, R, and H. H. Shen (2010) Gravity waves propagating into an ice-covered ocean: A viscoelastic model. J. Geophys. Res. C: Oceans, 115:C006024. doi.org/10.1029/2009JC005591

Welch, P. D. (1967) The use of fast Fourier transform for the estimation of power spectra: A method based on time averaging over short, modified periodograms; *in* IEEE Trans. Audio Electroacoust.,15(2):70–73. doi:10.1109/TAU.1967.1161901

Williams, T., L. Bennetts, V. Squire, D. Dumont, and L. Bertino (2013) Wave-ice interactions in the marginal ice zone. Part 2: Numerical implementation and sensitivity studies along 1D transects of the ocean surface. Ocean Modell., 71:92–101.

APPENDIX I

List of Figures

Figure AI.1. Seismic Vault December 2017 – January 2018, IWR1. From top to bottom: Air temperature (°C) and air pressure (kPa), yaw, pitch, and roll (degrees), and accelerations with positive North, East, and Down (m s^{-2}).

Figure AI.2. Seismic Vault December 2017 – January 2018, IWR2. From top to bottom: Air temperature (°C) and air pressure (kPa), yaw, pitch, and roll (degrees), and accelerations with positive North, East, and Down (m s^{-2}).

50
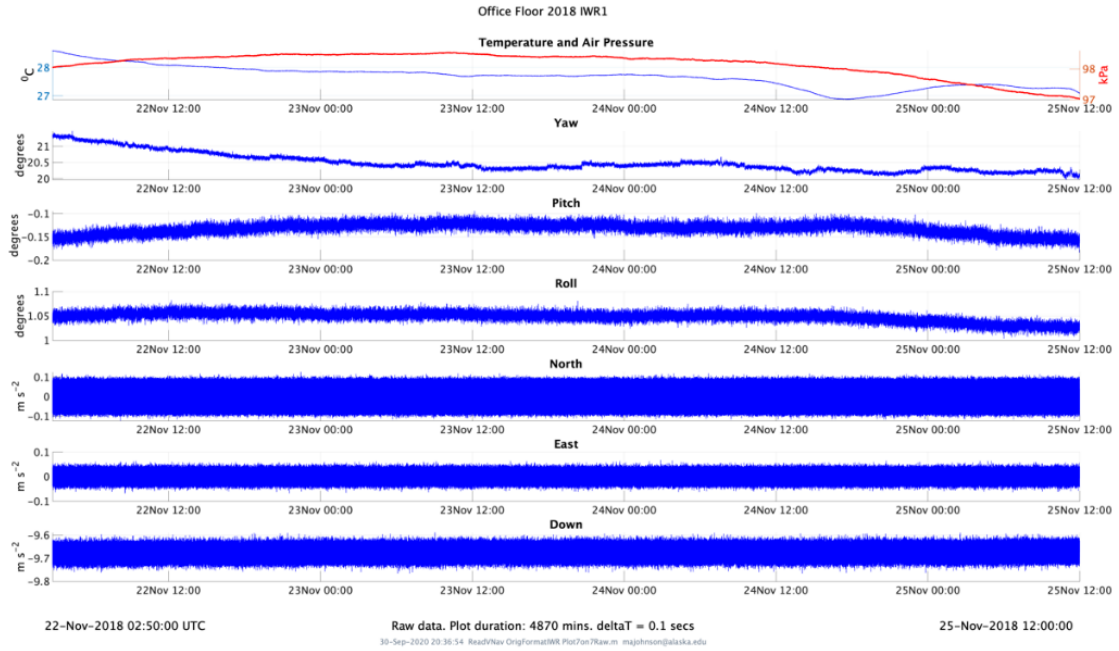
Figure AI.3. Office Floor November 2018, IWR1. From top to bottom: Air temperature ($°C$) and air pressure (kPa), yaw, pitch, and roll (degrees), and accelerations with positive North, East, and Down (m s^{-2}).
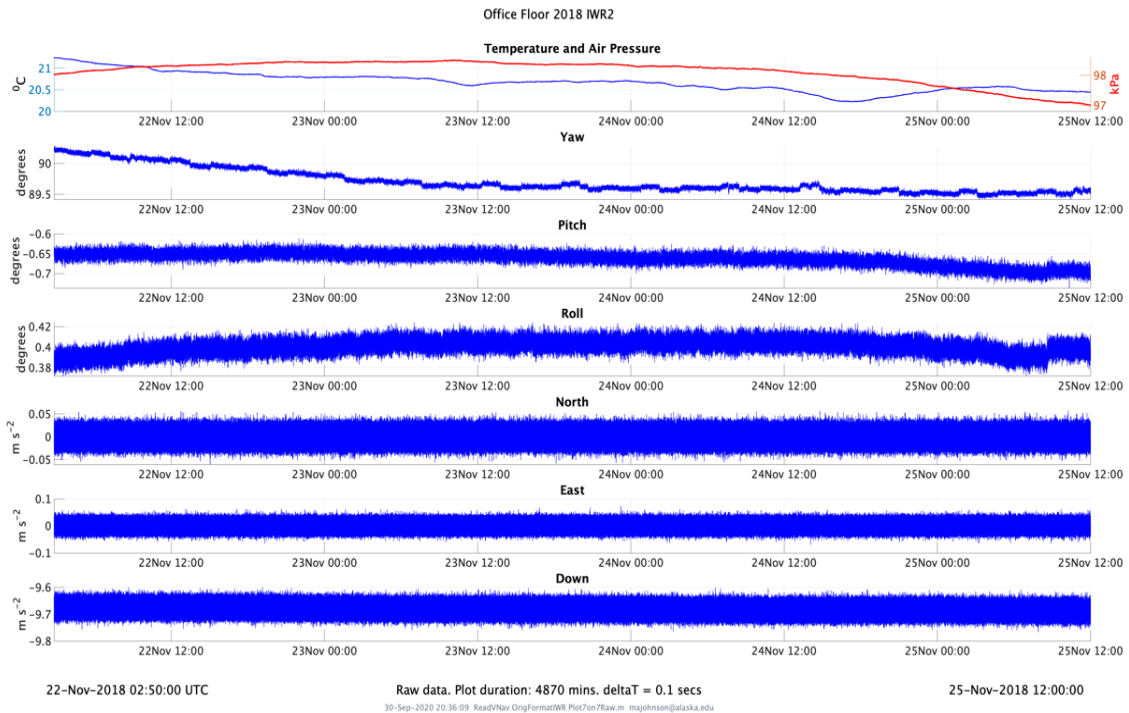
Figure AI.4. Office Floor November 2018, IWR2. From top to bottom: Air temperature ($°C$) and air pressure (kPa), yaw, pitch, and roll (degrees), and accelerations with positive North, East, and Down (m s^{-2}).
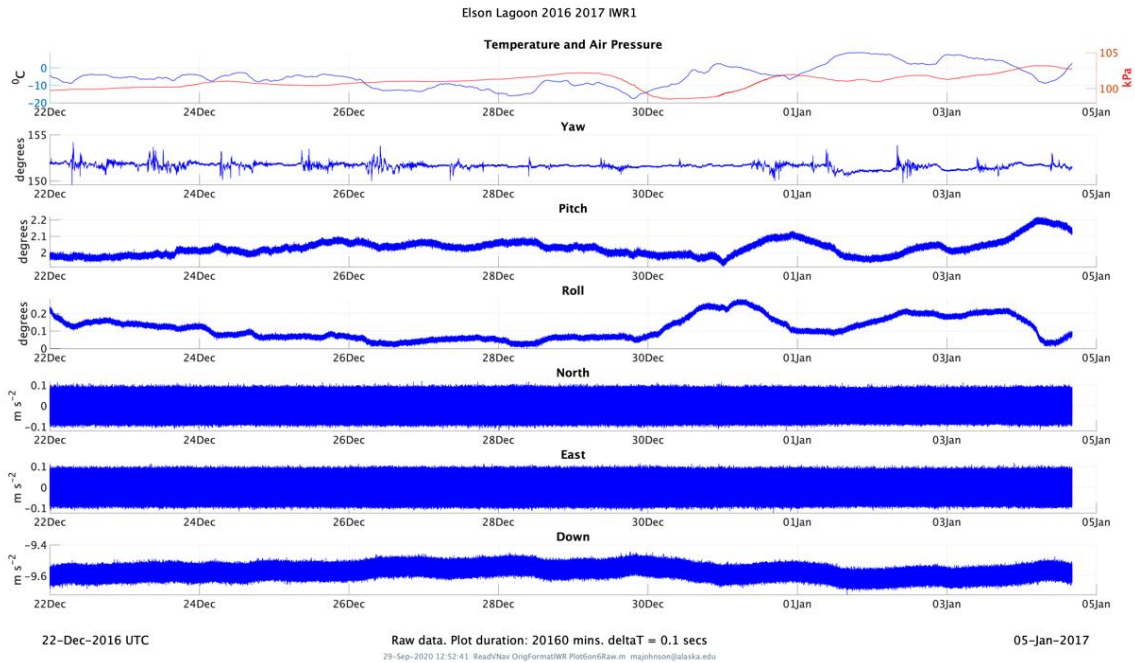
Figure AI.5. Elson Lagoon December 2016 – January 2017, IWR1. From top to bottom: Air temperature (°C) and air pressure (kPa), yaw, pitch, and roll (degrees), and accelerations with positive North, East, and Down (m s⁻²).
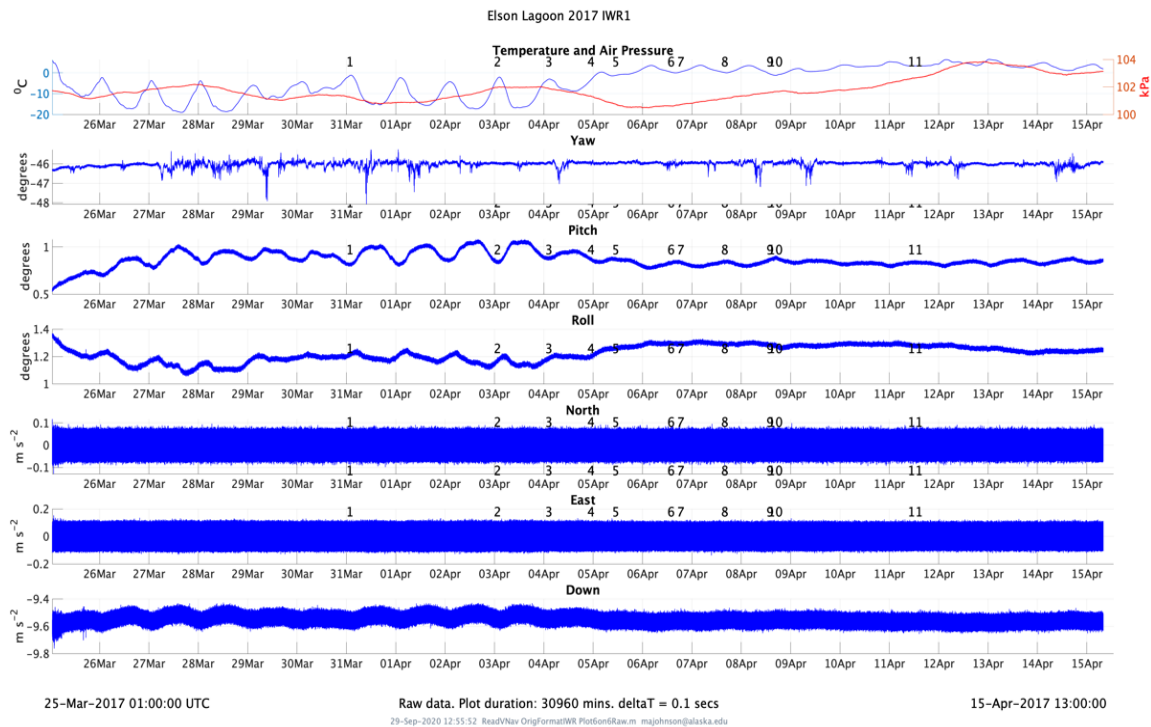
Figure AI.6. Elson Lagoon March – April 2017, IWR1. From top to bottom: Air temperature (°C) and air pressure (kPa), yaw, pitch, and roll (degrees), and accelerations with positive North, East, and Down (m s⁻²).
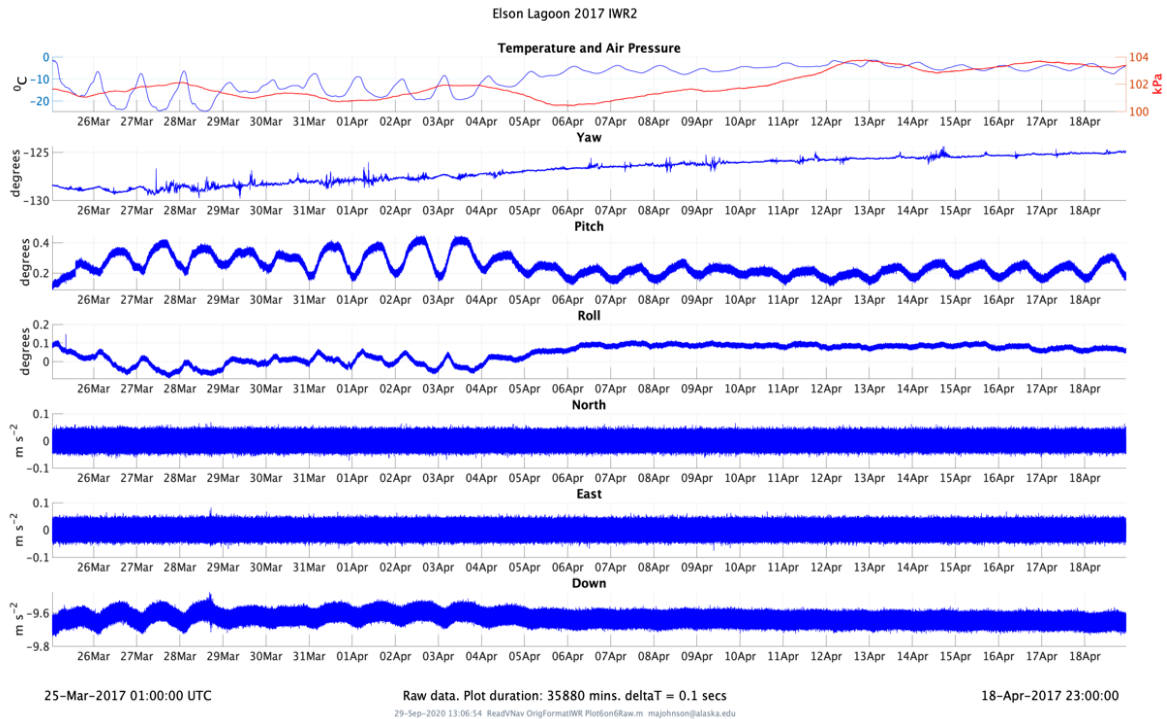
Figure AI.7. Elson Lagoon March – April 2017, IWR2. From top to bottom: Air temperature ($°C$) and air pressure (kPa), yaw, pitch, and roll (degrees), and accelerations with positive North, East, and Down (m s^{-2}).
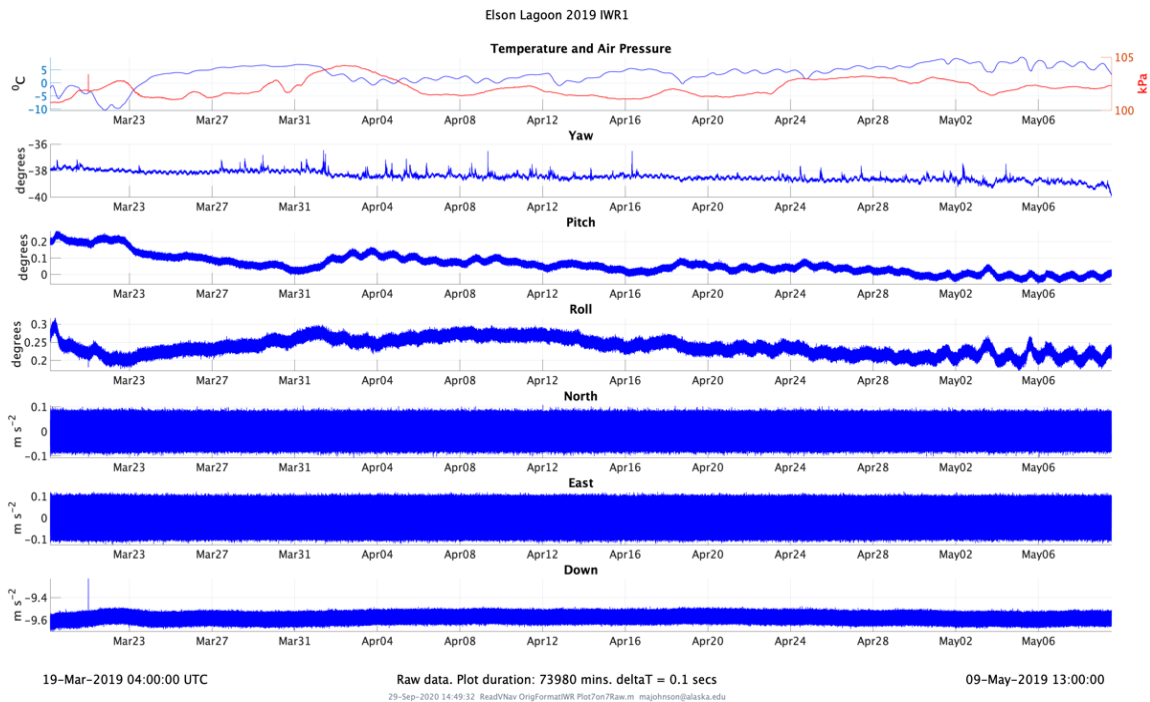
Figure AI.8. Elson Lagoon March – April 2019, IWR1. From top to bottom: Air temperature ($°C$) and air pressure (kPa), yaw, pitch, and roll (degrees), and accelerations with positive North, East, and Down (m s^{-2}).

53
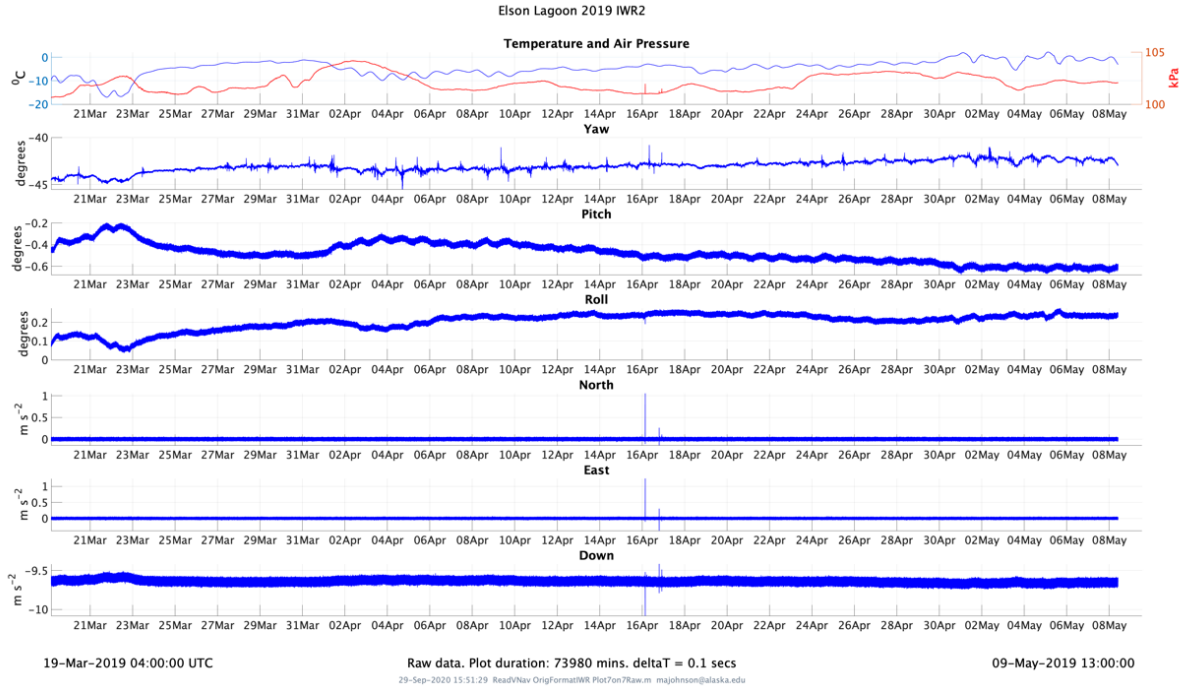
Figure AI.9. Elson Lagoon March – April 2019, IWR2. From top to bottom: Air temperature ($°C$) and air pressure (kPa), yaw, pitch, and roll (degrees), and accelerations with positive North, East, and Down (m s^{-2}).
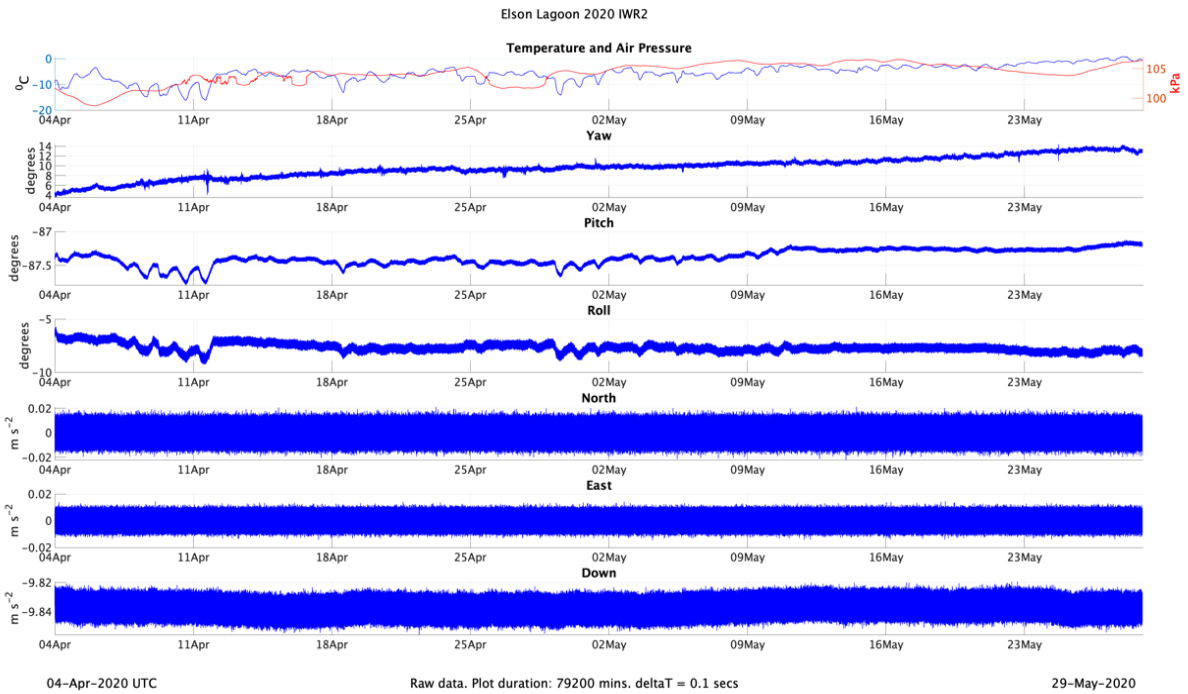
Figure AI.10. Elson Lagoon April – May 2020, IWR2. From top to bottom: Air temperature ($°C$) and air pressure (kPa), yaw, pitch, and roll (degrees), and accelerations with positive North, East, and Down (m s^{-2}).
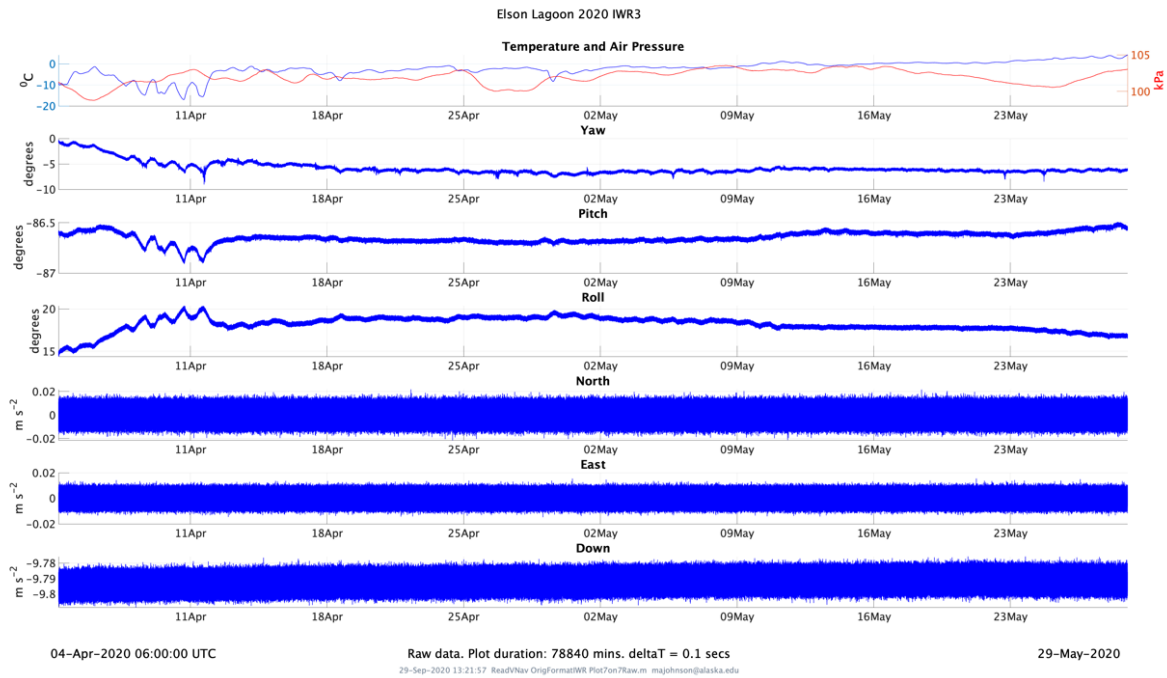
Figure AI.11. Elson Lagoon April – May 2020, IWR3. From top to bottom: Air temperature (°C) and air pressure (kPa), yaw, pitch, and roll (degrees), and accelerations with positive North, East, and Down (m s^{-2}).
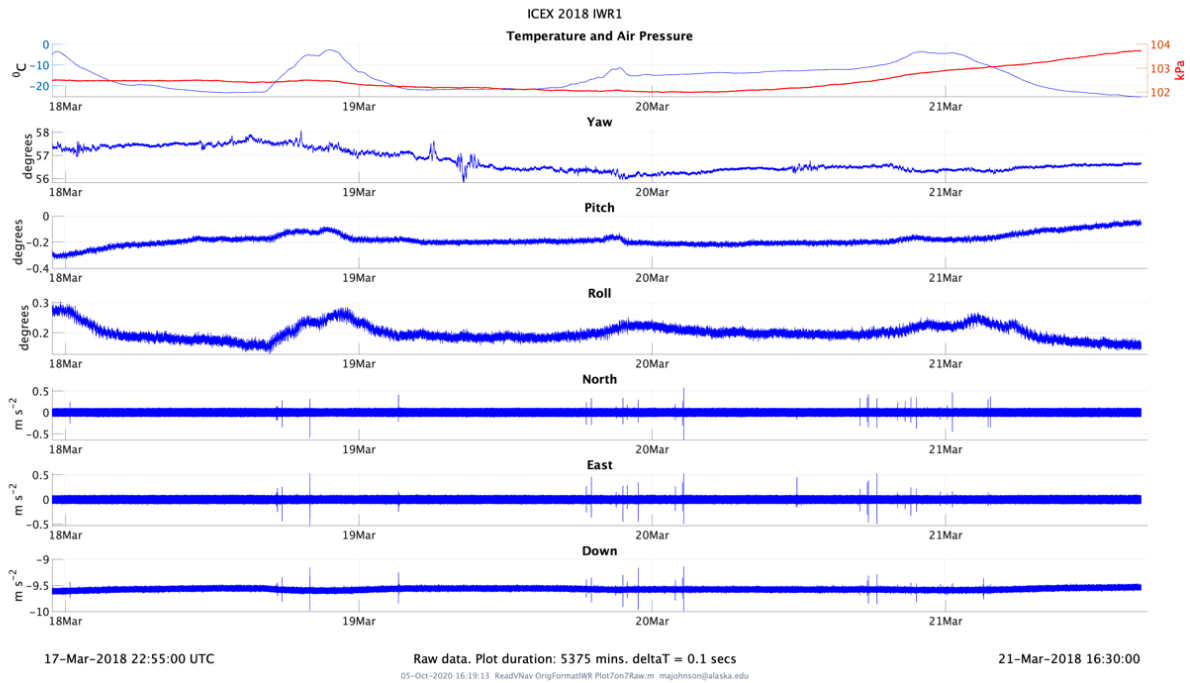
Figure AI.12. ICEX2018 April – May, IWR1 (placed 60 m from the airstrip). From top to bottom: Air temperature (°C) and air pressure (kPa), yaw, pitch, and roll (degrees), and accelerations with positive North, East, and Down (m s^{-2}). The "spikes" in NED acceleration generally align with logged times for aircraft landings.
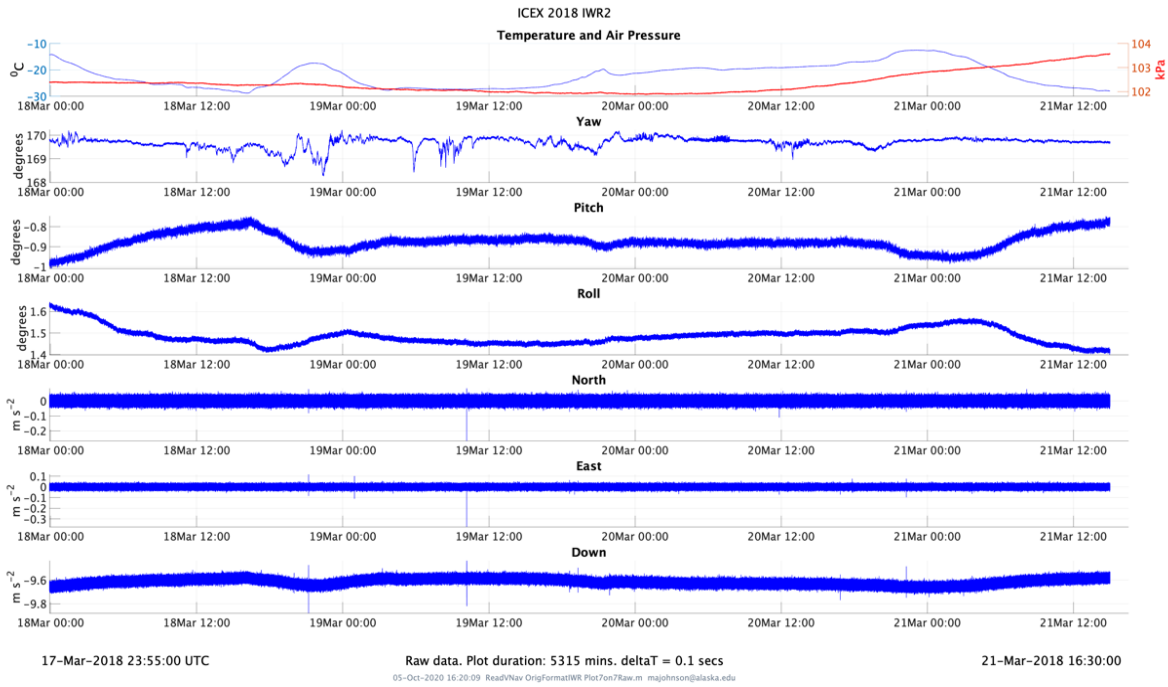
Figure AI.13. ICEX2018 April – May, IWR2. From top to bottom: Air temperature ($°C$) and air pressure (kPa), yaw, pitch, and roll (degrees), and accelerations with positive North, East, and Down (m s^{-2}).
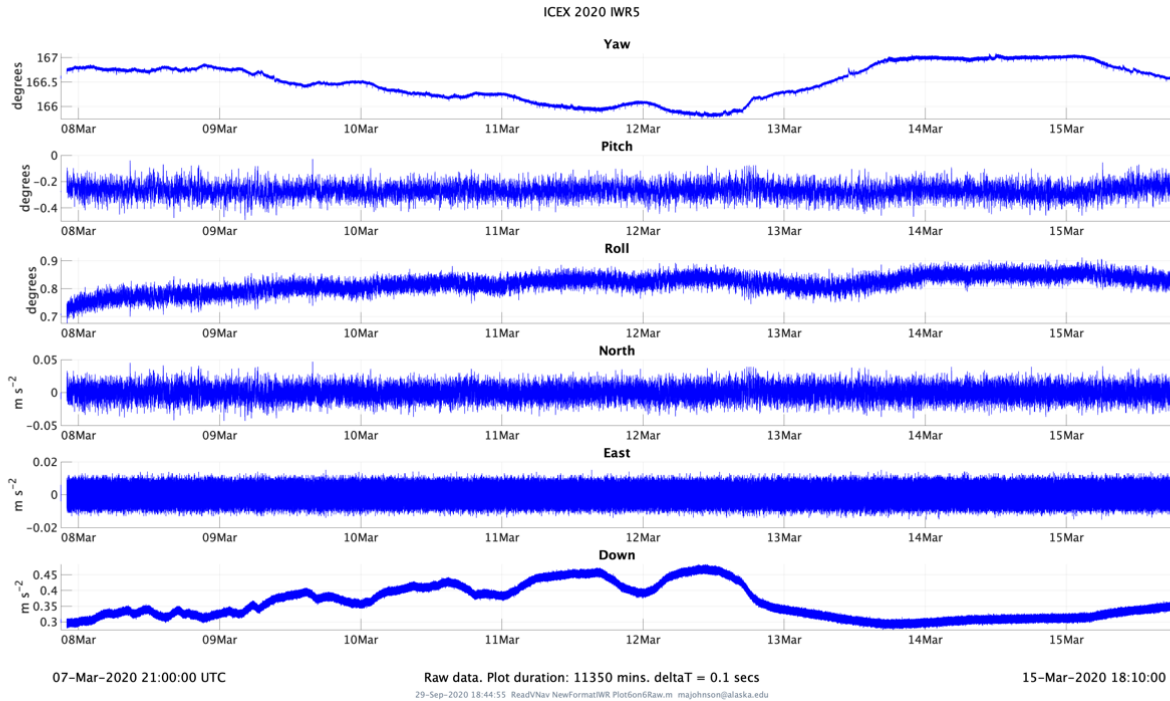
Figure AI.14. ICEX2020 March, IWR5. From top to bottom: Yaw, pitch, and roll (degrees), and accelerations with positive North, East, and Down (m s^{-2}).
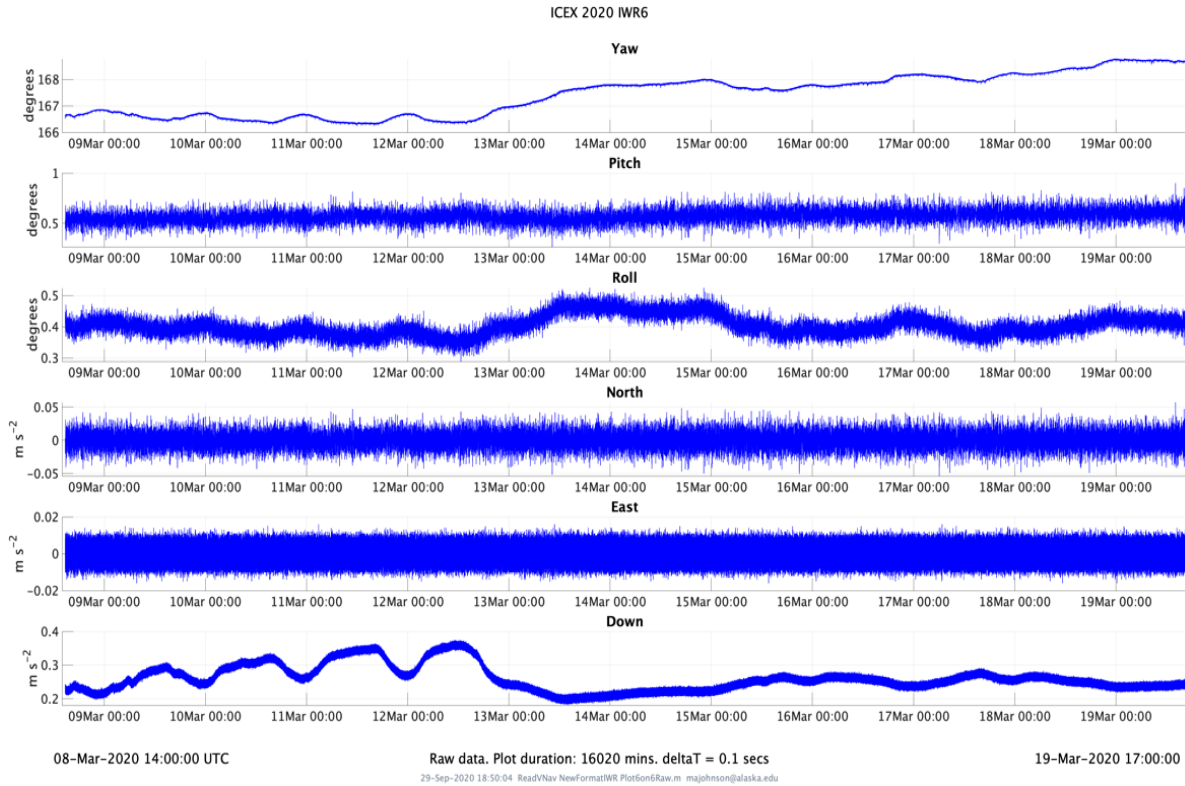
Figure AI.15. ICEX2020 March, IWR6. From top to bottom: Yaw, pitch, and roll (degrees), and accelerations with positive North, East, and Down (m s^{-2}).
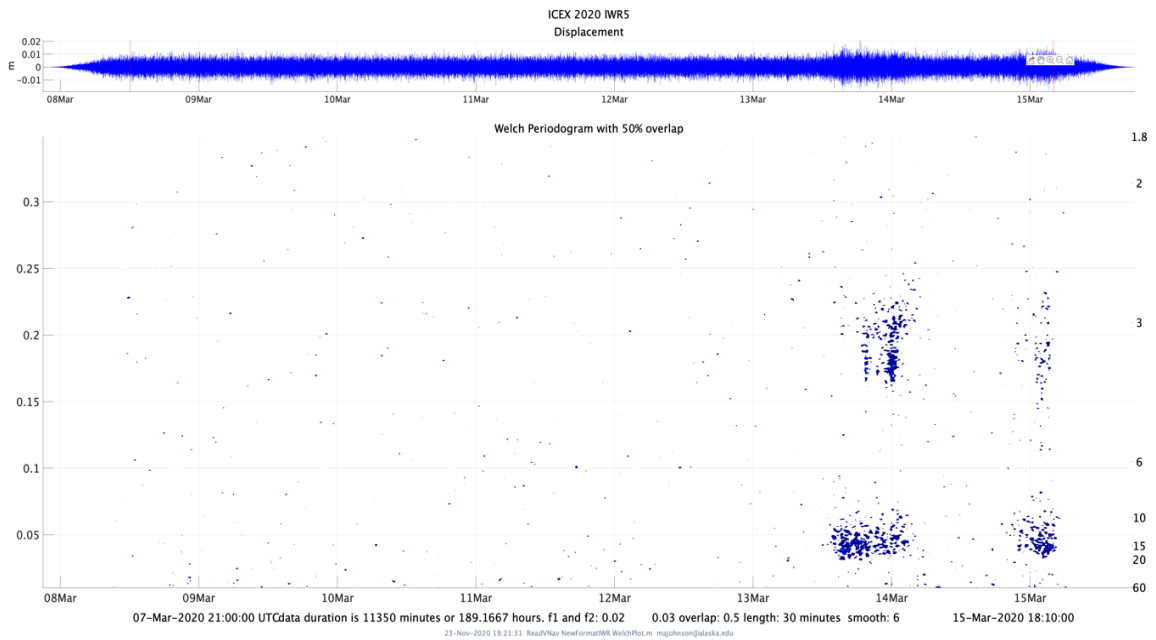
Figure AI.16. ICEX2020 March, IWR5, displacement and Welch Plot. Full deployment record displacement in meters (upper panel). Welch periodogram of displacement over the full deployment record (lower panel) with normalized frequency (left axis) and period in seconds (right axis).
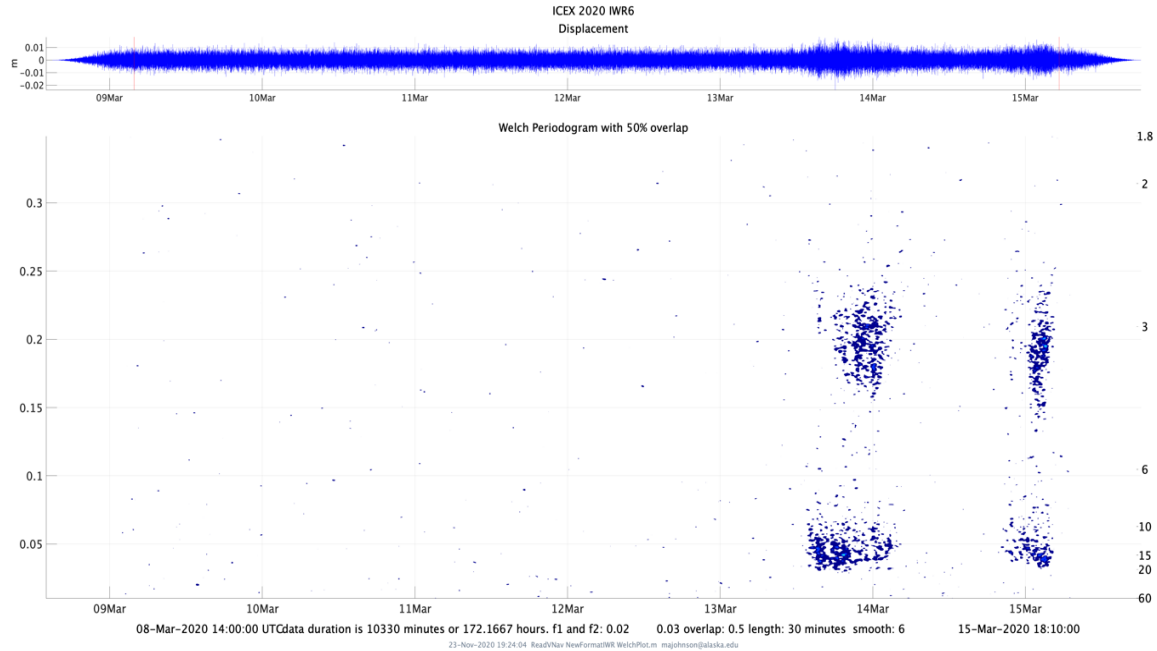
Figure AI.17. ICEX2020 March, IWR6, displacement and Welch Plot Full deployment record of displacement in meters (upper panel). Welch periodogram of displacement over the full deployment record (lower panel) with normalized frequency (left axis) and period in seconds (right axis).
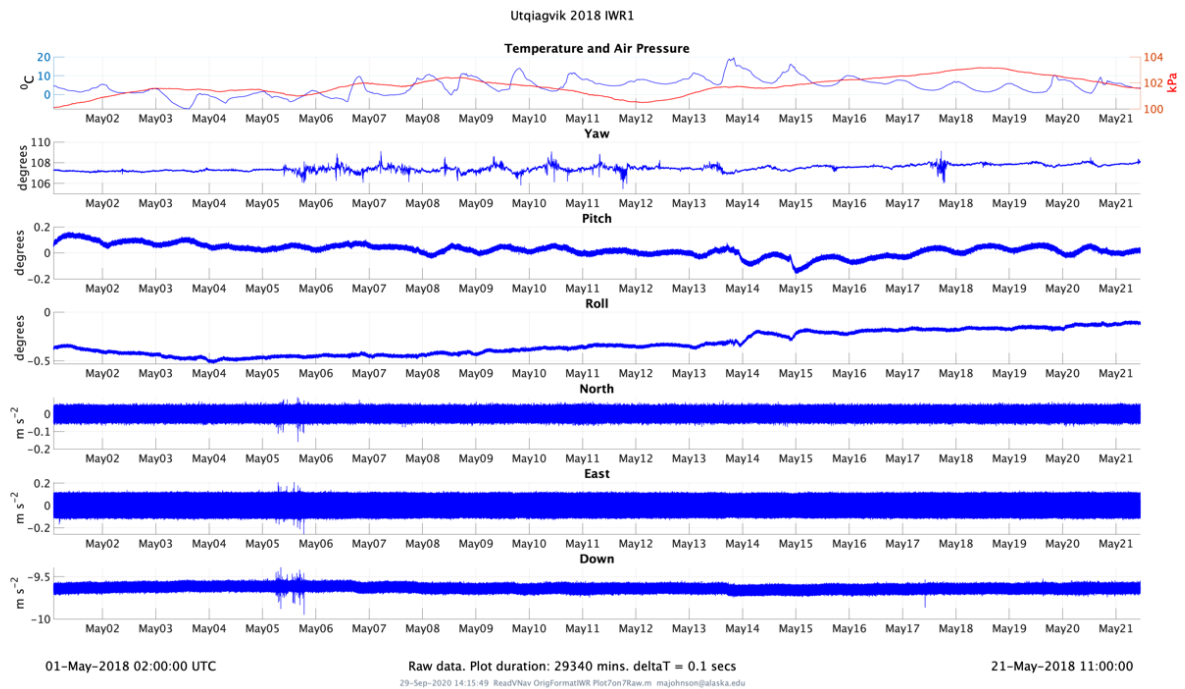
Figure AI.18. Utqiagvik May 2018, IWR1. From top to bottom: Air temperature ($°C$) and air pressure (kPa), yaw, pitch, and roll (degrees), and accelerations with positive North, East, and Down (m s^{-2}).
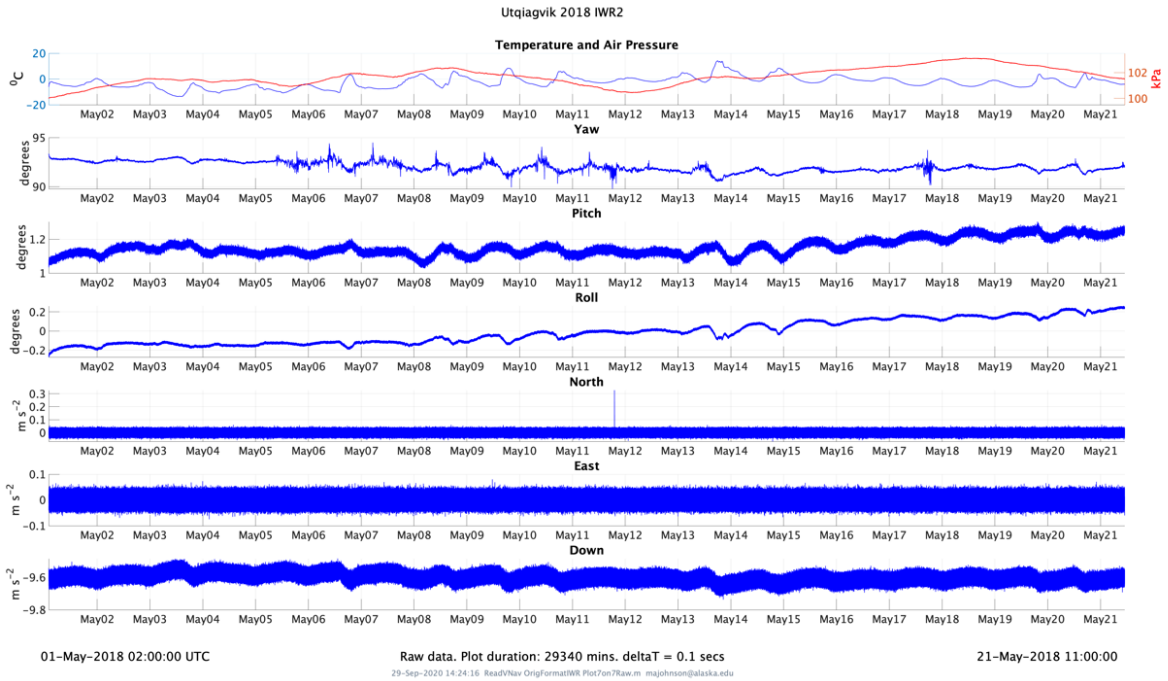
Figure AI.19. Utqiagvik May 2018, IWR2. From top to bottom: Air temperature ($°C$) and air pressure (kPa), yaw, pitch, and roll (degrees), and accelerations with positive North, East, and Down (m s^{-2}).
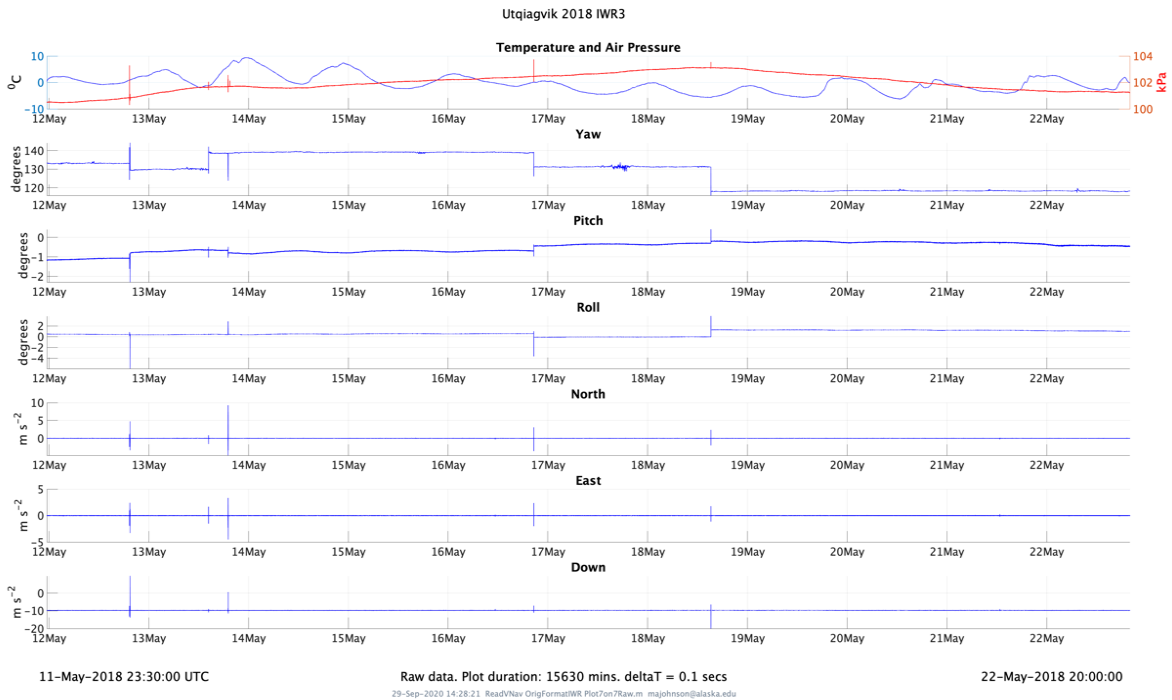
Figure AI.20. Utqiagvik May 2018, IWR3. From top to bottom: Air temperature ($°C$) and air pressure (kPa), yaw, pitch, and roll (degrees), and accelerations with positive North, East, and Down (m s^{-2}).
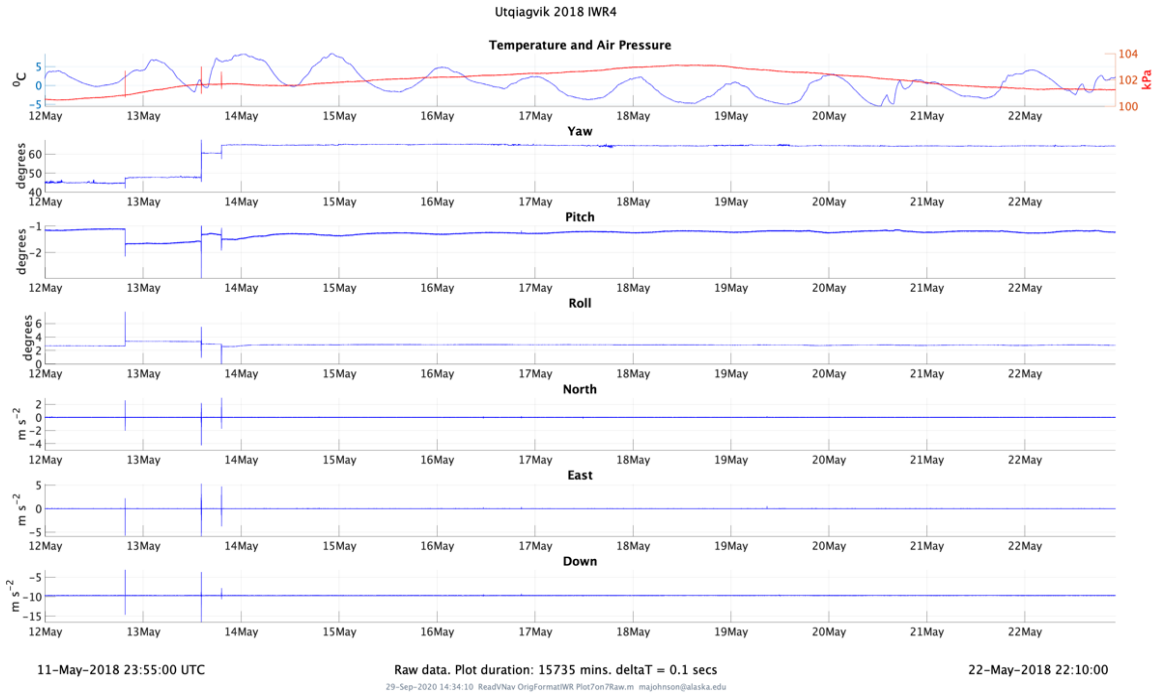
Figure AI.21. Utqiagvik May 2018, IWR4. From top to bottom: Air temperature ($°C$) and air pressure (kPa), yaw, pitch, and roll (degrees), and accelerations with positive North, East, and Down (m s^{-2}).
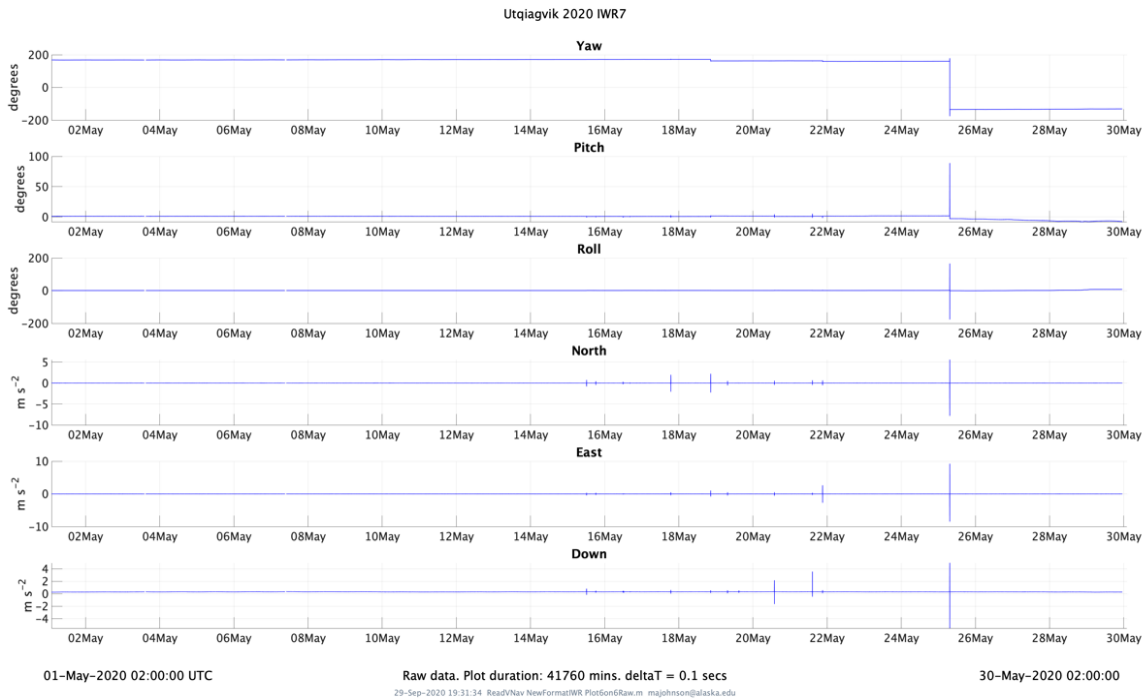
Figure AI.22. Utqiagvik May 2020, IWR7. From top to bottom: Yaw, pitch, and roll (degrees), and accelerations with positive North, East, and Down (m s^{-2}).

60
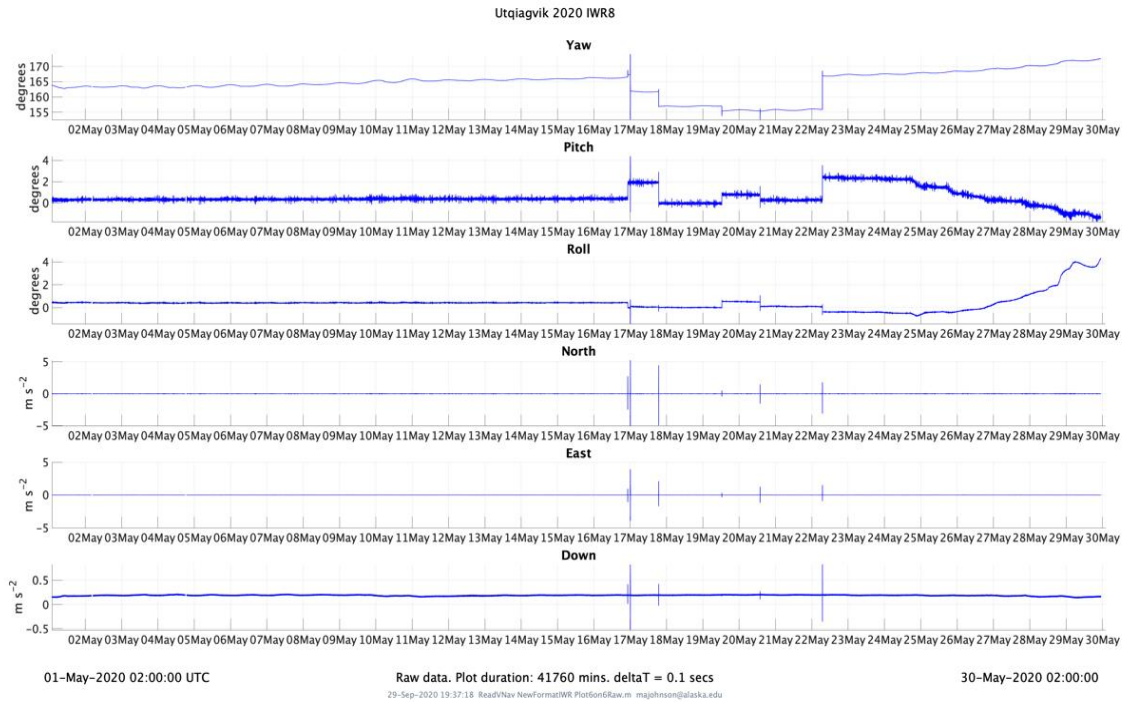
Figure AI.23. Utqiagvik May 2020, IWR8. From top to bottom: Yaw, pitch, and roll (degrees), and accelerations with positive North, East, and Down (m s^{-2}).
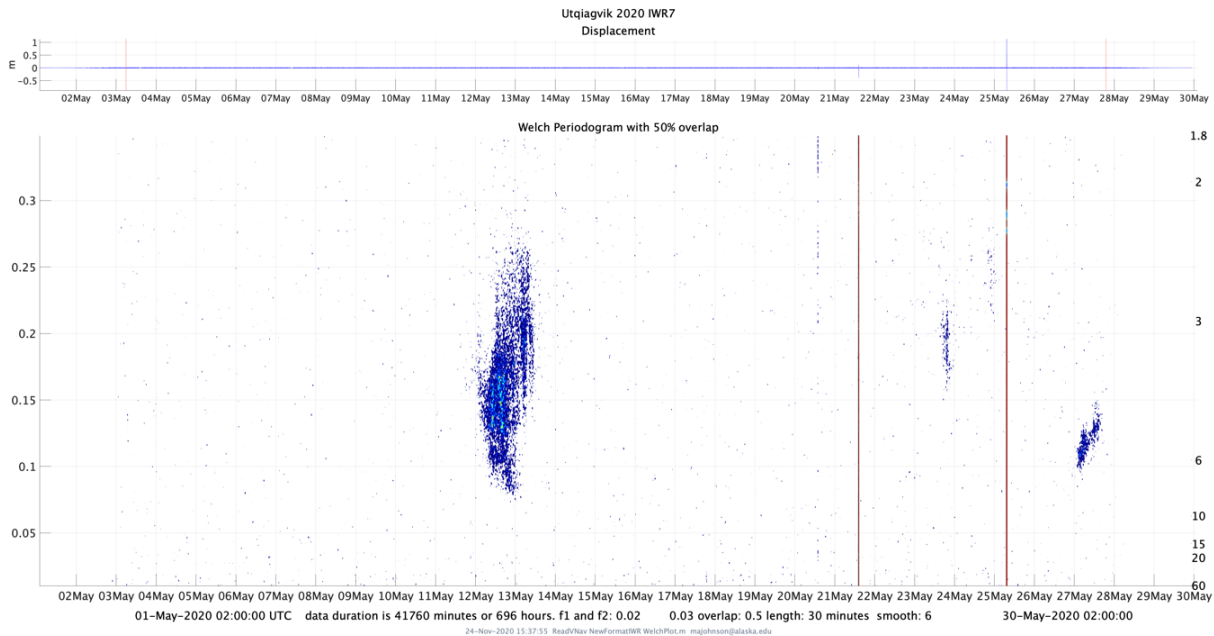
Figure AI.24. Utqiagvik May 2020, displacement and Welch Plot IWR7. Full record of displacement in meters (upper panel). Welch periodogram of displacement over the full deployment record (lower panel) with normalized frequency (left axis) and period in seconds (right axis).
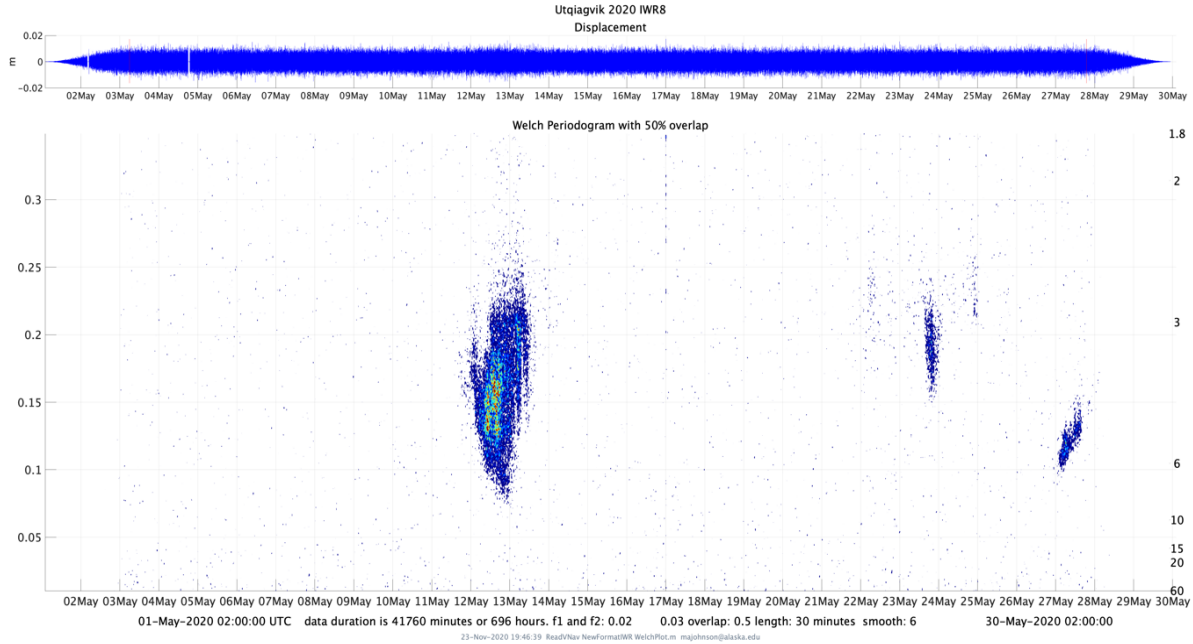
Figure AI.25. Utqiagvik May 2020, displacement and Welch Plot IWR8. Full record of displacement in meters (upper panel). Welch periodogram of displacement over the full deployment record (lower panel) with normalized frequency (left axis) and period in seconds (right axis).
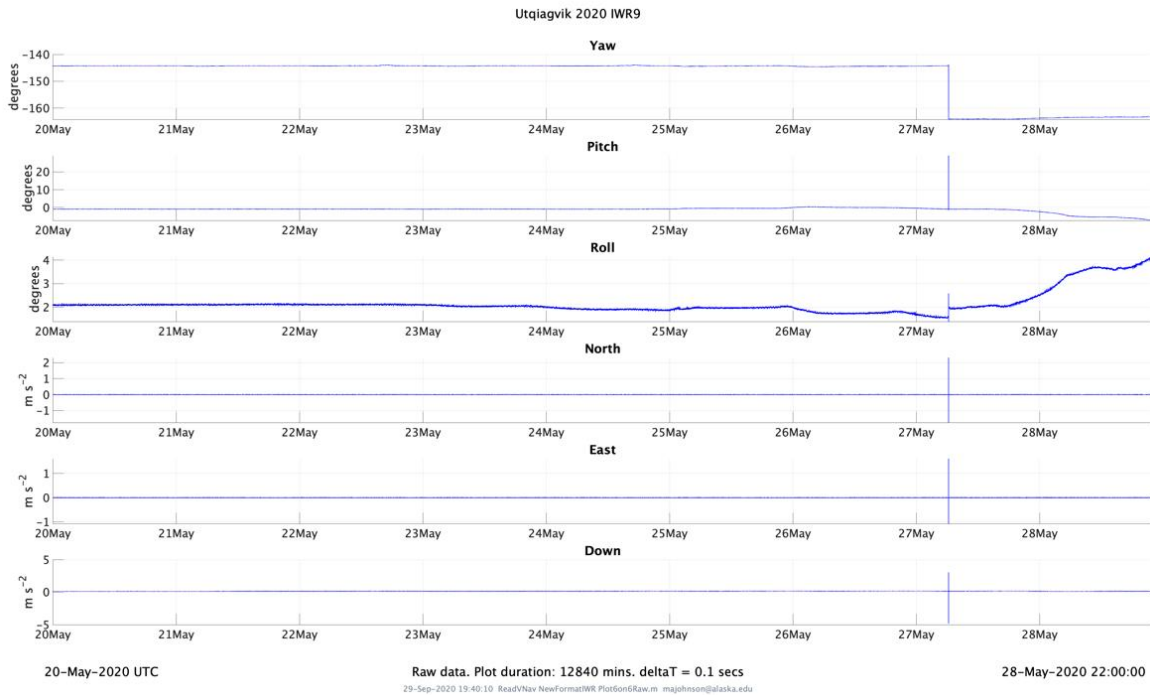
Figure AI.26. Utqiagvik May 2020, IWR9. From top to bottom: Yaw, pitch, and roll (degrees), and accelerations with positive North, East, and Down (m s^{-2}).
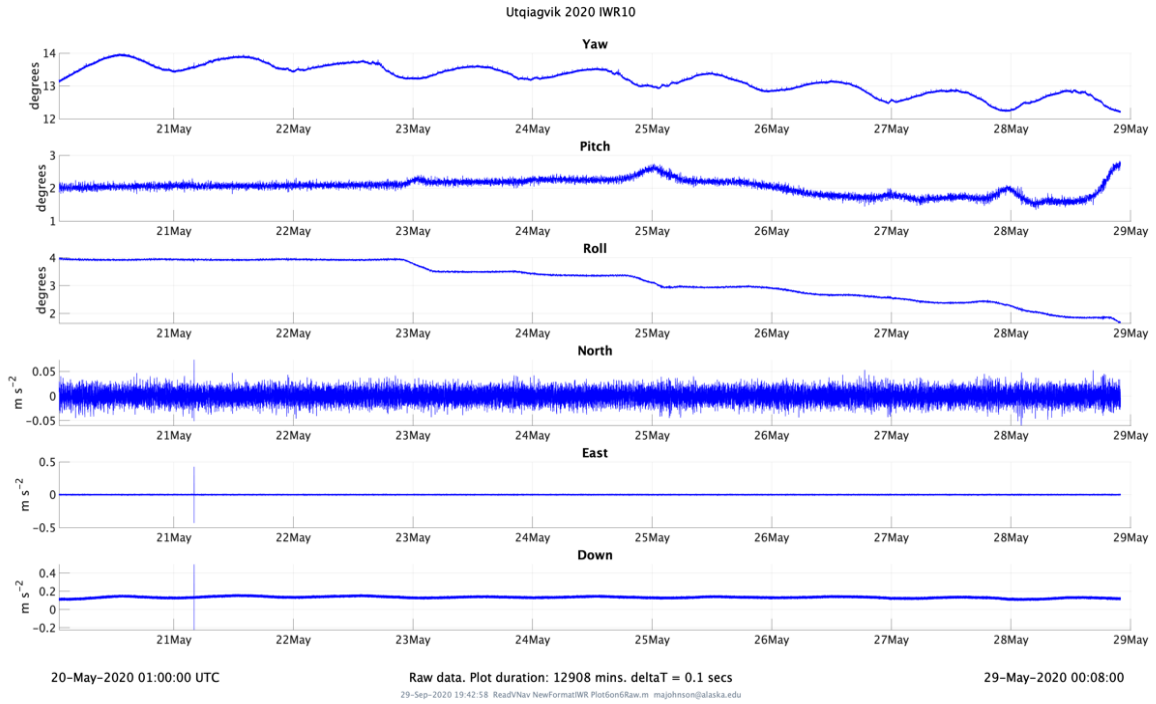
Figure AI.27. Utqiagvik May 2020, IWR10. From top to bottom: Yaw, pitch, and roll (degrees), and accelerations with positive North, East, and Down (m s^{-2}).
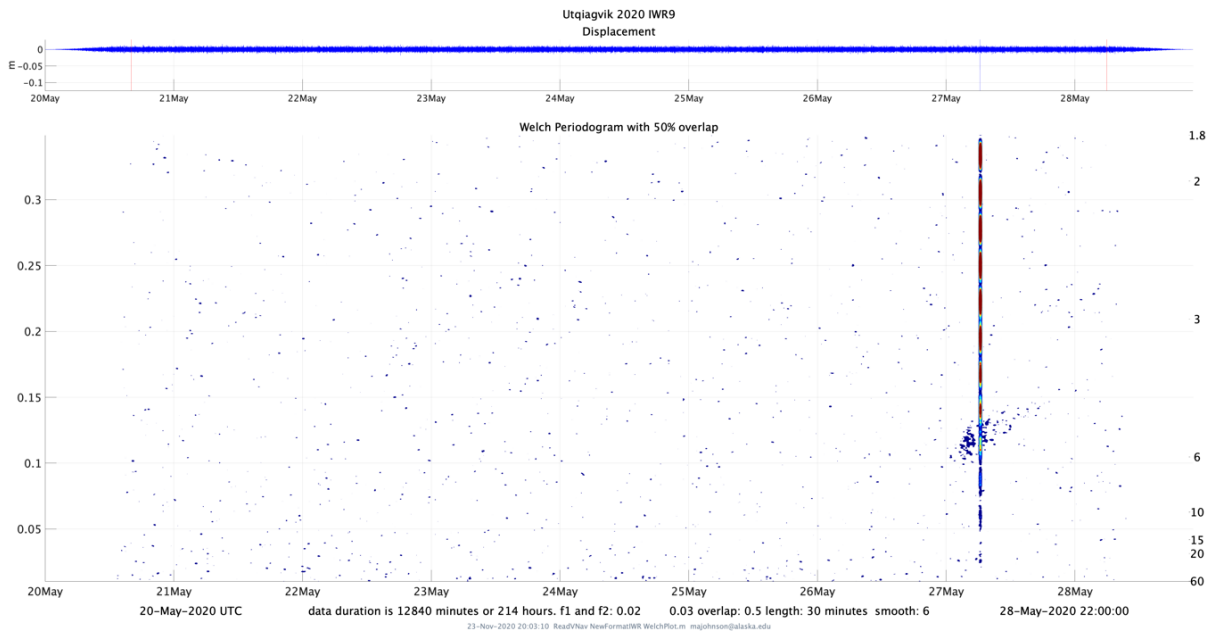
Figure AI.28. Utqiagvik May 2020, displacement and Welch Plot IWR9. Full record of displacement in meters (upper panel). Welch periodogram of displacement over the full deployment record (lower panel) with normalized frequency (left axis) and period in seconds (right axis).
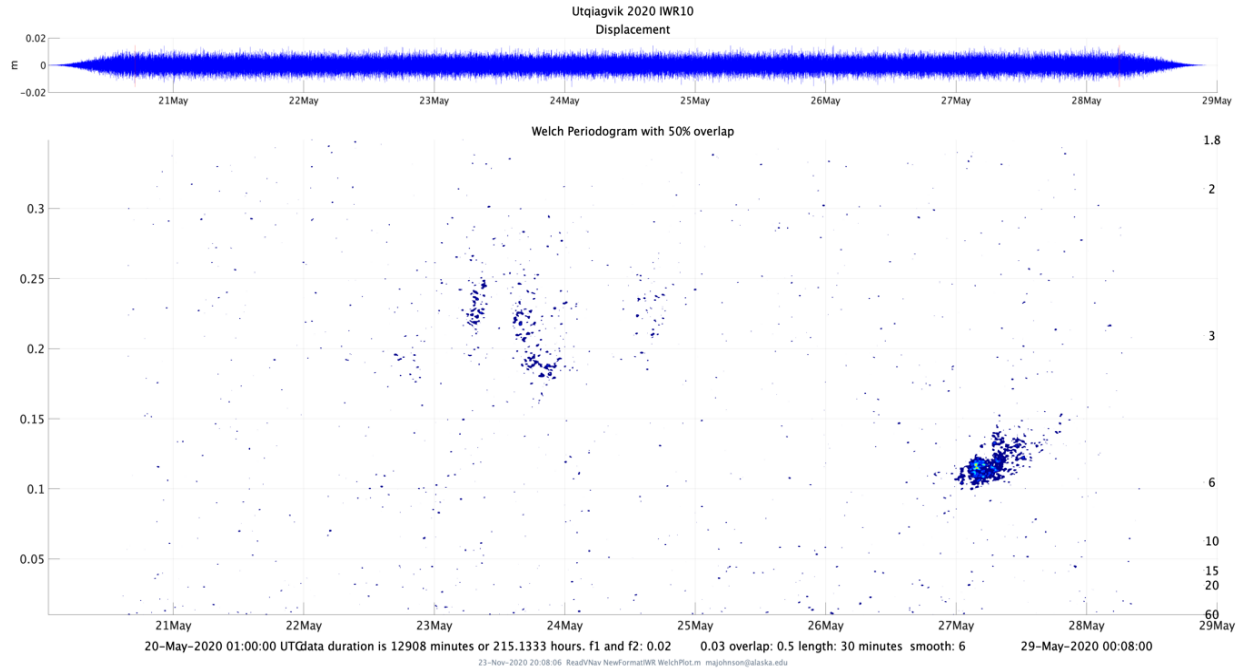
Figure AI.29. Utqiagvik May 2020, displacement and Welch Plot IWR10. Full record of displacement in meters (upper panel). Welch periodogram of displacement over the full deployment record (lower panel) with normalized frequency (left axis) and period in seconds (right axis).
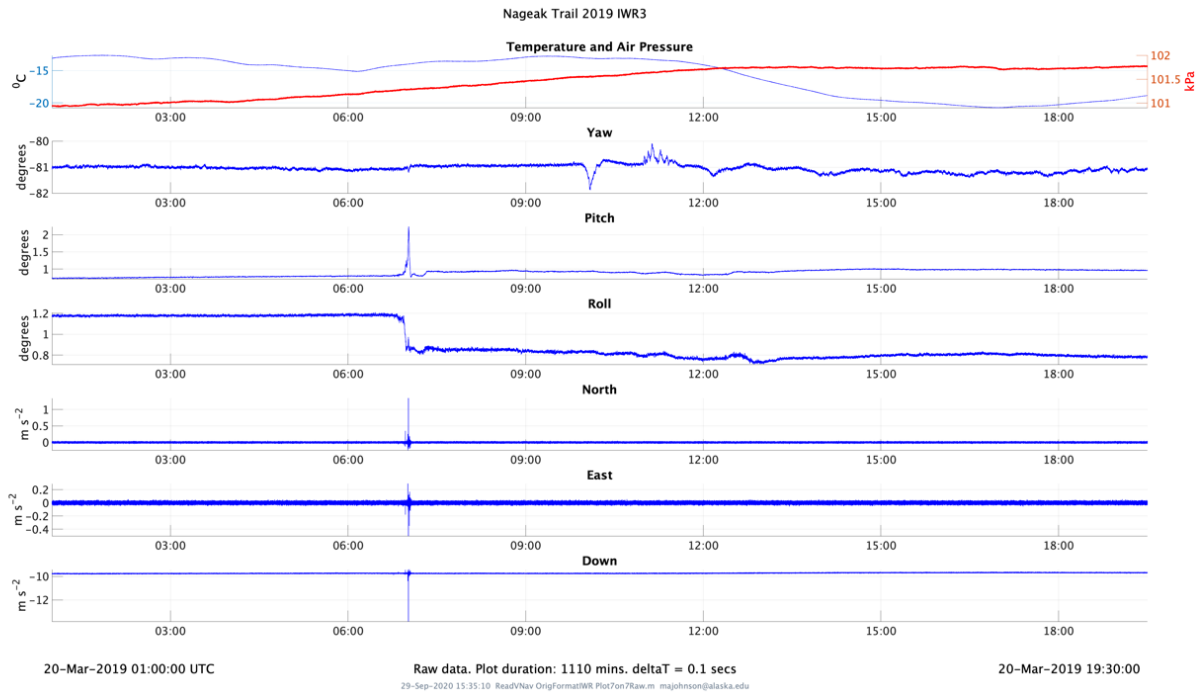
Figure AI.30. Nageak Trail March 2019, IWR3. From top to bottom: Air temperature ($°C$) and air pressure (kPa), yaw, pitch, and roll (degrees), and accelerations with positive North, East, and Down (m s^{-2}).
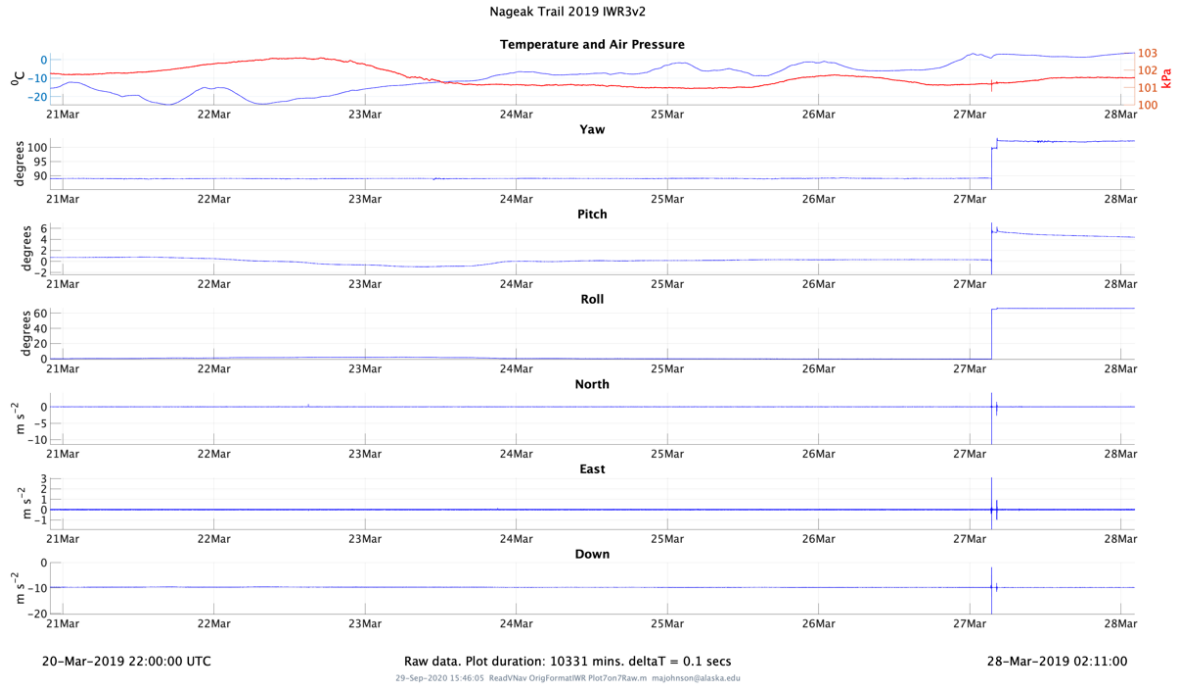
Figure AI.31. Nageak Trail March 2019, IWR3V2. From top to bottom: Air temperature ($°C$) and air pressure (kPa), yaw, pitch, and roll (degrees), and accelerations with positive North, East, and Down (m s^{-2}).
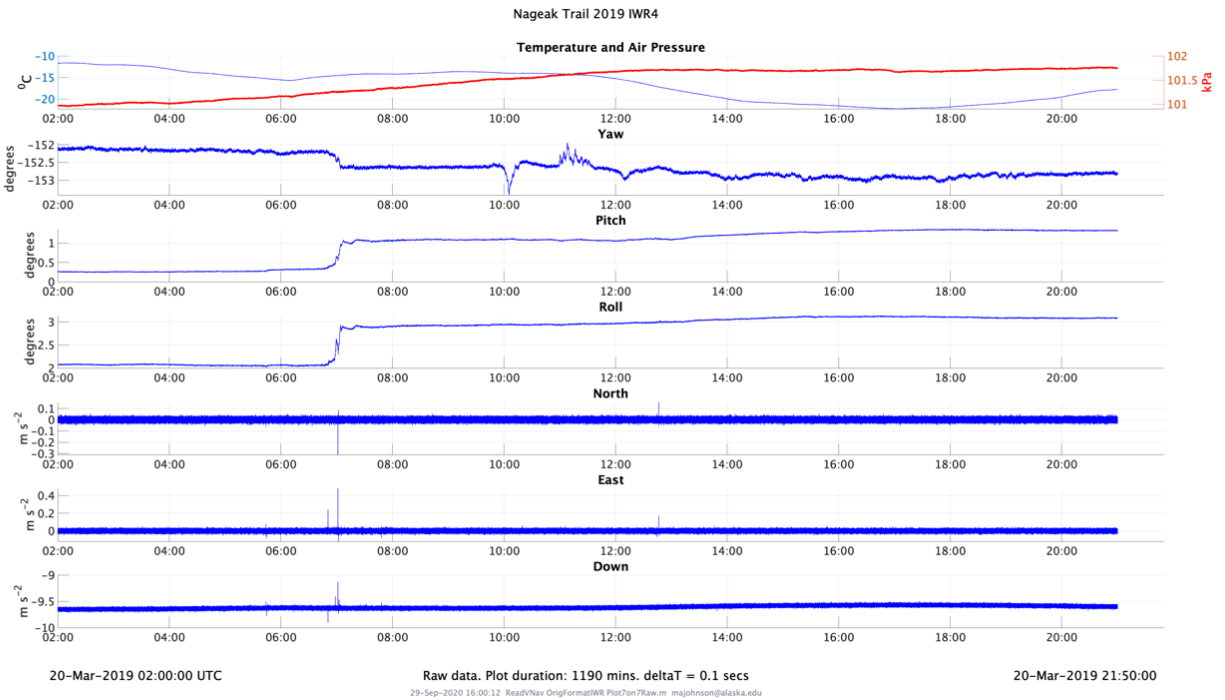
Figure AI.32. Nageak Trail March 2019, IWR4. From top to bottom: Air temperature ($°C$) and air pressure (kPa), yaw, pitch, and roll (degrees), and accelerations with positive North, East, and Down (m s^{-2}).
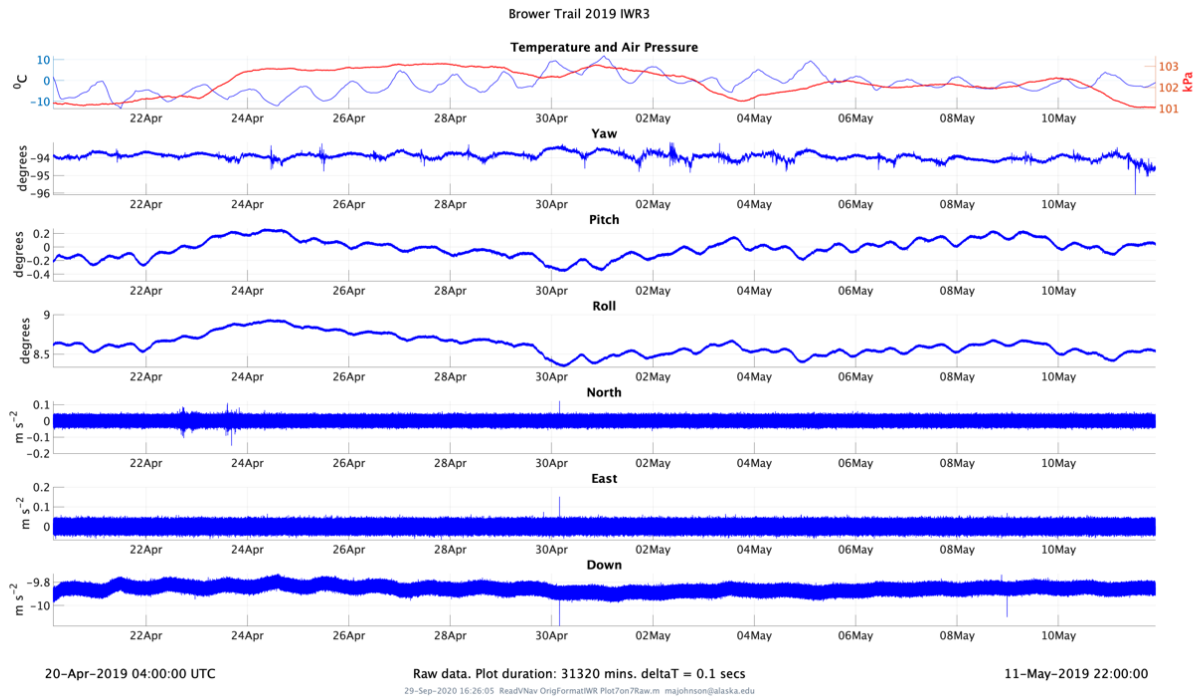
Figure AI.33. Brower Trail April – May 2019, IWR3. From top to bottom: Air temperature ($^{\circ}C$) and air pressure (kPa), yaw, pitch, and roll (degrees), and accelerations with positive North, East, and Down (m s^{-2}).

APPENDIX II

List of Figures

Figure AII.1. Able Seismic Vault December 2017 – January 2018. Accelerations with positive North, East, and Up (m s^{-2}) from the SVS-603.
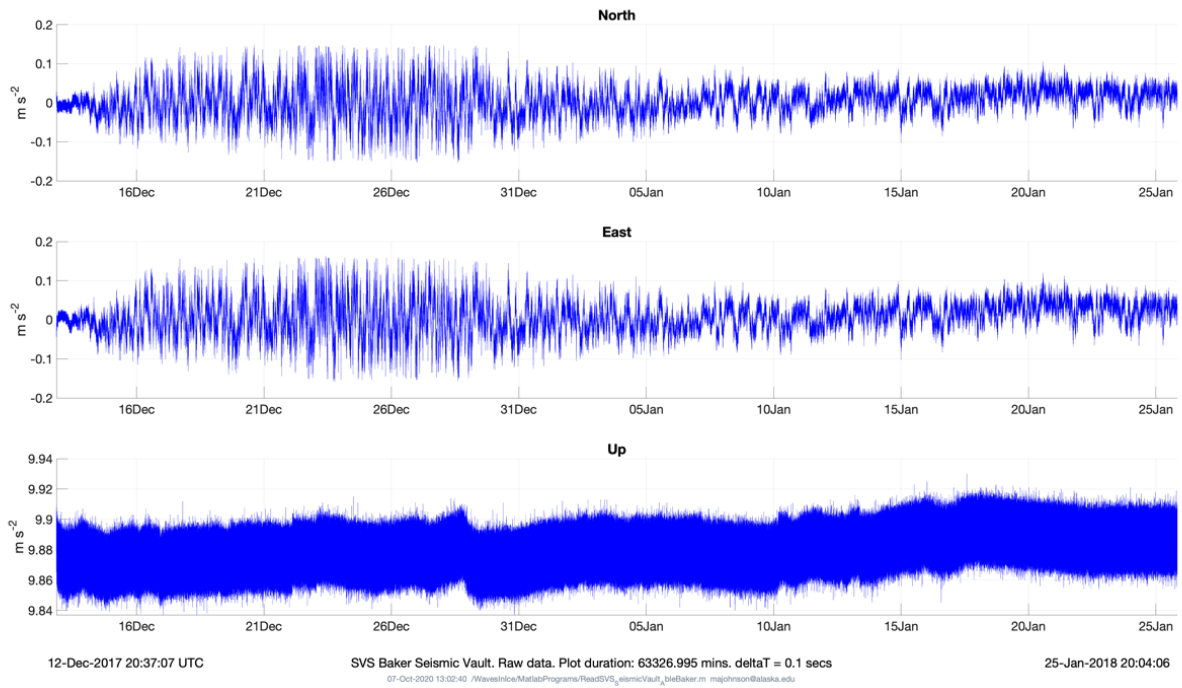
Figure AII.2. Baker Seismic Vault December 2017 – January 2018. Accelerations with positive North, East, and Up (m s^{-2}) from the SVS-603.
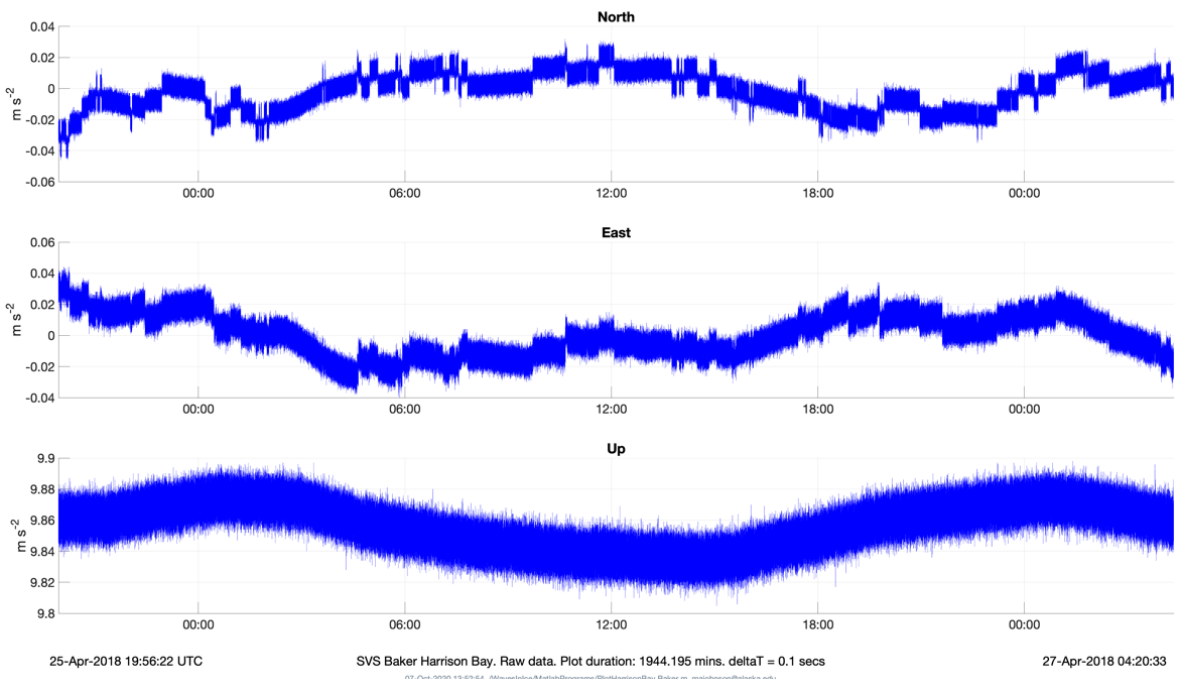
Figure AII.3. Baker Prudhoe Bay April 2018. Accelerations with positive North, East, and Up (m s^{-2}) from the SVS-603.
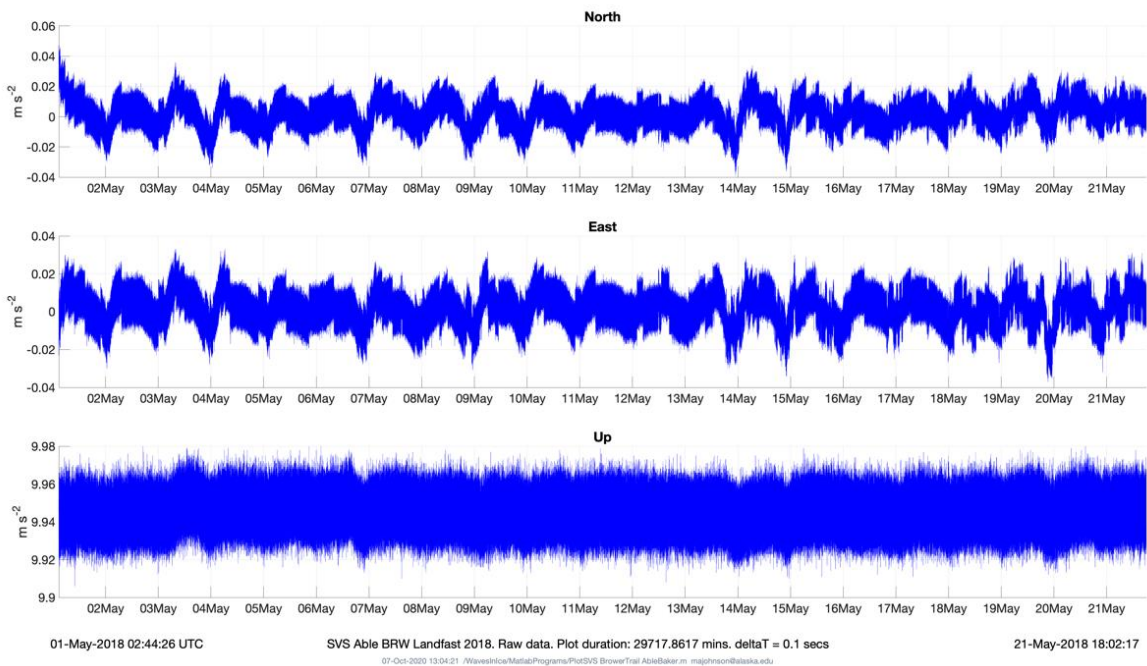
Figure AII.4. Able deployed on Utqiagvik landfast ice May 2018. Accelerations with positive North, East, and Up (m s^{-2}) from the SVS-603.
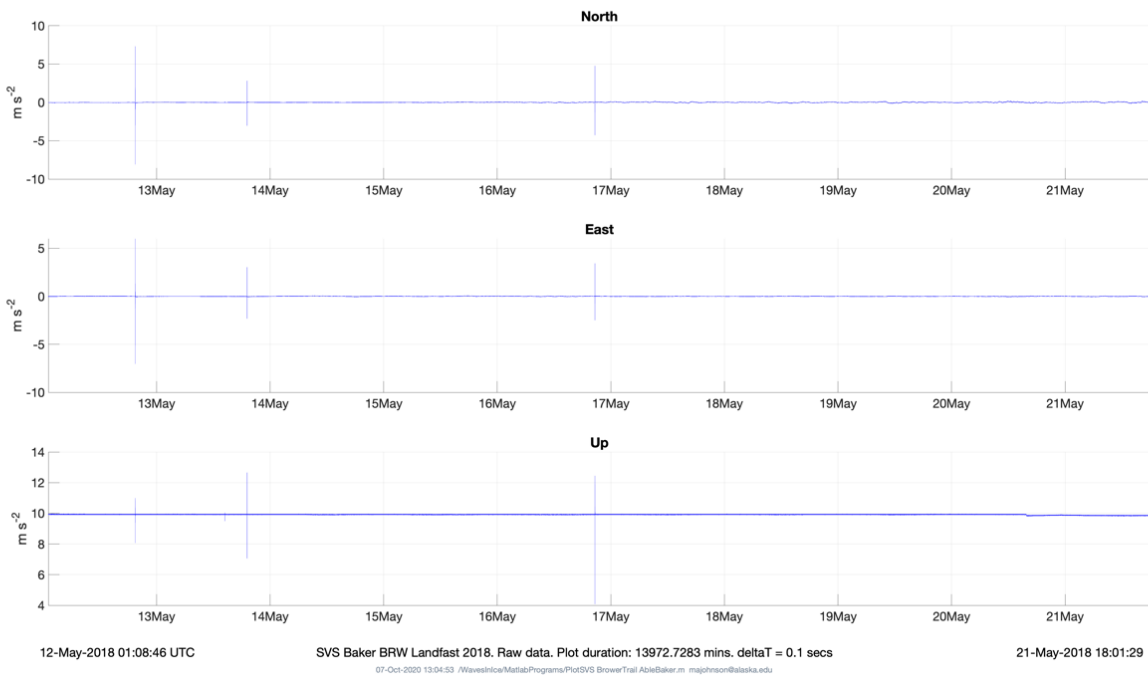
Figure AII.5. Baker deployed on Utqiagvik landfast ice May 2018. Accelerations with positive North, East, and Up (m s^{-2}) from the SVS-603. Large horizontal and vertical accelerations to ~7 m s^{-2} are visible. These large signals are similarly timed to the large accelerations from IWR4 deployed nearby.
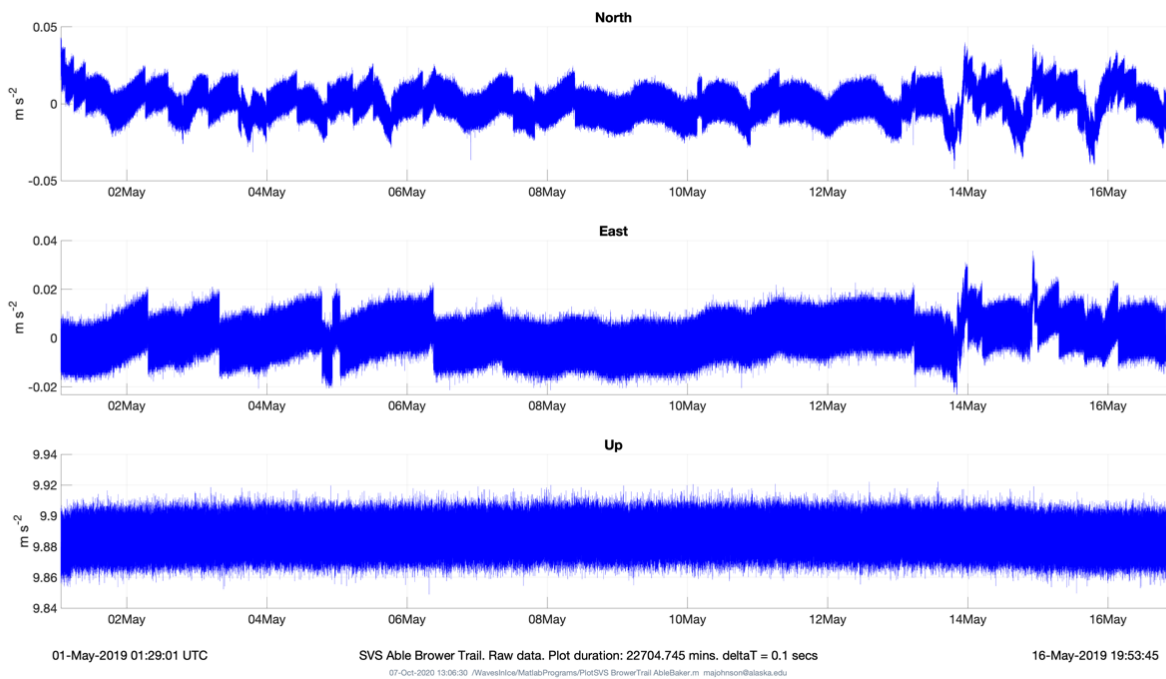
Figure AII.6. Able Frederick Brower Trail May 2019. Accelerations with positive North, East, and Up (m s^{-2}) from the SVS-603.
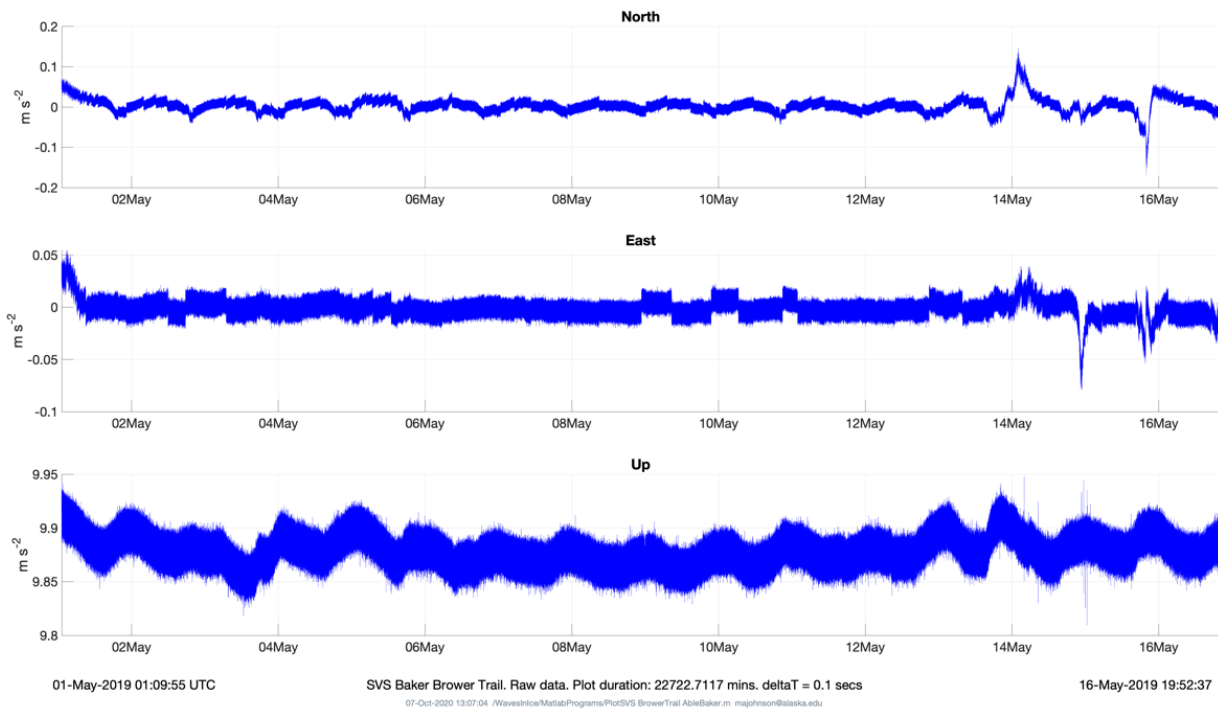
Figure AII.7. Baker Frederick Brower Trail May 2019. Accelerations with positive North, East, and Up (m s^{-2}) from the SVS-603.

The Department of the Interior Mission

As the Nation's principal conservation agency, the Department of the Interior has responsibility for most of our nationally owned public lands and natural resources. This includes fostering the sound use of our land and water resources, protecting our fish, wildlife and biological diversity; preserving the environmental and cultural values of our national parks and historical places; and providing for the enjoyment of life through outdoor recreation. The Department assesses our energy and mineral resources and works to ensure that their development is in the best interests of all our people by encouraging stewardship and citizen participation in their care. The Department also has a major responsibility for American Indian reservation communities and for people who live in island communities.

The Bureau of Ocean Energy Management

The Bureau of Ocean Energy Management (BOEM) works to manage the exploration and development of the nation's offshore resources in a way that appropriately balances economic development, energy independence, and environmental protection through oil and gas leases, renewable energy development and environmental reviews and studies.